CZECH TECHNICAL UNIVERSITY IN PRAGUE

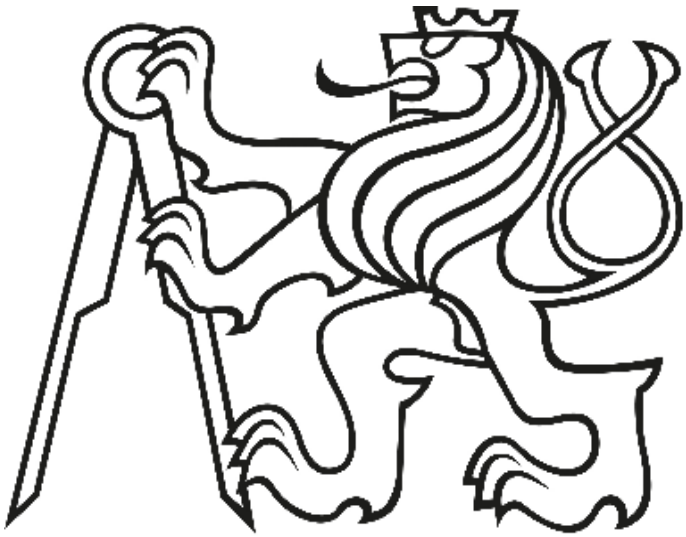

DOCTORAL THESIS

Mgr. Barbara Nevrlá
Institute of Plasma Physics of CAS

GEOMATERIALS IN PLASMA SPRAYING

Supervisor: prof. RNDr. Petr Špatenka, CSc.
Supervisor-Specialist: doc. Ing. Pavel Ctibor, Ph.D.

CTU in Prague, Faculty of Mechanical Engineering, Department of Materials Engineering

April 2021

Acknowledgements

Firstly, I would like to thank prof. Ing. Dr. Pavel Chráska, DrSc. who was at my beginnings at the Institute of Plasma Physics and was the initiator of this thesis.

Genuine thanks belong to my supervisor-specialist doc. Ing. Pavel Ctibor, Ph.D., without his generous support would this work hardly arose.

Many thanks also go to the prof. RNDr. Petr Špatenka, CSc. and all the staff from the Institute of Plasma Physics for their tuition, analyses, and other support. As for my colleagues, I would like to thank Ing. Karel Neufuss, who with his lifelong practical experience with WSP and WSPH torches greatly contributed to the rapid finding of suitable spraying conditions. Many thanks include Monika, Mr. Dlabáček, and Mr. Kutílek, Marek, Fero, Vlasta and all of my colleagues. I would like to thank Veronika Koudelková and my helpful geologists for sharing all non-technical ideas.

Humble and great thanks belong to all the co-authors of the articles that form background of this work.

I would like to thank my wonderful husband for the encouragement and patience over many years of my Ph.D. study. Big thanks definitely go to all the babysitters of our little daughter. Finally, I thank Žofie, who stood long hours to watch Krteček and let me finish the thesis.

Declaration

I hereby declare that this thesis is the result of my own work and all the sources I used are in the list of references.

In Prague ……. ……

Barbara Nevrlá

Annotation

The thesis focuses on the selection and investigation of natural materials that will be proper as an alternative to the expensive synthetic powders used for plasma spraying of protective layers. The thesis is focused on the examination of ceramic coatings from geomaterials in plasma spraying applications especially at increased temperatures.

Anotace

Disertační práce si klade za cíl hledat alternativní materiály, které by nahradily drahé syntetické prášky používané k přípravě ochranných vrstev deponovaných pomocí plazmového stříkání. Pozornost je soustředěna na keramické vrstvy z geomateriálů. Práce je zaměřena na testování vhodnosti vybraných materiálů pro použití v technologii plazmového stříkání zejména ve zvýšených teplotách.

Contents

1 Aim of Thesis and Introduction 10

2 Overview of the Studied Topic 11

2.1 Plasma Spraying 11

2.2 Common Materials in the Plasma Spraying Technology 13

2.3 Alternative Materials in the Plasma Spraying Technology 14

2.3.1 Zircon 15

2.3.2 Mullite 16

2.3.3 Diopside 18

2.3.4 Tourmaline 18

2.3.5 Alternative Materials in Thesis 18

3 Objectives of the Thesis 20

4 Experimental Part 21

4.1 Powder Pre-Treatment, Plasma Spraying and Coating Post-Treatment 22

4.1.1 Zircon 22

4.1.2 Diopside 22

4.1.3 Tourmaline 23

4.1.4 Kaolin 23

4.1.5 Clay Shale 24

4.2 Analytical Methods 25

5 Results and Discussion 28

5.1 Zircon 28

5.2 Diopside 32

5.3 Tourmaline 40

5.4 Kaolin 47

5.5 Clay Shale 56

6 Implication for Science and Practical Applications 67

7 Conclusion 69

8 Literature 71

A List of Publications Related to the Thesis 80

List of Symbols and Abbreviations

a	Lattice Constant
A	Ampere (Unit of Electric Current)
Å	Ångström (Unit of Length)
APS	Atmospheric Plasma Spray
ASTM	American Society for Testing and Materials
A111VHR	Sample Label
a.u.	Arbitrary Units
BSE	Back Scattered Electron
c	Lattice Constant
CIR	Mean Circularity
CIR-min	Minimal Detected Circularity
cm^2	Square Centimeter (Unit of Area Measurement)
CCD	Charged Coupled Device
CMAS	Calcium-Magnesium-Alumina-Silicate
cps/eV	Counts per Second per Electron-Volt
CRVC	Crystallization Related Volume Changes
CTE	Thermal Expansion Coefficient, in 10^{-6}/K
Cu-Kα	Copper K-alpha radiation
D	Crystallite Size (Diameter), in nm
DSC	Differential Scanning Calorimetry, Heat Flow Data in mW
DTA	Differential Thermal Analysis, Results in mV, µV/g or µV
EBC	Environmental Barrier Coatings
ED	Equivalent Diameter (Pore Size), in µm
EDX	Energy Dispersive X-Ray Analysis
θ	Diffraction Angle
FD	Feeding Distance
FFP	Free-Flight Particles
FGM	Functionally Graded Materials
FSP	Free-Standing Plates
FSZ	Yttria-Stabilised-Zirconia
g	Gram (Unit of Mass)
g/cm^3	Gram per Cubic Centimeter (Unit of Specific Weight)
h	Hour (Unit of Time)
HTXRD	High Temperature X-Ray Diffraction
HVm	Vicker's Microhardness, in GPa
HVOF	High Velocity Oxygen Fuel Spraying
IA	Image Analysis
IWR	Inverse Wear Rate (Wear Resistance), in m/mm^3
K	Kelvin (Unit of Temperature)
K/min	Kelvin per Minute (Unit of Heating Rate)
kJ/mol	Kilojoule per Mole (Unit of Activation Energy)
keV	Kiloelectron-Volt (Unit of Energy)
KP	Sample Label
kV	Kilovolt (Unit of Electric Potential)
kW	Kilowatt (Unit of Power)
l/h, l/min	Liter per Minute, Liter per Hour (Units of Flow Rate)
LTCC	Low Temperature Co-Fired Ceramic
min	Minute (Unit of Time)

MK	Sample Label
mm	Millimeter (Unit of Length)
mg	Milligram (Unit of Mass)
MPa	Megapascal (Unit of Pressure and Stress)
m/s	Meter per Second (Unit of Speed)
m-ZrO_2	Monoclinic Zirconia
µm	Micrometer, Micron (Unit of Length)
N	Newton (Unit of Force)
N/A	Not Applicable
NIR	Near Infrared
nm	Nanometer (Unit of Length and Wavelength)
PS	Plasma Spray, Plasma Sprayed
PSZ	Partially-Stabilized Zirconia
ψ	Psi
R_a	Surface Roughness, in µm
RT	Room Temperature
R_{wp}	Weighted Profile R-Factor
s	Second (Unit of Time)
SAR	Slurry Abrasion Response
SAS	Spinel Type Aluminosilicate
SD	Spray Distance
SE	Secondary Electron
SEM	Scanning Electron Microscope/Microscopy
T_a	Annealing Temperature, in °C
TEBC	Thermal and Environmental Barrier Coatings
TBC	Thermal Barrier Coatings
TC	Thermal Conductivity, in W/mK
TD	Thermal Diffusivity, in cm^2/s
TG	Thermal Gravimetry, in mg
t-ZrO_2	Tetragonal Zirconia
UV	Ultra Violet
Vis	Visible
vol.%	Volume Percentage
VPS	Vacuum Plasma Spray
WSP	Water Stabilized Plasma
WSP-H	Hybrid Water Stabilized Plasma
wt.%	Weight Percentage
XRD	X-Ray Diffraction
YSZ	Fully-Stabilised-Zirconia
α, β, γ, δ, ε	Mineral Phases
°	Degree
> , <	Greater Than, Less Than
~	Approximately Equal
×	Multiply
±	Plus or Minus

1 Aim of Thesis and Introduction

Today's materials in their day to day technical practice are required to meet high designer demands to withstand the harsh conditions. An example is the jet engine of an aircraft. The temperatures of the gases rotating the turbine blades can exceed 1650 °C [1], which is a temperature incompatible with the use of metal alloys due to their melting point and in terms of their mechanical properties. Similar problems occur also in a number of other applications such as automotive, chemical or energy industry, etc.

As traditional homogeneous single materials are no longer sufficient for the increasingly demanding conditions of the operating environment (high temperatures and pressures, temperature gradients, high mechanical stresses, oxidation or corrosive atmospheres, erosion, etc.), efforts to find more durable materials continues. Attention is focused on composite materials or on strengthening only the surface of the component. This is possible by means of surface hardening, nitriding, cementation, or application of more resistant surface layers (galvanizing, plating, physical and chemical vapor deposition, etc.). The last group of modifications includes plasma spraying technology utilizing the principle of thermal spray, as will be described below. Typically, thermal and environmental barrier coatings (TEBCs) are produced by plasma spraying. TEBCs protect the substrate against harsh environments and extend component lifetimes. Here, ceramic coating layers perform as barriers to heat transfer.

Since high-quality synthetic powders utilized for spraying these ceramics are often very expensive, a cheaper alternative would be demanded. Institute of Plasma Physics of the Czech Academy of Sciences (IPP) focuses on the investigation of plasma sprayed layers including a search for less expensive alternatives to commercial materials. Its attention pays also to the so-called geomaterials. General definition of the term geomaterial by Fookes [2] encompasses primary and secondary raw materials like soils, rocks and minerals which are mainly used in the construction and structuring of buildings, both in their natural and processed form. In this work, the concept of geomaterials is limited to inorganic raw materials, as was introduced, for example, by Přikryl [3], i.e. mineral-based naturally occurring materials.

Natural raw materials contain undesirable impurities and thus cannot be utilized in high specific applications, as, for example, thermal insulation layers on the vanes and stators of plane turbine motors. Nevertheless, the coating of components of land-based turbines with layers made from natural materials would be, in specific cases, possible. However, a number of these materials can for example meet the condition of thermal stability at elevated operating temperatures. The issue of the utilization of raw materials in the plasma spraying field of investigation is explored insufficiently yet.

The thesis focuses on the selection and investigation of materials that would be a proper alternative to the expensive synthetic powders, conventionally used for plasma spraying of protective layers. The general demand for newly selected materials is besides of the advantageous properties also lower price and good availability. The ceramic layers made from geomaterials are subjects of the interest; thereby the thesis is focused on the testing and selection of novel materials suitable for plasma spraying. The presented work states the results of investigation of the thermal properties supplemented by a study of microstructure and composition of newly prepared plasma sprayed coatings. These results were published in 6 publications in impacted journals (see list of publications) and presented at international conferences.

2 Overview of the Studied Topic

2.1 Plasma Spraying

Plasma spraying is a technology from the thermal spraying processes and involves the coating of melted accelerated particles onto a substrate. A newly formed coating serves as an additional layer that improves the quality or protects the original surface. Plasma spraying is a time-saving and economic technology suitable for coating of large volumes of material, also including the design of thick-walled layers on topographically complicated surfaces.

The process of plasma spraying is based on the utilization of a plasma torch, being able to generate thermal plasma. Plasma is produced in the electric discharge which is stabilized by gas (Atmospheric Plasma Spray, APS) or by water vapor (Water Stabilized Plasma, WSP), while both media are ionized during the process. In the APS spraying technology, the excitation of plasma is based on the ignition of electric arc in the chamber continuously filled with suitable flowing gas (argon, nitrogen, or hydrogen). The Hybrid Water Stabilized Plasma (WSP-H) technology is based on the utilization of both systems – a mixture of gas and water vapor (figure 1). Liquid stabilization of plasma in the WSP is based on the rotation of water whirl around the electrical arc where thermal energy vaporizes water. As a result, the water vapor dissociates and ionizes. Contrary to APS technology, this combined design of plasma torch provides several advantages: (i) using high temperature and large volumes of material and (ii) prolongation of the service life of the apparatus. In the experiments described in this thesis, systems operating with WSP and WSP-H technology are used.

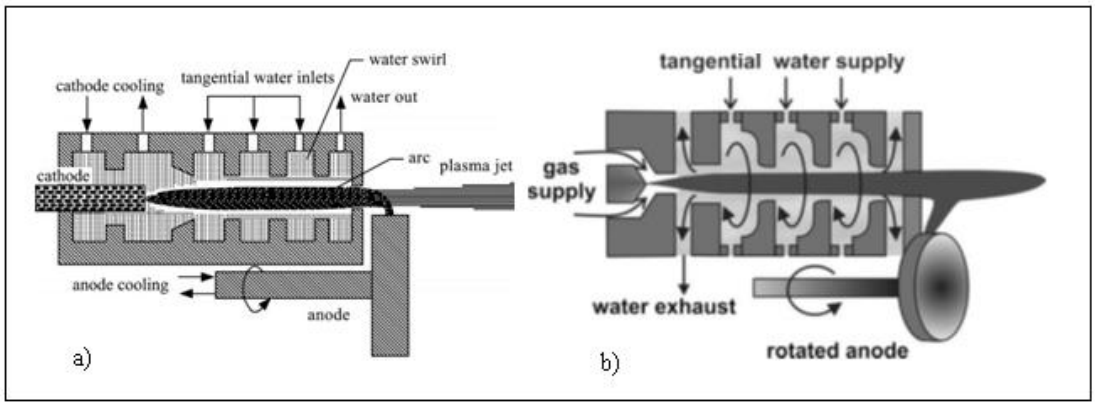

Figure 1. Scheme of water stabilized (a) and hybrid plasma torch (b) [4]

The splats subsequently create an anisotropic and inhomogeneous layer of the plasma coating (figure 2) with a relatively high-porosity structure. The structure of such a layer may also contain unmelted and oxidized particles (metals) or oxygen-depleted oxides with disrupted stoichiometry (e.g. titanium oxide based ceramic).

The composition of the original material strongly influences the final quality of the plasma coating. The main variables that represent the key parameters during the assessment of a suitable powder for plasma spraying (so-called feedstock) include chemical composition, microstructure, powder size distribution, homogeneity, and thermal conductivity which influence the level of melting of individual particles.

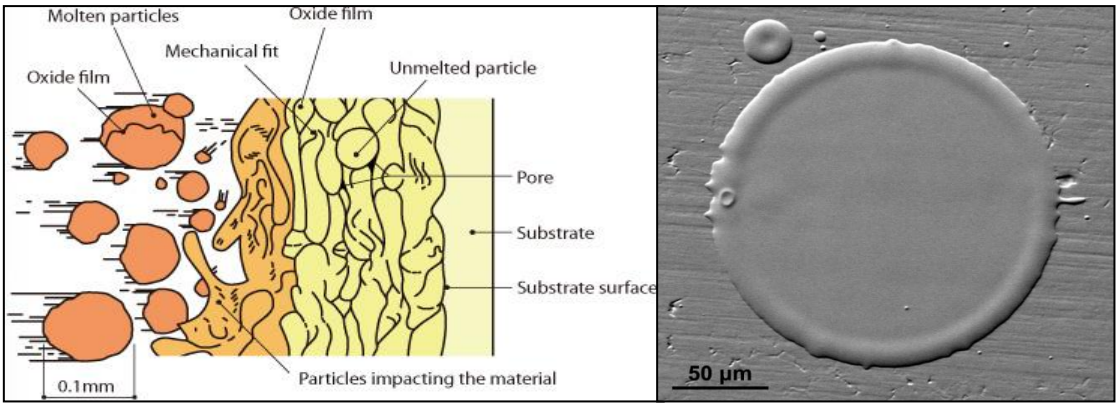

Figure 2. Scheme of the plasma coating [5] *and the detail of splat (an Eucor ceramic coated with the water stabilized torch, electron microscope)* [6]

In addition, the spraying parameters determine the quality of the resulting coating, namely, the geometric setting of powder feeding, the spray distance (SD; axial distance between the plasma nozzle and the substrate), the feeding distance (FD; axial distance between the plasma nozzle and the injector), the type of a feeding medium, the velocity of acceleration of the powder towards the substrate, the substrate preheating, and the material of the substrate or the chemical composition of the previously sprayed layer. The powder particles have to be fully smelted but cannot be completely vaporized in the plasma torch. The setting parameters are individual and correspond with the particular composition of the feeding powder. Hence, the optimal parameters are mainly in the case of novel materials assessed experimentally and the proper setting of the system is dependent on the experience of the operators. Suitability of material for plasma spraying can be validated only by practical experience – a fact that was confirmed also in this thesis.

Plasma spraying includes rapid heating and melting of material, followed by cooling and consolidation in one process. This sequence of phase changes frequently causes a metastable character of newly-formed coatings. As it has been already mentioned previously, the physicochemical properties of the feeding powder strongly influence the result. Properties that can negatively affect the plasma spraying process are, for example, the following: the content of volatile components, structurally bounded water, the decomposition of the material in the plasma and its selective evaporation, sublimation, improper temperature interval of solid and liquid, or incongruent melting. The elimination of bounded water in the feeding powder is an energy-demanding process and the proper melting of particles is then more difficult. Each of the factors or a combination of them has to be considered, and the final suitability of the material for plasma spraying needs to be validated.

According to these facts, the results of plasma spraying are often unstable and nonstoichiometric materials with different phase and chemical composition in contrast to the original material. Partial improvement of material properties, e.g. stabilization of individual phases, enhancement of crystallization process, or healing of the defects in the crystal lattice, consists of annealing of the material after deposition. The subsequent application of annealing of the material has several advantages, e.g. the applications of materials with coatings in thermally loaded processes where there may be changed in the stoichiometry or even crystal lattice stability that strongly affects the resulting volume of the loaded material.

2.2 Common Materials in the Plasma Spraying Technology

The selection of material suitable for plasma spraying technology is dependent on the required quality and stability of the coating. The desired properties certainly include good meltability, stability in the plasma (e.g. decomposition- and sublimation-free material), and persistence to oxidation and reduction processes. Nevertheless, some applications utilize only material vulnerable to the decomposition in the plasma.

Ceramic and metal are the most frequently used materials for the coatings. The practical application provides also coatings created from the combination of both, ceramic and metal materials, e.g. cermets, functionally graded materials (FGM) or two- or multi-layered coatings combining more properties (e.g. combination of a lower layer with good affinity to the substrate and an upper layer with thermally insulating properties) [7]. Other examples include hard and abrasion-resistant layers (Cr_2O_3, corundum, spinel), chemically stable layers (corundum, zirconia, Cr_2O_3), high temperature and thermal-shock resistant layers (zirconia, mullite), and layers with good thermal insulating properties (zirconia, mullite) [8]. Ceramic coatings have usually better thermal insulating properties than metal coatings and they also have a higher resistance to oxidation, corrosion, and abrasion factors [7]. They also serve as an electric insulator laying on a highly electrically conductive metal substrate (corundum, synthetic silicates, annealed TiO_2).

One of the longest and most frequently used materials for plasma spraying is synthetic corundum (α-Al_2O_3, alumina) producing hard and erosion and chemically stable alumina coatings suitable for anti-wear and anti-corrosion applications. The advantages of corundum utilization as the feeding power for the production of the coatings include its relatively good accessibility with economic benefits. The main disadvantage of corundum constitutes in thermal instability since higher temperatures induce polymorphism accompanied by volume change and consequently the lowering of properties. Hence, the feeding powder is enriched by additives that stabilize the most optimal trigonal α phase [9].

An interesting member of the alumina-based family of materials is an eutectic ceramic Eucor (the mixture of corundum, baddeleyite, and glass; Al_2O_3–ZrO_2–SiO_2). The Eucor ceramic is mechanically stiff and abrasive-, high-temperature- and chemically-resistant. The Eucor products are therefore used in industrial facilities, e.g. abrasive-resistant filling in the pipelines and the furnace lining in the metallurgy and glass industry [10]. The Eucor has also been successfully prepared in the form of coatings [11; 12].

Important material is also synthetic zirconium oxide, which is nowadays the most utilized material used as a heat barrier (chapter 2.2.1). The other materials applied in the industry are oxides (e.g. Cr_2O_3, TiO_2), silicates, borides, or carbides with good mechanical and chemical-resistant properties, low reactivity to molten metals and stability in oxidizing or reducing atmospheres they are suitable for corrosion and wear resistant coatings [13; 14; 15].

All the mentioned ceramics are before application manufactured from the original materials. The production often consists of multiple pre-treatment including melting, chemical separation, filtration, etc. These processes are highly energy-demanding and often hazardous for the environment and facility employees. Thus, application of natural geomaterials as alternative to the above mentioned ceramics have been studied.

2.3 Alternative Materials in the Plasma Spraying Technology

Plasma spraying of geomaterials has already been studied a little as it is summarized in the following overview.

Basalt, the most common volcanic rock type on Earth, is a gray to black fine-grained igneous rock with a low content of SiO_2, with main composition from plagioclase minerals, often with the olivine occurrence. Basalt is characterized by high abrasion-resistance properties, hardness, and toughness. It is utilized for the casting of amorphous products such as pipes and tiles and the production of mineral wadding used as soundproof and fire-stopping insulation [16]. Chráska et al. [17] produced the basalt coatings with the utilization of several techniques of thermal spraying: the water-stabilized plasma torch (WSP), high velocity oxygen fuel spraying (HVOF), and common atmospheric plasma spraying (APS) [18]. The results indicated amorphous basalt coatings with surprisingly low porosity around 3 %. Bayrak and Senol [16] were concerned with the crystallization kinetics of plasma-sprayed basalt. The authors studied the problem with differential thermal analysis (DTA) and revealed that amorphous plasma coatings can be transformed into crystalline ceramics during the annealing process. They prepared the coating on the stainless steel substrate with the bondcoat from NiAl and subsequently they burned it for 1 – 4 h at the temperature range of 800 - 1000 °C. During the annealing process mainly the mineral augite crystallized, giving a semi-amorphous structure to the newly-formed material. In the other experiment, the authors pointed out that longer crystallization time causes a reduction of the coating adhesion to the substrate [19]. Another amorphous basalt coating on the stainless steel substrate with the NiAl bondcoat was prepared by the authors Ercenk et al. [20]. The authors confirmed the presence of augite, ferrous diopside, albite, andesine, and moissanite minerals after burning at the temperature range of 800 – 900 °C. Furthermore, in the DTA apparatus, the authors revealed that the addition of commercial SiC causes a decrease in the activation energy of crystallization. The authors Ageorges et al. [21] investigated the possibility of spraying of the mixture of basalt and Cr_2O_3 with the aim of reduction of the brittleness of the pure Cr_2O_3.

Plasma coatings were successfully prepared from a number of minerals that are for specific optical and mechanical properties called precious or semi-precious stones and they are widely popular for jewellery production. Among precious minerals suitable as the raw materials for the coatings are represented by certain types of garnets with the general formula $X_3Z_2(SiO_4)_3$, where X is a divalent cation (Ca^{2+}, Mg^{2+}, Fe^{2+} or Mn^{2+}) and Z is a trivalent cation (Al^{3+}, Fe^{3+}, Cr^{3+}, V^{3+}, Zr^{3+} or Ti^{3+}). Garnets crystallize in the cubic system and are characterized by a high refractive index, high specific weight, and hardness (6.5 – 7.5 on the Mohs scale of mineral hardness) [22]. Due to their unique properties such as low thermal conductivity, good phase stability, and hardness, garnets are utilized in high-temperature processes and as an abrasive material in many industrial applications. The disadvantage of garnets is low CTE [8]. The Fe-garnet almandine, Mg-pyrope, and Fe-Ca series andradite-grossular were sprayed mainly as amorphous coatings with the cohesion to the substrate comparable with the coatings prepared from the corundum [23; 17].

Another mineral also from the silicate group is cordierite ($Mg_2Al_3(AlSi_5)O_{18}$), which is characterized by high hardness (7 - 7.5 on the Mohs scale), low thermal expansivity, and thermal stability [24]. Cordierite has been successfully manufactured into a form of fire-resistant material and electrical-engineering ceramic. Authors Chráska et al. [25] prepared free-standing cordierite in their experiment. Another study published by Neufuss et al. [26] deals with the preparation of cordierite coatings as well. The authors detected a decrease of CTE after the burning of the cordierite material at the temperature of 1250 °C.

Olivine (Mg^{2+}, Fe^{2+})SiO_4 is a common mineral from the basic igneous rocks; the main isomorphic series include two end members – Mg-olivine forsterite (Mg_2SiO_4) and Fe-olivine fayalite (Fe_2SiO_4). Olivine is utilized in metallurgy, chemical industry, for technical glass production, and as an abrasive material [22]. Ctibor et al. [27; 28] used olivine (forsterite and fayalite) as a raw material for free-standing plasma coatings. The authors stated that dielectric properties in the form of coatings are better than in the bulk material and the quality can be compared with the coatings prepared from synthetic corundum.

The minerals zircon, andalusite, diopside and tourmaline mentioned in next chapters are also from the group of the precious minerals.

Furthermore, semi-crystalline coatings were prepared from the calcium inosilicate wollastonite ($CaSiO_3$) which typically occurs in calcareous rocks affected by contact metamorphism. The study [29] focused on the shape of the particles in the feeding powder and confirmed that the spheroid shape modified in advance showed better properties in contrast to the unmodified powder.

Clay mineral pyrophyllite $Al_2Si_4O_{10}$ $(OH)_2$ in the form of spherical granules was also utilized for thermal spraying (APS and Vacuum Plasma Spray, VPS) by authors Kim et al. [30].

Bhuyan et al. prepared coatings from the mixture of fly ash (a waste product from a coal-fired power station) and bauxite (10 – 20 %) sprayed on a copper substrate. The authors revealed that the higher content of bauxite in the feeding powder increases the porosity of the coating and decreases its microhardness. Nevertheless, such coatings are bulkier [31] and Al_2O_3-richer [32]. Composite coatings prepared from the mixture of fly ash and quartz [33] or ilmenite ($FeTiO_3$) [34] were prepared similarly.

2.3.1 Zircon

The long-standing studied material in terms of plasma spraying is tetragonal mineral zircon ($ZrSiO_4$). Zirconium silicate is found in nature associated with acidic igneous rocks, such as schists, gneisses, syenites, and granites [35], from which zircon sand forms through weathering. Well-known secondary deposits of zircon are zircon sands on the beaches in Australia, southwest India, South Africa, and other places. Nevertheless, beside zircon, the deposits also contain other heavy minerals (e.g. rutile, ilmenite, monazite, garnet, kyanite) [36; 37]. After additional treatment, when impurities are separated, zircon sand is used as one of the technologically important oxide ceramic materials.

Zircon has good stability against thermal shocks and chemicals and it is also characterized by its refractoriness, high melting point (2190 °C), hardness (7.5 on Mohs scale), abrasion-resistance, low wettability, low thermal conductivity, and expansivity [22]. In metallurgy, zircon is used as a fire-resistant material for the production of glaze, enamels, electrotechnical ceramics, furnace lining, melting pots, and protective layers against thermal or chemical loading [37; 35]. Zircon is also a very popular mineral in the designing of jewellery as an above-mentioned gemstone.

Zircon is a mineral from the silicate group and above 1676 °C it decomposes to the tetragonal ZrO_2 (tetragonal zirconia, t-ZrO_2) and amorphous SiO_2. The newly-formed phases can persist due to rapid cooling also in coatings [38; 39]. Moreover, after annealing at the temperature of 1500 °C, both phases tend to react and create zircon silicate. The existence of both phases in the coating leads to an increase in resistance against thermal shocks and corrosion [37]. Hence, in comparison to synthetic zircon oxide, natural zircon could represent

an alternative raw material for thermal barrier coatings (TBC) or more widely for environmental barrier coatings (EBC).

ZrO_2 is up to temperature 1170 °C at atmospheric pressure monoclinic (m-ZrO_2). Above this temperature, it transforms into the tetragonal phase and after an increase in temperature above 2370 °C, it transforms into the cubic crystal lattice, and eventually, at higher pressures and temperature above 2680 °C, it transforms to the orthorhombic phase. The most utilized form of synthetic zircon in plasma spraying is its cubic polymorph. Hence, to preserve the cubic crystal lattice during the transformation process, 8 % Y_2O_3 has to be added and the final products yttria-stabilized zirconia (YSZ) or fully-stabilized-zirconia (FSZ) are then used. For the partial stabilization of cubic ZrO_2, lower amounts of Y_2O_3 (4 - 8 %) can be used, and the final product is known as partially-stabilized-zirconia (PSZ). The other compounds suitable for the stabilization of cubic ZrO_2 are oxides of dysprosium, hafnium, calcium, or magnesium [37]. Although the YSZ is widely used, new materials are subjected to the investigation as an alternative to economically-demanded yttrium oxide and pure ZrO_2.

Zircon plasma coatings manufactured from natural material were studied by Ramaswamy et. al. [40]. The authors prepared the layers on the stainless steel substrate with the bond coat from NiCrAlY, which balances differences between thermal expansion coefficients (CTE) of the coating and the substrate. Self-supporting zircon material manufactured from the natural zircon sand was sprayed by the authors Kolman et. al. [23] and Chráska et. al. [25; 36].

2.3.2 Mullite

One of very significant engineering materials is mullite. Mullite (general formula $Al_6Si_2O_{13}$) is also a mineral from the silicate group, which forms during regional or local high-temperature metamorphosis from the Cenozoic (tertiary-aged) clayey rocks rich in aluminum. Mullit exists in two stoichiometric forms: $3Al_2O_3 \cdot 2SiO_2$ (furthermore labelled as ‘‘3/2’’) or $2Al_2O_3 \cdot SiO_2$ (‘‘2/1’’) and it can contain traces of impurities such as Ti, Fe, Na, and K [41]. Mullite is characterized by low specific weight and low thermal conductivity, high temperature, and chemical stability and its mechanical strength [7]. The mullite layers are less vulnerable to the failure after thermal shock loading in contrast to layers manufactured from zirconia (YSZ). This phenomenon is caused by lower CTE in mullite layers. Another advantage is higher resistance against oxidation [7]. Mullite has been successfully utilized in glass and ceramic industry as fire-resistant ceramic, furnace lining, or for EBC applications [41]. Nevertheless, mullite rarely occurs in a pure form in nature but it is possible to produce it from several natural raw materials.

The natural raw mineral for the mullite production is represented by andalusite (Al_2SiO_5), which occurs in pegmatites, contact schists, or mica schists. Andalusite is processed into a form of special mullite ceramics with fire-resistant, mechanically, and chemically resistant properties. More than 90 % of andalusite transforms into the mullite at temperatures between 1315 and 1550 °C [22]. Authors An et al. [42; 43; 44] sintered andalusite for 4 h at the temperature of 1480 °C and prepared material which contained 80 % of mullite and 20 % of glass phase. They removed the undesirable amorphous phase by adding powdered Al_2O_3 and burning at the same temperature. They spray the obtained material on two substrates - on stainless steel and nickel alloy with the bondcoat from NiCrAlY.

Another material that is potentially suitable for the mullite production appears to be kaolinite, which was studied in this thesis. Kaolinite is a widespread mineral and constituent

of many porcelain and ceramic products, especially in the branch of utility ceramics. Kaolin, relatively pure clay, has been widely used in ceramic industry for centuries [45]. Kaolin is a white sedimentary rock originating from chemical weathering (kaolinization) or by hydrothermal alteration of rocks rich in feldspar – mainly granites, pegmatites, and arkoses. Kaolin is constituted by the mineral kaolinite from more than 80 %, accompanied with silica and a variety of clay minerals, micas, feldspar and others according to the nature of the mother rock.

Before using kaolinite in some applications, heating is desirable. This treatment is called dehydroxylation or calcination. It runs initially between 550 and 750 °C, where dehydroxylation takes place, i.e. bonded water is released [46]. At the same time, Al-octahedrons of the clay mineral are reformed to Al-tetrahedrons. Stable finely crystalline kaolinite transforms to metastable and non-crystalline metakaolinite this way [47; 48; 49] (table 1). If the temperature of treatment rises over 900 °C, crystalline mullite ($Al_6Si_2O_{13}$), spinel ($MgAl_2O_4$) or γ-Al_2O_3 with amorphous silica (SiO_2) are formed. This process depends on the content of alumina and silica.

Table 1. Transformations in kaolinite structure during firing, based on literature [50]

Step no.	**Temperature [°C]**	**Change**
I	Up to 180	Loss of superficial and adsorbed water
II	180–500	Dehydroxylation of the clay structure
III	600–800	Destruction of bonds and collapse of the clay structure
IV	900–1000	Recrystallization to a new high temperature phase (mullite)
V	1850	Melting [51]

Plasma spraying of such material as kaolin, exhibiting both following obstacles: structurally bonded water and a narrow melting interval; incongruent melting is considered extremely difficult. That is the main challenge of the presented thesis, when both of them, kaolinite with structurally bonded water and metakaolinite without it were plasma sprayed; metakaolinite was obtained by thermal treatment of natural kaolinite. Kaolin plasma sprayed coating could serve as a low-cost environmental barrier coating and once thermally transformed also as a low-cost thermal barrier coating for not extremely high temperatures and medium harsh environments [52].

Besides pioneer plasma spraying of kaolin, chemical reactions of the coatings with a silicate based dust were also studied in the thesis. After the main oxides forming such dust, i.e. CaO, MgO, Al_2O_3 and SiO_2, the label CMAS is usually applied for it [53]. Examination of chemical reactions of thermal barrier coatings with powders like CMAS is essential for application where aircraft parts covered by protective coatings are open toward the environment and dangerous dust during service. At high temperature, CMAS melts and infiltrates into the coating along the pores and microcracks rapidly. Upon cooling, CMAS penetrated into the coating, solidifies, and blocked pores develop a high stress level. Also, for other barrier coating applications like in land-based turbines, the interaction with CMAS is important to be studied.

2.3.3 Diopside

Diopside is a calcium and magnesium silicate with the chemical formula $CaMgSi_2O_6$. It is a monoclinic mineral from the diopside–hedenbergite series and forms solid solutions between $CaMgSi_2O_6$ and $CaFeSi_2O_6$. Diopside belongs to inosilicates, the calcic pyroxenes group, and its melting point is at 1390 °C. The origin of the mineral name is from two Greek words: "double" and "appearance" because the vertical zone of its crystal prism can be oriented in two ways. Diopside is common in metamorphic rocks. Transparent varieties of diopside are used as gems. The pyroxene structure consists of single chains of SiO_4 tetrahedra extending along the c-axis [54; 55]. Diopside as a material is among others suitable also for ceramic glazes [56] or as an addition to porcelain improving its sintering [57] and mechanical strength [58]. Diopside is considered a prospective material for covering Mg-based bone implants [59] or dental implants [60] to improve their durability. It could also serve as a host material for persistent luminescence nanoparticles [61].

In this study natural diopside $CaMgSi_2O_6$ was processed by plasma spray technique into self-supporting plates. It is the first documented plasma spraying of a diopside.

2.3.4 Tourmaline

Tourmaline (schorl), a mineral with a general chemical formula $NaFe_3Al_6(BO_3)_3Si_6O_{18}(OH,F)_4$ melts incongruently at temperatures varying roughly from 1050 to 1200 °C [62]. For the iron-rich types, the melting temperature decreases with increasing content of iron or magnesium. The specific weight is similar to e.g. diopside [54], around 3 g/cm^3 in dependence on actual iron-richness. Homogeneous glass can be prepared from high-iron tourmaline by quenching from about 1550 °C.

Tourmaline in the form of single crystal is piezoelectric [63]. Tourmaline can also be used in chemical catalysis. A commercial dye, Argazol blue, in an aqueous solution can be effectively discolored by mineral-catalyzed Fenton-like system of schorl (Fe-containing variety of tourmaline) and H_2O_2 [64]. In another work by the same team a discoloration of Rhodamine B dyeing wastewater is described [65].

Liu et al. [66] deposited a tourmaline film about 170 nm thick tourmaline on glass by ion-beam. However, tourmaline had never been processed by plasma spray before this work. Processing of materials that melt incongruently (in the case of tourmaline this is mainly because of the OH group in its structure) is a challenge for plasma spray technique with its typical rapid quenching (chapter 2.1). Plasma spraying offers deposition of silicate glasses on many kinds of substrates without thermal damage to the substrate [67; 68; 69]. Various silicates already have well-established application but these single-phase ceramics require sintering at a high temperature, which is sometimes a serious drawback. In the material the OH group and partly also F and Na tended to preferentially evaporate.

The current experiment is focused on spraying material with chemically bound water in its structure and exhibiting incongruent melting. Since the bound water is responsible for the incongruent melting, the key factor is to find spray parameters for melting maximum amounts of the powder mass.

2.3.5 Alternative Materials in Thesis

Based on the above described research, zircon will be investigated in the thesis because the pioneering studies need to be developed and further improved. Current research is

focused on natural $ZrSiO_4$ plasma sprayed by a water-stabilized plasma system. A combination of two feeding distances and three spray distances was utilized for spraying and the microstructure and basic properties of the prepared samples were evaluated.

Kaolin and clay shale were selected as a new materials potentially suitable for mullite production. Besides pioneer plasma spraying of kaolin, chemical reactions of the coatings with a silicate based dust were also studied.

Other completely new studied materials in the plasma spray field that the work deals with are diopside and tourmaline.

The conception of this thesis is based on five studies published in impacted journals. The results are arranged from simpler to more complex studied material based on the chemical composition and physicochemical properties influencing the plasma spraying process - specifically zircon, diopside, tourmaline, kaolin, and clay shale.

The author of the thesis actively participated in the experiment's planning, preparation of the specimens, and performed primarily thermal, and several optical analyses. The other experiments were carried out in co-operation with the supervisor-specialist and other scientific workers, and technicians, mainly in the Department of Material Engineering of the Institute of Plasma Physics.

3 Objectives of the Thesis

The aim of this thesis was to search for new natural materials suitable for plasma spraying that would be commonly available and will bring economic benefits in comparison with synthetic materials. The search for new candidates consisted mainly in testing the suitability of selected materials for the use in plasma spraying technology. The objectives of the work were therefore set as follows:

- The essential task was to prepare plasma coating from natural materials.
- The second task focused on the experimental testing of this new material, particularly investigation of thermal properties supplemented by the study of composition, microstructure and further more physicochemical properties.
- The additional goal of the work was to pay increased attention when choosing a material, to those geomaterials, from which the prepared coatings could compete with the coatings of synthetic mullite.
- Attention was also focused on the thermal stability of the newly prepared material.
- The effect of thermal post-treatment and the evaluation of eventual application of the material were studied too.

4 Experimental Part

Various minerals and rocks were studied from the physical and chemical points of view. The selected materials suitable for further investigation were gained in nature or from the providers. Each raw material was then crushed, eventually sorted to separate the impurities, milled, and sieved to the size fraction acceptable for plasma spraying (typically 40 - 180 μm).

Institute of Plasma Physics of the Czech Academy of Sciences is equipped with technologies that were used for the implementation of experiments, i.e. water stabilized plasma torch WSP® 500 with graphite cathode (WSP) and hybrid technique with water-argon stabilized plasma torch WSP®-H 500 with tungsten cathode (WSP-H). The details are described in chapter 2.1.

Stainless steel, or ceramic coupons used as substrates were grit blasted before spraying. Preheating of the substrates was applied just before spraying. A preheated substrate provides a better platform for the coating crystallization and reduces the amount of amorphous phase formed in the coating due to the slightly prolonged quenching time of the individual droplets; and spreading of splats is also enhanced [70].

Investigation of free-flight particles (FFP, i.e. passing through the plasma but not impacting the glass substrate) and individual splats sprayed with different setting parameters on microscopic glasses was performed prior to the spraying of coatings itself to optimize the device parameters (this process is described in detail in chapter 5.2).

The samples were prepared as coatings on stainless steel, carbon steel or ceramic substrates and/or as free-standing subjects (free-standing plates, FSP). The selected deposits for FSP forming were later removed from the stainless steel substrate by thermal cycling provided by repeated placement onto a kitchen heater and in liquid nitrogen (approximately -170/+100 °C).

As-sprayed coatings as well as free-standing plates were then investigated in terms of microstructure, mechanical properties, and thermal properties. The selected samples were thermally modified by annealing.

4.1 Powder Pre-Treatment, Plasma Spraying and Coating Post-Treatment

4.1.1 Zircon

Pre-milled zircon sand with a particle size of 0.5 to l mm was supplied by Westralian Sands Ltd., Australia, and later it was in-house milled and sieved for 40 to 70 μm feedstock, useful for thermal spraying by WSP.

The spray process was carried out to obtain self-supporting parts (similar to those referred in the literature [71]). A matrix of two feeding distances and three spray distances was applied to test the influence of these parameters (similarly to another work [72]). Zircon powder was thermally sprayed with parameters listed in table 2.

Table 2. Plasma spray parameters for zircon

Torch type	WSP
Power [kW]	154
Plasma-forming medium [l/min]	Water,22
FD - feeding distance [mm]	23; 28
SD - spray distance [mm]	200; 245; 290; (350)
Powder-feeding medium	Air
Substrate material	Al

After spraying, a post-treatment consisting of heating to 960 °C in air, dwell time 15 min, and subsequent cooling was applied. This temperature was high enough to remove aluminum-based substrates from the coatings and low enough to remain the coating intact, since zircon decomposes above 1676 °C into its basic components - zirconia and silica (with silica in a glassy form). It is just below the eutectic melting temperature in the zirconia-silica system, 1687 °C [73]. The treatment temperature was far below this temperature as well as below sintering temperature 1180 °C, equal to 0.7 of the melting point. Free-standing plates 1-2 mm thick were made by this approach and examined by subsequent tests [74].

4.1.2 Diopside

Coarse-grain natural diopside was crushed and sieved to obtain the feedstock powder for spraying (grain size 100 – 180 μm).

Preheating of the substrates to 300 °C was applied just before spraying. The coatings were produced using a WSP plasma spray system. The powder was fed in by compressed air through two injectors. Final feeding distance and spray distance used for spraying the coatings were 65 mm and 400 mm respectively. The deposited coating thickness was about 3 mm.

Annealing of the as-sprayed FSP was carried out in air in a laboratory furnace using two regimes. In both regimes temperature was set to 900 °C, heating as well as cooling were done in air at a rate of 7 K/min. The dwell time was 15 min in the first case and 30 h in the other case. The annealing temperature was chosen on the basis of the DTA results to be above the diopside crystallization temperature. The dwell times, first as the shortest possible and the other as a really long one, were selected for the observation how the annealing process changes the microstructure and crystallinity [75].

4.1.3 Tourmaline

Natural as-mined tourmaline was crushed and sieved to obtain the feedstock powder for spraying. The powder had a size distribution of 63 – 125 μm.

Stainless steel coupons, as well as ceramic tiles, were used as substrates for coating. The substrates were preheated to 300 °C. The coatings were produced using a plasma spray system with a hybrid stabilization WSP-H. The powder was fed in by compressed air through two injectors. Plasma spray parameters were adjusted using observation of single splats sprayed on non-treated surfaces of laboratory glass. A set of samples sprayed at SD 250 - 350 mm and FD 40 - 100 mm was prepared. The thickness of the deposited coatings was from 0.5 to 2 mm. Several deposits were later removed from substrates to form self-supporting plates.

Annealing of the as-sprayed FSP and some coatings on ceramic tiles was carried out in air in a laboratory furnace using two regimes. In both regimes, the temperature was set to 1000 °C, and heating as well as cooling were done in air at a rate of 7 K/min. Dwell time was 30 minutes in the first case and 8 hours in the other case. Annealing temperature was chosen on the basis of the thermal analysis results so as to be above the tourmaline transformation temperature. The short and long dwell times were chosen in order to observe how much the annealing process changes the microstructure, crystallinity, and mechanical aspects of tourmaline [76].

4.1.4 Kaolin

Kaolin for this study comes from the Kaznějov deposit in western Bohemia, Czech Republic. The parent rocks are Upper Carboniferous arkose and arkose sandstone. The main components are quartz (50–70 %) and kaolinite (20–30 %) with accompanying micas and feldspar in various intensity of disintegration. Accessories are mostly represented by Ti-ilmenite, rutile, leucoxene, anatase, tourmaline, garnet and Fe-oxides and hydroxides. The main product of the quarry is floated kaolin which was used in the experiment.

Thermal treatment of the powder to reform kaolinite powder (KP) into metakaolinite (MK) and to remove bonded water, was done in a laboratory furnace, in air atmosphere at 700 °C (set on the basis of DTA), with the dwell time 30 min and ramp up and down 7 K/min. The both materials were sieved.

Plasma spraying was done by a hybrid water-stabilized plasma torch (WSP-H). Preheating of the substrate for spraying was carried out by the torch, always to 120 °C, and between passes over the substrate the temperature was monitored and maintained at 125 °C. Torch current 500 A was applied and powder feeding ensured by air. Spraying of the final coating based on the original kaolinite powder was performed at the feeding distance 55 mm and spray distance 270 mm onto a stainless steel substrate, using 16 passes over the substrate with the final thickness about 0.85 mm (i.e. thickness per pass 53 μm).

Spraying of the coating based on the treated powder (MK) was performed by WSP-H using feeding distance 50 mm, spray distance 250 mm and 26 passes over the substrate to gain thickness about 1.50 mm (i.e. thickness per pass 60 μm).

Depending on the substrate material, the coatings of KP and MK adhered on the substrate or were released during cooling to form free-standing plates. Stainless steel was used for this, whereas other materials like carbon steel or ceramic tiles formed permanent substrate-coating systems.

Reactivity of the coating with calcium-magnesium-aluminum silicate (CMAS) powder was tested. The CMAS powder was Ultrafine Test Dust "Arizona desert sand" produced by Powder Technology (Arden Hills, MN, USA). The dust powder was mixed with ethanol and applied on the coating surface by a brush. Then this sample was dried in air at room temperature for 3 hours and subsequently annealed in air for dwell time of 4 hours at 1150 °C [77].

4.1.5 Clay Shale

Natural raw material from which the production of mullite was attempted in this thesis, accessible in the Czech Republic, Germany, Poland, etc., around the coal basins, is a clay shale, layered silicate rock formed by sedimentation of mud. It does not have an unambiguous English name (closest is ''shale,'' in Czech it is called ''lupek,'' ''letten'' in German) [78]. It contains the mineral kaolinite $Al_2O_3 \cdot 2SiO_2 \cdot 2H_2O$ as the major fraction (around 95 %) and several percents of Fe_2O_3 and TiO_2 and minute amounts of alkaline oxides [52]. This material will be labelled in the following text by its commercial brand name of the supplier CLUZ, Inc., Nové Strašecí, Czech Republic, i.e. A111VHR for the delivered one and A111 for the used feedstock [78].

The excavated raw material was calcined at 1350 °C and afterward milled and sieved into size fraction of 0 - 100 μm was chosen, which was then additionally sieved at IPP and only the powder size fraction of 40 - 80 μm was selected.

The WSP system was used for spraying with two external movable powder injectors and the feeding rate of 7 kg/h. Feeding distance was changed between 40 and 90 mm and the spraying distance between 250 and 450 mm. Spraying was monitored using DPV-2000 instruments (TECNAR, St-Bruno, Canada), capable of measuring simultaneously the temperature, diameter and velocity of sprayed particles during their flight. Strips from plain carbon steel (2.5 x 25 x 120 mm) preheated to 150 °C were used as substrates for coatings. Besides coatings with thickness of 0.8 mm, free-flight particles were collected at the distance of 1500 mm of the nozzle and finally the free-standing plates were prepared as well. FSP in the form of plates with thickness around 2 mm were striped out from a coated stainless steel mandrel preheated before coating process to 300 °C [79; 80].

Since it was found that the A111 coatings are basically stable up to 800 °C, further attention was given to annealing at higher range of temperatures. FSP strips were inserted into a furnace preheated to a given annealing temperature T_a between 800 and 1400 °C, annealed for 2 or 30 min in air and cooled down in air [78].

4.2 Analytical Methods

Preliminary **X-ray diffraction** (XRD) analysis of clay shale samples was carried out with diffractometer D500 (Siemens, Germany) coupled with PDF-2 ICDD database, using Cu-Kα radiation over 2 h range of 10 ° to 100 ° and point detector. Then XRD ‘‘in situ’’ experiment was made using the high temperature chamber with platinum heating strip on D8 Discover (Bruker, Germany), a more recent XRD machine, in the temperature range of 800 - 1200 °C with 10 °C steps between 900 and 1000 °C (High Temperature X-Ray Diffraction, HTXRD); 2 h range was from 10 to 50 °, heating rate was set to 10 K/min and dwell time for temperature stabilization at each step was 1 min. Residual stresses in selected samples were determined assuming equibiaxial stress state. Due to the lack of suitable diffraction profile at higher 2θ, the so-called ψ diffractometer setup coupled with parallel beam geometry was employed. The proper diffractometer alignment was checked by measuring stress-free powder tungsten sample giving normal stress of 0.3 ± 12.3 MPa [78].

Other samples were were measured also on the D8 Discover diffractometer in Bragg–Brentano geometry with Cu-Kα radiation and 1D LynxEye detector. Precise alignment of the sample surfaces was done by laser check. Topas software 4.2 version was used for the quantitative Rietveld analysis. The amorphous material was assumed to be of the same chemical composition, so the crystallinity was computed from integral intensities of crystalline phases and amorphous halo only.

To determine temperatures of the phase changes **differential thermal analysis** (DTA) and **thermogravimetric** (TG) curves were obtained by simultaneous thermal analyzer (TG-DTA, Bähr, Germany) using a B-type thermocouple. Thermal treatment of the powders and coatings manually milled to powder took place in alumina crucibles. As a reference substance α-Al2O3 powder (size < 60 μm) was used. The results were corrected by blank subtraction.

Samples of zircon and clay shale were analyzed by TG-DTA 92 machine (Setaram, France). Measurements of zircon were performed with a dwell time 15 min on the maximal temperature. Analysis of clay shale was complemented by measurements of the heat flow (**differential scanning calorimetry**, DCS) as functions of temperature (fine steps of 25 K between 800 and 1000 °C) and heating rates (2, 5, 10, 20, and 35 K/min) on the same machine.

The parameters of the individual experiments are shown in table 3. All the treated samples were re-analyzed by XRD.

Table 3. Parameters of DTA and TG measurements

Material	Device	Sample mass [mg]	Maximal temperature [°C]	Heating rate [K/min]	Atmosphere	Flow rate [l/h]
Diopside	Bähr	40	1300	10	argon	5
Tourmaline	Bähr	30	1100	10	argon	5
Kaolin	Bähr	20	1600	10	synthetic air	5
Clay shale	Setaram	50	1600	10	argon	N/A
Zircon	Setaram	50	1600	5	argon	N/A

Thermal expansion of the as-sprayed coatings was studied by a vertical push rod dilatometer TMA Setsys 16/18 (Setaram, France). Measurement was done on free-standing samples about 10 mm long in a controlled air flow. Heating rate of 10 K/min (5 K/min for clay shale) was used in the temperature range 30 – 1600 °C. A load of 5 g was applied. The obtained data were corrected by blank subtraction.

Thermal diffusivity (TD) of the free-standing coatings was measured by a laser flash apparatus LFA 1000 (Linseis, Germany). The measuring was held in vacuum at a room temperature and at temperatures from 100 °C to 1300 °C. The resulting values of thermal diffusivity were calculated as an average from five measurements at each temperature.

Thermal diffusivity of clay shale was registered by FL-3000 (Anter, USA) in nitrogen atmosphere from 100 °C to 1000 °C. The resulting values of thermal diffusivity were calculated as an average from three measurements at each temperature. Bulk mullite specific weight [81] was used for **thermal conductivity** (TC) calculation.

Sample size of all the samples was 10 x 10 mm and thickness was about 1 mm. The coatings were slightly grounded to obtain smooth surface on which a thin layer of colloidal graphite was applied. A thin interlayer of gold was applied on kaolin samples before covering with colloidal graphite.

Metallographically polished cross sections were prepared from as-deposited coatings. The samples were sectioned using a diamond cutting blade and cross sections were mounted in a low viscosity resin. Grinding and polishing of the samples were carried out using an automatic polishing system Tegramin-25 (Struers, Denmark).

Cross sections of the samples were observed in a **light microscope** Neophot 32 (Carl Zeiss SMT, Germany) and in two **scanning electron microscopes** (SEM):

Kaolin samples were studied in scanning electron microscopes Mira II LMU (Tescan, Brno, CZ) equipped with an energy dispersive X-ray detector (EDX). Prior to observation, the specimens were coated by a thin layer of gold (powders and coatings surfaces) or carbon (polished cross sections) in a sputter coater to ensure signal stability and specimen discharging. The microstructure was investigated with a back scattered electron (BSE) detector, since BSE provide better stability of signal necessary for powder investigation. The accelerated voltage was set on the 15 kV and the working distance was changed during scanning from approximately 13 to 22 mm.

Other samples were studied in a scanning electron microscope EVO MA 15 (Carl Zeiss SMT, Germany) with Quantax system (Bruker, Germany) using charge compensation mode with a pressure of 30 Pa and equipped with an EDX (SDD detector XFlash® 5010).

Porosity was studied by the light microscopy on polished cross sections. Micrographs were taken with a CCD camera and processed using the image analysis (IA) software Lucia G (Laboratory Imaging, Prague, Czech Republic). Porosity levels were determined from images by differentiating between porosity and bulk coating in gray levels. Ten images of microstructures taken from various areas of the cross section for each sample were analyzed. In addition to a simple quantification of porosity, other features of the coatings were also examined. The magnification used was 250 in all cases allowing an analysis of all objects with a size of 3 microns or more. For a better description of the microstructure, certain additional criteria were introduced: Equivalent diameter (ED) represents mean size of voids detected (approximation at 2D projection); Circularity (CIR) describes the shape of voids when ‘‘1’’ represents a perfect circle and ‘‘0’’ the linear projection; it is calculated for all 10 images. Minimal circularity represents the minimum of CIR detected for an individual void within all measured frames.

Vickers **microhardness** of the coatings was measured on polished cross sections by optical microscope equipped with a Hanemann head mounted on the light microscope with fixed load 0.5 or 1 N and the Vickers indenter on a microhardness head (Carl Zeiss, Germany) attached to the light microscope Neophot 32. The mean value of microhardness was calculated as an average from 20 indentations each applied over 15 seconds.

Surface roughness (R_a) was determined by a contact method using the Surtronic 3P (Taylor-Hobson, UK) apparatus on a length of 13 mm repeated 5 times on various parallel tracks. **Slurry abrasion response** (SAR) of coatings was measured with respect to the ASTM standard [82]. SAR test is based on measuring the mass loss rate of a self-supporting ceramic while lapped in slurry. The test was run for more than 9000 in 4 equal increments, with mass loss being measured at the end of each increment. The applied force was 22 N per specimen. After each run the specimens were ultrasonically cleaned and weighed. The slurry consisted of 150 g of water and 150 g of alumina powder having a size of 40 to 50 mm. Accuracy of measurement is approx. 75 %. The results are expressed as inverse wear rate (IWR).

Reflectance measurement was performed using an ultraviolet/visible/near-infrared (UV/Vis/NIR) spectrophotometer (Shimadzu, Japan). Prior to the measurement a calibration process was conducted using a BaSO4 reference mirror in order to minimize the error from the environment. The accuracy guaranteed by the manufacturer is ± 0.3 nm, independent of actual wavelength, and the uncertainty of measurement was less than 0.2 %. The wavelength of incident light used for the reflectance measurement was in a range from 250 nm to 2000 nm and the measured area was about 2 cm^2.

Specific weight and **open porosity** was determined by helium pycnometry (AccuPyc 1330 V3.03; Micromeritics, USA). Specific weight was examined also by Archimedean (i.e. water immersion) techniques.

X-ray fluorescence (XRF) was performed using spectrometer Axios (Panalytical, NL) equipped with Rh tube, 4 kW generator, 3 collimators, 8 crystals, and data processed with the software Omnian for a standard-less analysis.

Powder size measurements were carried out on the laser particle size analyser Mastersizer 3000 (Malvern, UK).

5 Results and Discussion

5.1 Zircon

Microimages of a polished cross section prepared from as-sprayed zircon coatings are given in figure 3. Each kind of defects typical in plasma sprayed coatings is present also in the samples. Main defects inherently present are visible: porosity (black) - interlamellar elongated as well as intralamellar globular; unmelted particles (circular and often also with globular pores inside, see the bottom left corner in figure 3b); and intersplat boundaries with a dominant horizontal orientation (i.e. perpendicular to spray direction). Those features were present in all coatings without any significant changes when spray parameters were modified.

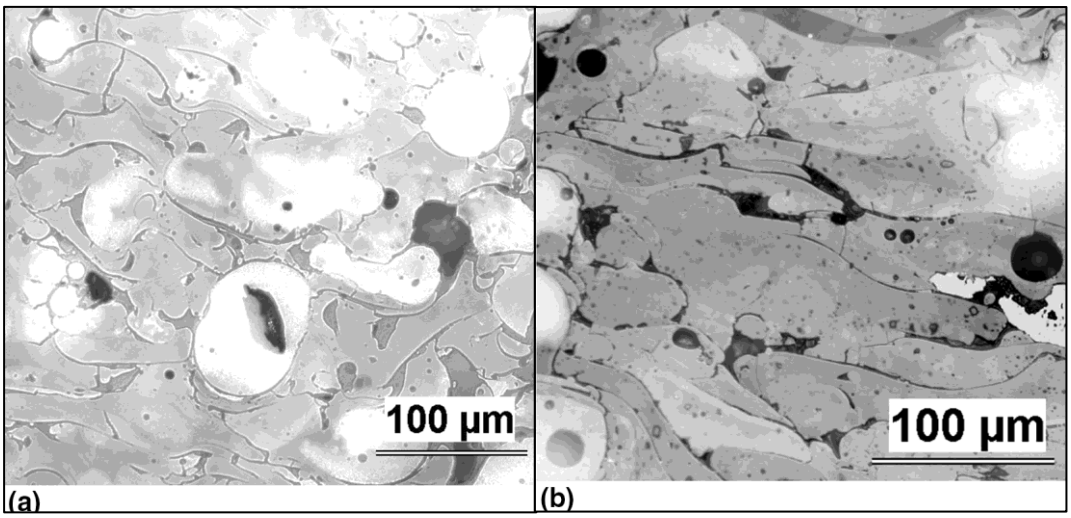

Figure 3. Cross section of two $ZrSiO_4$ coatings produced by WSP spraying: 28-290 (a) and 23-200 (b) (light microscopy)

Table 4 shows the porosity quantification. TiO_2 - rutile sprayed form natural rutile powder [4] as a representative of non-silicate ceramics and olivine-forsterite [83] as a representative of silicates are listed for comparison in table 4 with their porosity parameters; both are WSP sprayed coatings.

Table 4. Image analysis of pores in $ZrSiO_4$ coatings and comparison with different silicate coatings [84; 83]

Sample	Porosity [%]	ED (pore size) [µm]	Pores per mm^2	CIR	CIR-min
28-290	7.5 ± 2.7	7.90 ± 0.50	753 ± 174	0.42 ± 0.02	0.034
23-200	6.7 ± 1.8	11.35 ± 1.35	349 ± 131	0.51 ± 0.04	0.050
TiO_2-rutile	*4.3 ± 1.6*	*1.74 ± 0.21*	*446 ± 229*	*0.78 ± 0.04*	*0.093*
Olivine-forsterite	*14.2 ± 1.9*	*7.30 ± 0.40*	*991 ± 156*	*0.63 ± 0.01*	*0.066*

For zircon, a combination of the shortest FD (i.e. very high temperature at the feeding point) and shortest SD (i.e. high temperature at the impact point) should lead to high temperature of the material [85; 86]. It can be seen that zircon 28-290 (i.e. theoretically

‘‘the coldest’’ sample) exhibits medium porosity, relatively large pore size, and medium pores quantity per square millimeter. Low ‘‘mean circularity’’ (CIR) and ‘‘minimal detected circularity’’ (CIR-min) of pores are significant for zircon 28-290. This value is influenced first of all by the existence of intersplat (horizontal) flat pores. In contrast, zircon 23-200 (i.e. theoretically ‘‘the hottest’’ sample) has higher parameters CIR and CIR-min of pores. This signalizes lower quantity of the intersplat (horizontal) flat pores and thus better splat-to-splat contact. The sizes of its pores are even larger than for zircon 28-290.

However, the microstructures of both zircon samples look similarly, figure 3. Microhardness of the coating 28-290 was measured as 10.3 ± 1.1 GPa, and for the coating 23-200 it was 8.8 ± 2.1 GPa. This difference is also not a large one.

Figure 4 displays results of X-ray diffraction measurements. Phase identification showed the presence of two zirconia phases, i.e. monoclinic and tetragonal. A so-called amorphous halo indicating the presence of amorphous material within the irradiated volume is not observed. Rietveld quantitative and microstructural refinement, performed in TOPAS 4.2, of the diffraction data revealed approximately 27 and 17 wt.% of monoclinic phase in the top and substrate side, respectively, with the balance of tetragonal phase. Sizes of coherently scattering domains of both phases are similar, do not differ significantly for the analyzed areas, and are in the range from 10 to 20 nm as evaluated from diffraction peaks integral breadths by fundamental parameters line profile fitting approach. This is mirrored in the fairly broad diffraction profiles, typical for a nano-sized polycrystalline material.

The lattice refinement showed that the lattice parameters of the monoclinic ZrO_2 are similar (with differences not exceeding 0.015 Å) to those reported by Smith and Newkirk [87] for high purity baddeleyite. However, the lattice parameters of the tetragonal phase are substantially smaller when compared with standard values reported by Teufer [88], i.e. refined values of 3.600 Å and 5.195 Å for *a* and *c* lattice dimensions versus standard $a = 3.64$ Å and $c = 5.27$ Å from [88]. The ionic radii of Zr and Si in +IV state are 72 and 40 pm [89], respectively, and replacement of Zr ions by Si ions in tetragonal lattice will lead to smaller lattice parameters. The results of XRD analyses hence indicate that silicon atoms are not present as an amorphous matrix, but rather substitute Zr atoms in the crystallites of the tetragonal phase forming the so-called silica-substituted zirconia. This feature is significant for all spray parameter combinations used.

These conclusions are confirmed by Itoh who created $ZrSiO_4$, t-ZrO_2 and m-ZrO_2 in an equimolar mixture of amorphous silica and amorphous zirconia heated in furnace [90]. In addition, he claims that transformation of t-ZrO_2 to m-ZrO_2 appreciably occurs after the crystallite size of t-ZrO_2 exceeds a critical size around 200 Å (i.e. 20 nm). This is the crystallite size also detected within the current study experiment (10 - 20 nm). Itoh [90] considered 20 nm as a “threshold size” of tetragonal ZrO_2 crystallites, under which the tetragonal phase is preferred before monoclinic phase. The existence of a certain "critical size" of crystallites is confirmed also by other authors [91; 92]. The preservation of tetragonal zirconia maximal content down to the room temperature will be desirable for the engineering practice, since the phase transformation (t-ZrO_2 to m-ZrO_2) is accompanied by large shrinkage and limits the applicability of thermal barrier coatings. In fact, such fine crystallites are more typical when synthesizing ZrO_2 by the co-precipitation technique [92] then for any processing of $ZrSiO_4$ into ZrO_2 (plus by-product SiO_2). The receiving of even finer crystallites in the coating could be theoretically maintained by *i)* having $ZrSiO_4$ feedstock powder with even finer crystallites, or *ii)* cooling the as sprayed coating rapidly by e.g. a stream of cold water to enhance the (already high) cooling rate.

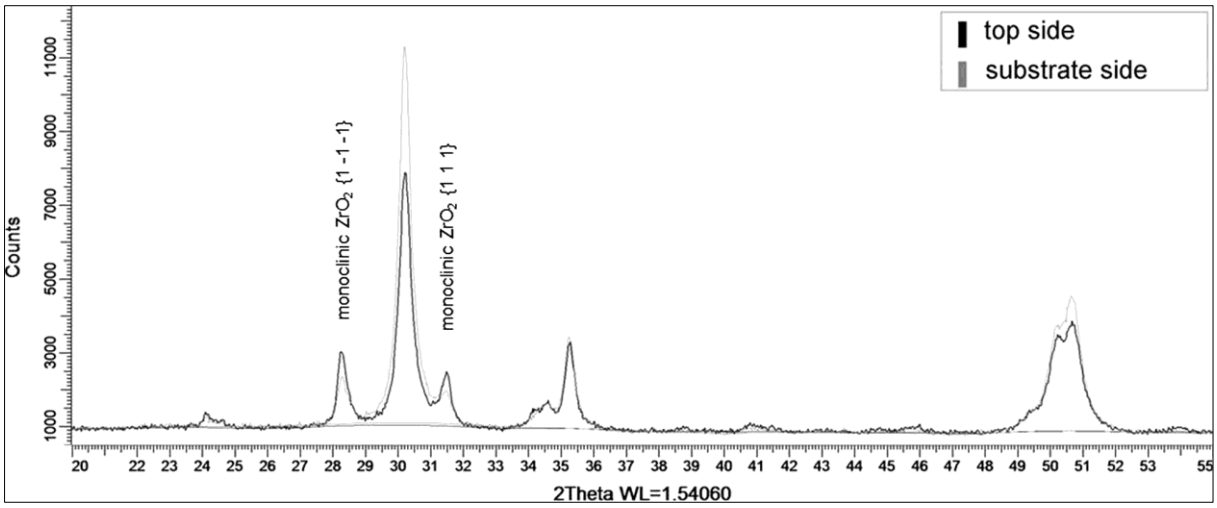

Figure 4. XRD pattern of $ZrSiO_4$ coating

Figure 5 displays the DTA analysis of the coating. Certain endothermic peak at 730 °C and exothermic peak at about 900 °C were observed similarly to Puclin et al. [93], which attributed these features to reordering of strongly disordered zircon.

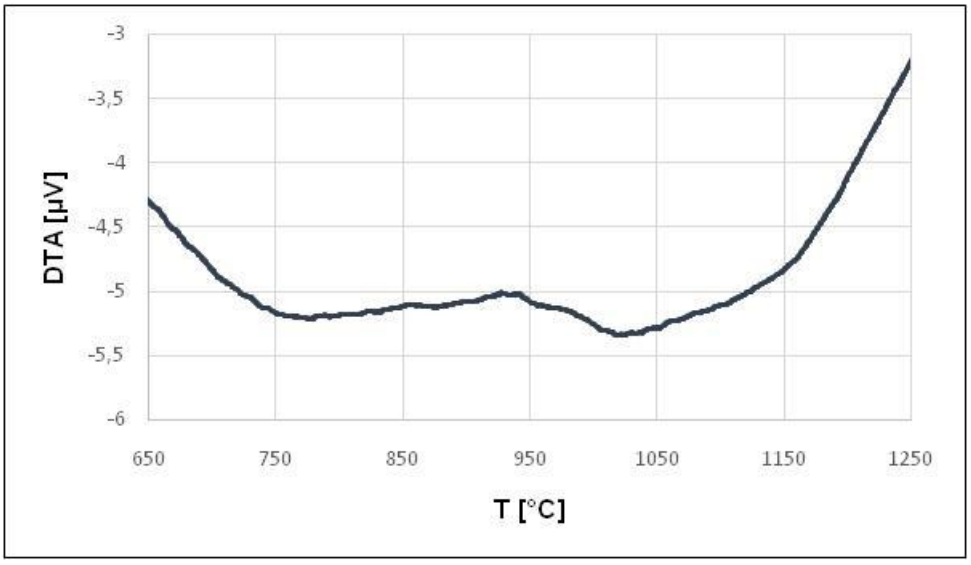

Figure 5. Detailed DTA curve of $ZrSiO_4$ coating

Conclusions for Zircon

Natural zirconium silicate $ZrSiO_4$ was plasma sprayed, whereas a set of two feeding distances FD and three spray distances SD was applied to test the parameters window for a sufficient quality coating. The results reveal that there is a combination of effects on the microstructure scale (splats, their contacts and defects) and also on the scale of lattice repeating units, where Si atoms are placed in the ZrO_2 matrix. This silica-substituted zirconia was revealed as very fine-grained with coherently scattered domains smaller than 20 nm. In the presented experiment as in the first one, silica-substituted zirconia with crystallites of the 10 - 20 nm size was prepared using plasma spraying technology which is the same implication for the phase transformations in ZrO_2 component as in a sintered material [90]. Zircon as an inexpensive material can substitute alumina, forsterite or steatite with similar microstructure in the form of plasma-sprayed coatings and free-standing bodies [74].

5.2 Diopside

Plasma spray parameters were adjusted using observation on single splats sprayed on non-treated surface of laboratory glass as following text describes. Figure 6 presents single splats sprayed from three different feeding distances at the fixed spray distance of 300 mm. For all FDs, variability in transparency of splats quite frequently represented by two major extremes – transparent splats and black splats – was observed. This can be attributed to a difference in chemical composition. However, such a difference is not manifested by different adherence to the glass – both splat types behave similarly.

For the shortest FD of 50 mm the splats were fragmented which signalizes impact in a too hot state and a too high velocity. If the FD was set on 70 mm, the splats frequently bounced-off (low impact temperature and velocity). The dark splats were apparently thicker (not optimally spread out) probably due to resolidification [94] and the transparent splats were surrounded by long "fingers" – at this distance the two sorts of splats did not behave equally. If an intermediate FD was chosen (60 mm), both splat sorts – dark and transparent – were circular. This indicated suitable conditions for the coating build-up at FD 60 mm. However, not only single splats character is the factor enhancing the optimization process because the cooling regime is not easily transferable to a different substrate material. Free-flight particles were observed too.

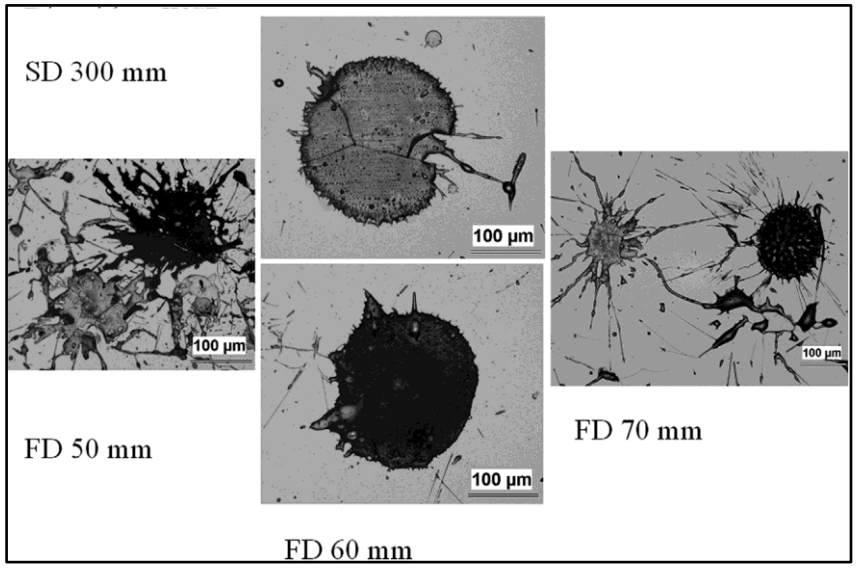

Figure 6. Optical micrographs of diopside splats on glass: FD 50 mm (top left) FD 70 mm (top right) and FD 60 mm (bottom)

Figure 7 shows the appearance of the feedstock (nominally 100 – 180 µm) and the FFP from three tested FDs. The feedstock is faceted and individual particles differ in colour, which could be again attributed to the difference in chemical composition. At the shortest FD (50 mm) the particles were irregular and fragmented because of a too high quenching rate. At the FD 60 mm the particles were well spheroidized which signalizes proper melting. At the highest FD 70 mm the particles were well spheroidized too and even more equal in size with the absence of substantially smaller spheres present at FD 60 mm.

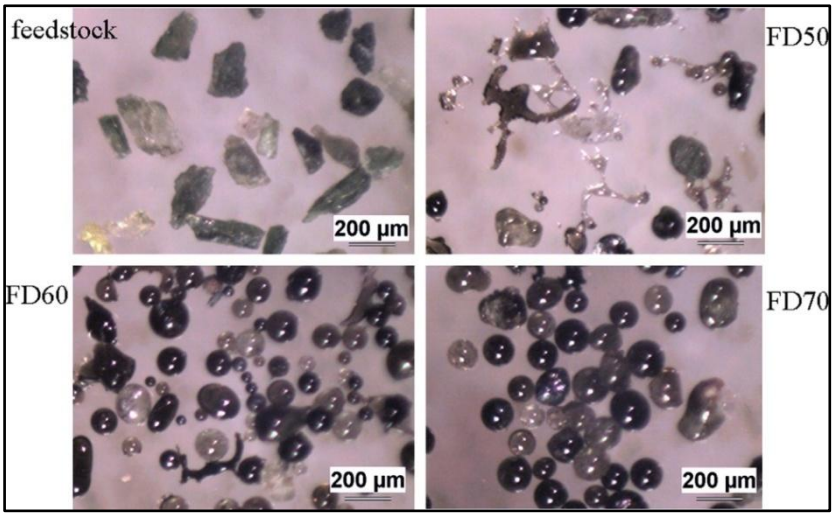

Figure 7. Optical micrographs of diopside feedstock powder and free-flight particles at feeding distance 50 mm, 60 mm and 70 mm

Finally, FD for substrate coverage equal to 65 mm as a compromise between the best appearance of single splats on glass and free-flight particles was selected. FFP at this FD were collected and the size and shape distribution was acceptable (figure 8 – left). However, certain proportion of irregular particles was present. The particles above 250 µm were separated by sieving and some fibers connecting two particles, as in figure 8 – right, were observed among the "largest" particle fraction obtained by this procedure. Based on previous experience, such a feature is typical for an amorphous material. Spray distance 400 mm was dictated by the steel substrate temperature evolution during preheating. Final feeding distance and spray distance used for spraying the coatings were 65 mm and 400 mm respectively [95].

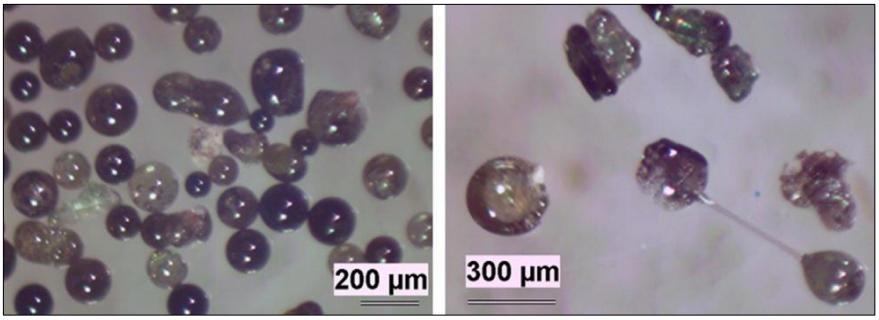

Figure 8. Optical micrographs of diopside free-standing plates at FD 65 mm non-sieved (left) and the separated size above 250 µm (right)

A typical microstructure of resulting as-sprayed diopside coatings is shown in figure 9 (surface) and figure 10 (cross section). A lamellar structure, typical for plasma sprayed coatings, can be seen with the presence of little number of unmelted particles in the coating. Presence of multiple cracks and predominantly globular pores was observed as well. The EDX spectrum is depicted in figure 11. Intensities of the main lines of all basic diopside-constituting elements are similar [75].

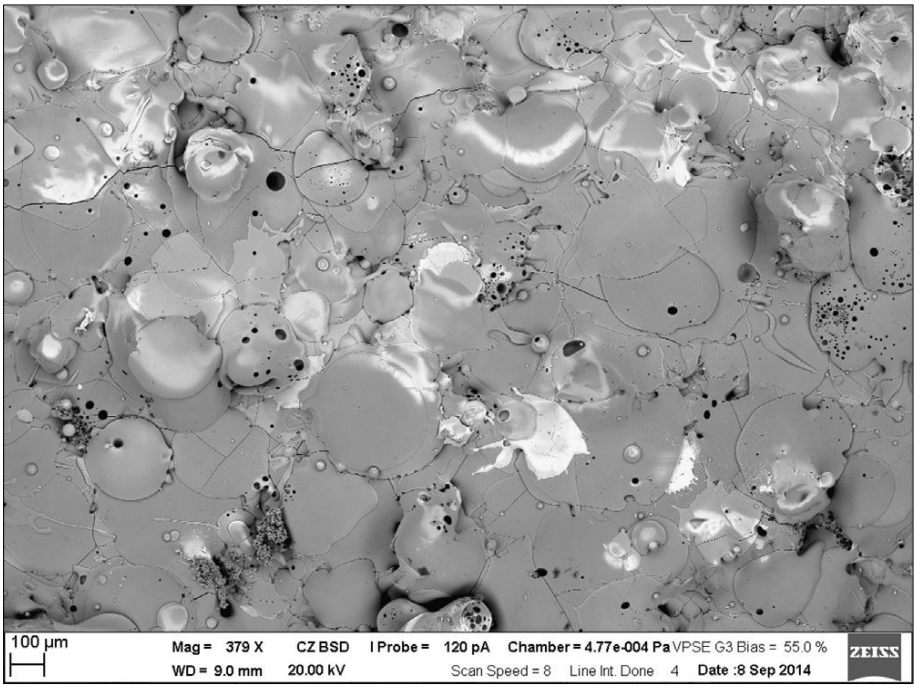

Figure 9. Surface of the diopside self-supporting plate (SEM-SE)

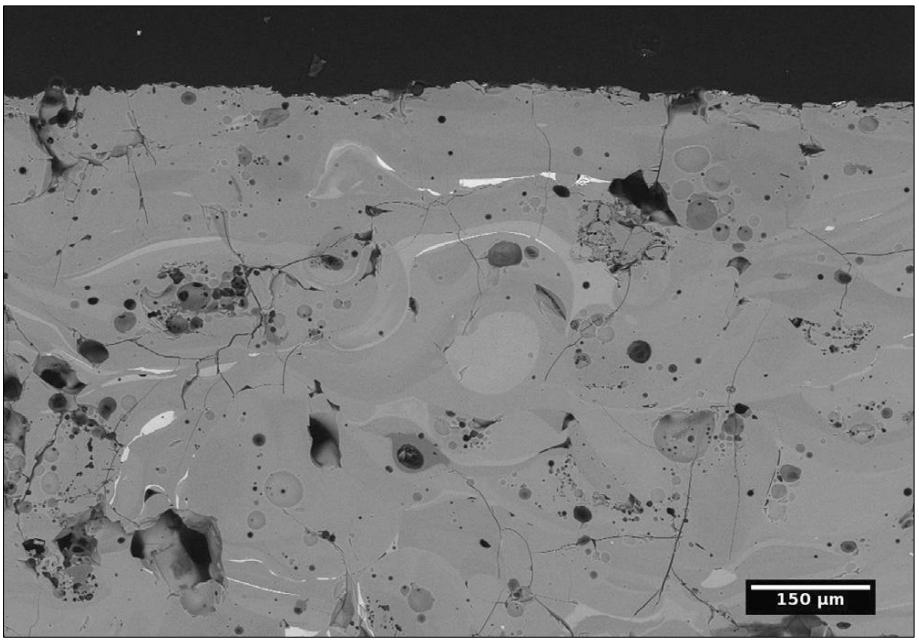

Figure 10. Cross section of diopside self-supporting plate (SEM-BSE)

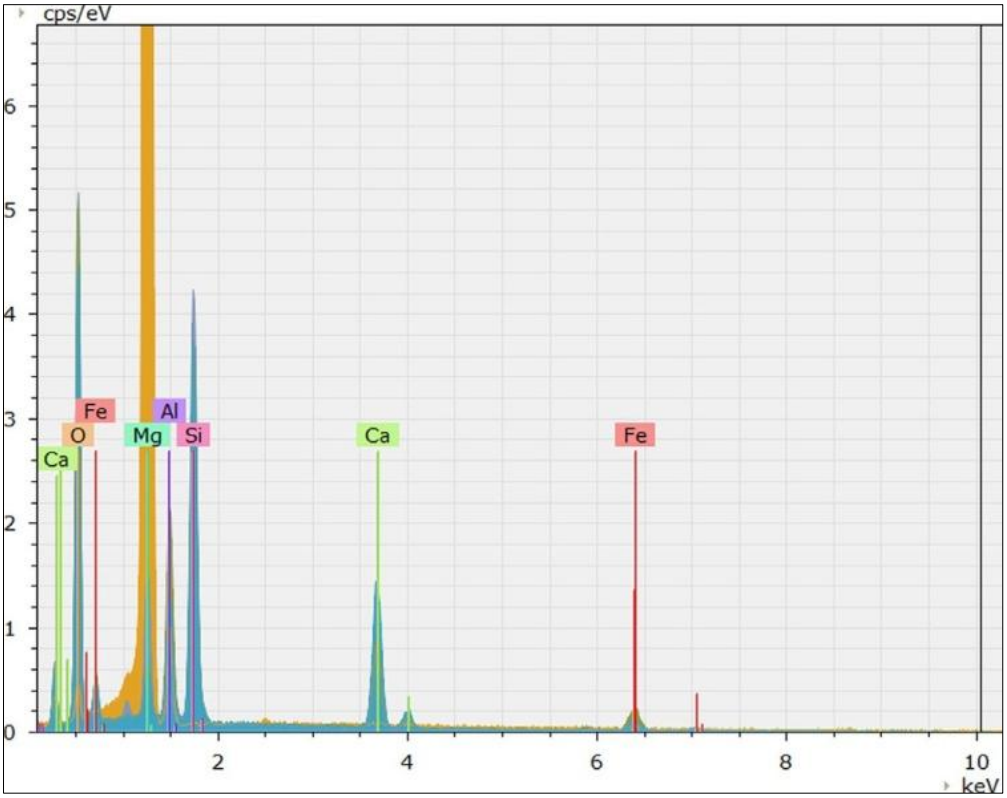

Figure 11. Diopside coating EDX spectrum

Mechanical properties characteristics can be seen in table 5. Specific weight and main porosity characteristics of the samples are shown in table 6.

Table 5. Mechanical characteristics of the as-sprayed diopside [95]

Sample	**Microhardness [GPa]**	**Inverse wear rate [m/mm^3]**	**Surface roughness R_a [µm]**
WSP - FSP	8.72 ± 1.24	35.6 ± 0.6	49.8 ± 5.6
WSP on Mg	6.40 ± 0.57	-	34.3 ± 11.0

Table 6. Porosity and specific weight of the as-sprayed diopside ([a] Image analysis, [b] Pycnometry, [c] Immersion) [75; 95]

Porosity [%][a]	8.2 ± 2.3
ED (pore size) [µm][a]	10.4 ± 0.9
Number of pores over 20µm per mm^2[a]	523 ± 79
Specific weight [g/cm^3][b]	2.9041 ± 0.0009
Specific weight [g/cm^3][c]	2.6671
Open porosity [%][c]	3.225

After annealing, microhardness increased, most probably due to crystallization. Specific weight was lower than for diopside mineral which is between 3.22 and 3.40 g/cm^3. Mean pore size measured by image analysis represents closed and open pores. The wear rate values are comparable with other sprayed silicates such as basalt (IWR 38 to 42 m/mm^3 for various SD) or garnet (IWR about 45 m/mm^3), or common dielectric ceramics $BaTiO_3$ (IWR about 37 m/mm^3) [96]. After annealing, porosity increased nearly twice (table 7) [75]. Thermally induced coagulation of pores probably occurred, similarly to titanate coatings [96].

Table 7. Immersion determined open porosity of diopside coatings

Sample	Porosity [%]
WSP–FSP	3.225
Annealed 15min	7.743
Annealed 30h	7.367

XRD patterns of feedstock powder, an as-sprayed sample and samples annealed at 900 °C for 15 min and 30 h are shown in figure 12. In comparison with the original feedstock powder, which was fully crystalline, the material after spraying is predominantly amorphous (halo between 20° and 40° 2theta) only with traces of crystalline phases. Diopside in two different forms can be found in the feedstock powder, i.e. a standard one with composition $CaMgSi_2O_6$ and a ferroan form [97]. Subsequent Rietveld analysis revealed that both diopsides form together around 80 wt% of the feedstock while the rest is mostly clinoenstatite and cristobalite. Diopside phase re-emerges in the annealed samples, as seen in figure 12. Broader profiles, as compared to the feedstock, indicate substantially smaller grain size (or, more relevantly said, coherently scattering domain sizes). The Rietveld refinement showed only minor grain coarsening from around 40 nm after 15 min annealing to 60 nm after 30 h annealing [75]. The result of Rietveld refinement for the sample annealed for 30 h is presented in figure 13.

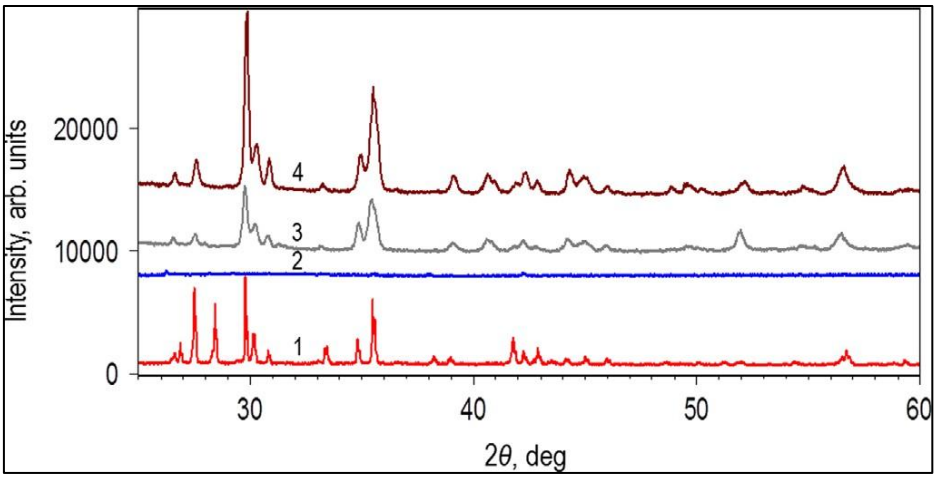

Figure 12. XRD patterns of diopside feedstock powder (1), as-sprayed sample (2) and samples after 15 min (3) and 30 h (4) annealing at 900 °C (vertical shift was introduced in order to distinguish between the patterns)

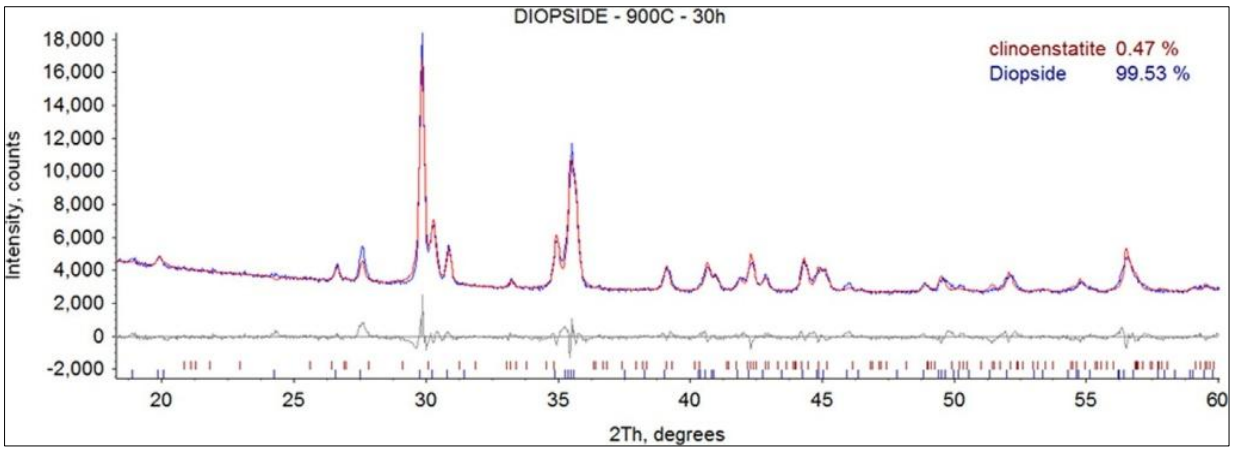

Figure 13. Rietveld refinement of powder XRD pattern measured on a diopside sample annealed for 30 h at 900 °C; the measured data are in blue and the fit is in red, difference between both ("R_{wp} quality of the fit") is presented as a gray curve at zero intensity

Chemical analysis obtained by EDX (table 8) shows certain amount of impurities in the as-sprayed sample; especially atoms of Al and Fe are present due to the natural character of the diopside powder. Chemical composition varies among the individual splats, especially the amount of Si changes significantly [95], as can be seen from the line scan across several splats, which is presented in figure 14 (the placement of the measured line is drawn over the microstructure).

Table 8. Chemical elements content in the as-sprayed diopside (determined by EDX)

Element [%]	O	Si	Ca	Mg	Fe	Al	SUMMA
Formula	60	20	10	10	-	-	100
WSP - FSP	60.0	17.6	11.0	5.3	3.35	2.35	99.6

Differential thermal analysis data are presented in figure 15. The feedstock powder did not undergo any specific transformation up to 1100 °C, whereas the as-sprayed material transformed between 830 °C and 850 °C, which was manifested by an exothermic peak. According to the literature [98] this transformation corresponded to the crystallization of diopside, however, it took place at a slightly lower temperature because the diopside material is of lower purity [99].

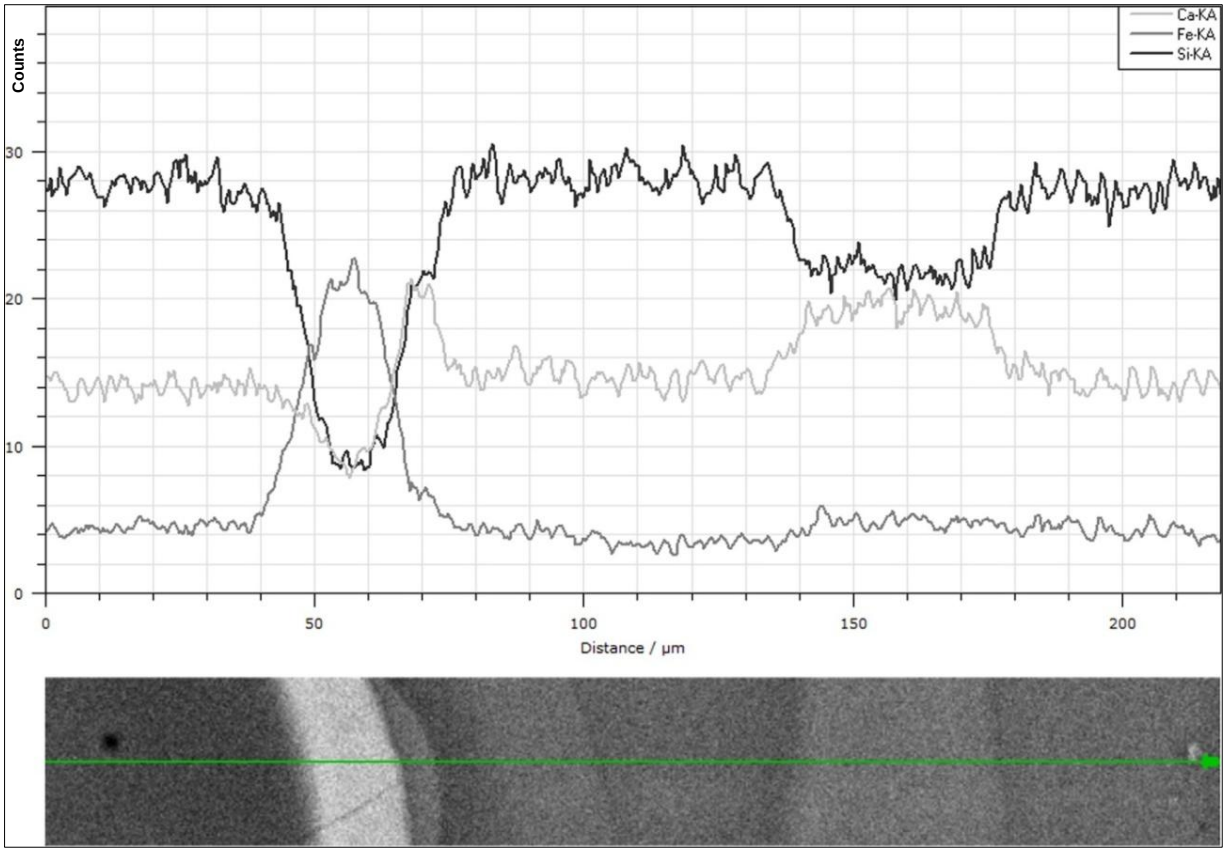

Figure 14. Line EDX scan showing variations in chemical composition among single splats of diopside coating

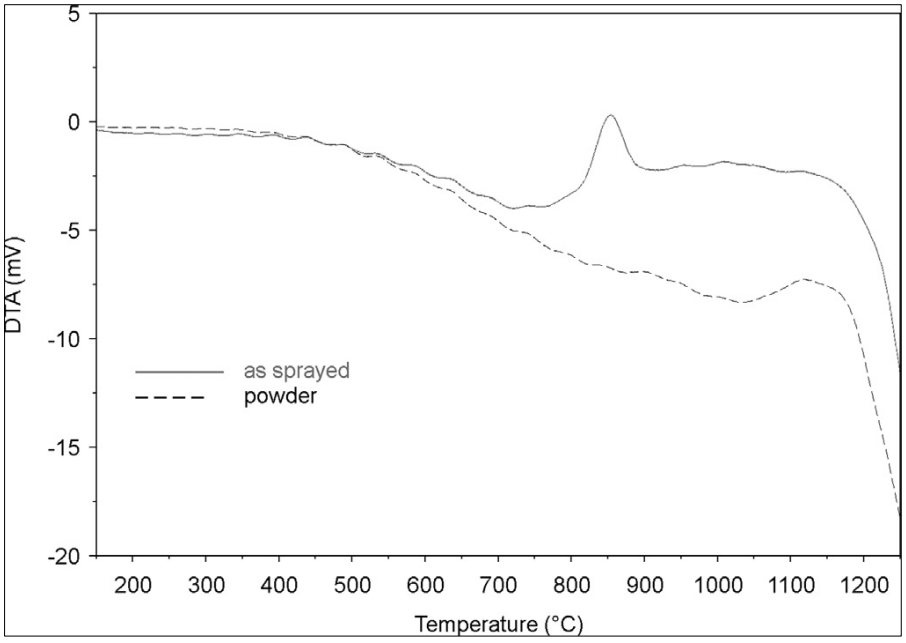

Figure 15. DTA curve of the diopside feedstock powder and as-sprayed FSP

Crystallization was performed also by thermal post-treatment of the FSP samples. Presumably, after crystallization, diffusion leading to further microstructure rearrangement by sintering and defects healing was partly blocked by elements such as Fe and Al, and the microstructure remained significantly heterogeneous [75]. The grain size is larger (according to XRD) in case of longer annealing.

Conclusions for Diopside

Plasma sprayed diopside represents an inexpensive natural material that can be processed by the plasma spray technique to form self-supporting plates stripped from steel substrates. The study demonstrated this ability for water-stabilized plasma spray system. And after all, a production of diopside coatings in plasma spray technology in general was manifested for the first time. The observed mechanical properties of plasma sprayed diopside are also comparable with other silicates. The microstructure modification by annealing, i.e. crystallization into a fine-grained structure, appeared to be not favourable in case of diopside; probably due to the two-fold phase appearance of diopside as well as due to the presence of Fe and Al impurities [75].

5.3 Tourmaline

Figure 16 presents single splats sprayed from four different spray distances at a fixed feeding distance of 40 mm. For the shortest spray distance of 300 mm the splats were fragmented, which indicates impact at too high a temperature and at an unacceptably high velocity. When the SD was set to 400 mm or 450 mm, the splats frequently bounced off (the central part of the splat is absent or damaged) because of low impact temperature and velocity. At a medium SD of 350 mm the splats were surrounded by long 'fingers', but only in this case was the central part completely solid. This indicated that the most suitable conditions for coating build-up are at SD 350 mm.

However, the characteristics of single splats are not the only consideration for process optimization, because the cooling regime is not easily transferable to a different substrate material. Also free-flight particles were observed.

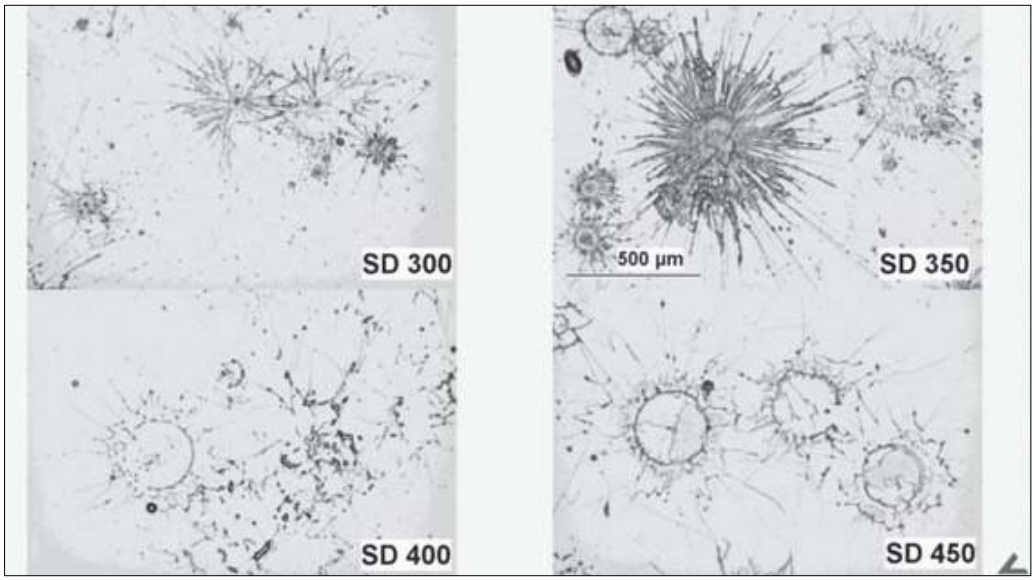

Figure 16. Tourmaline splats on glass with constant feeding distance 40 mm (optical micrograph)

Figure 17 shows the appearance of FFP from two markedly different FDs. At the short FD (40 mm) the particles were well spheroidized, which signifies proper melting. At the long FD (80 mm) a larger amount of less well spheroidized particles was present. The incongruent melting was responsible for the dramatic difference among various particles collected at FD 40 mm (figure 18). Many of them were foam-like with internal porosity. The mixture of wholly molten and partly molten particles, several of which were foam-like, is a suitable basis for production of porous, ultralow weight coatings.

For coating production, FD varied between 40 mm and 100 mm and the SD varied between 250 mm and 350 mm. A combination of FD 100 mm and SD 250 mm was used as well, not based on the previously described optimization, but in order to minimize the trajectory length where the hot powder is surrounded by reactive air.

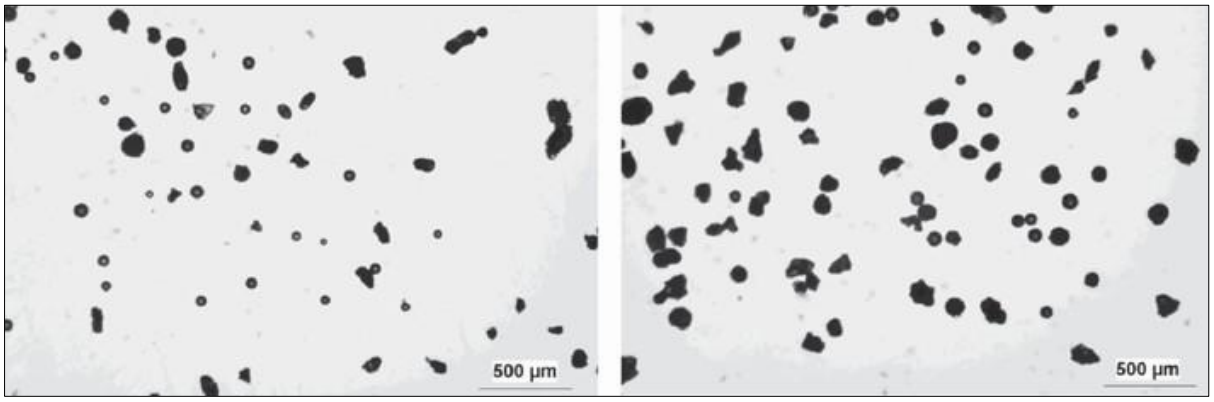

Figure 17. Free-flight particles collected at feeding distance 40 mm (left) and 80 mm (right);(optical micrograph)

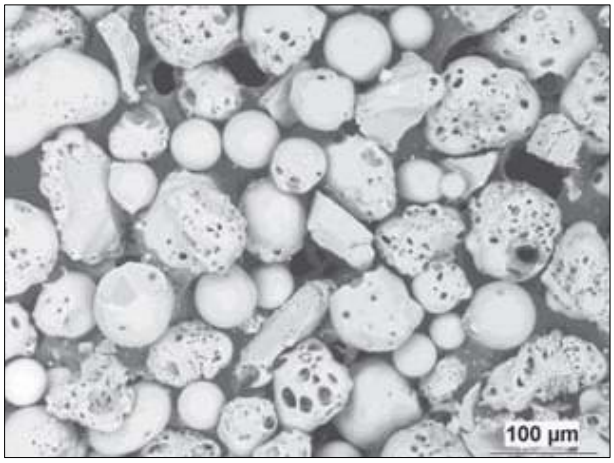

Figure 18. Tourmaline free-flight particles collected at feeding distance 40 mm (optical micrograph)

A representative microstructure of as-sprayed tourmaline cross section is shown in figure 19. A lamellar structure, typical for plasma sprayed coatings, is suppressed by a large number of pores and unmelted or prematurely resolidified particles in the coating. Multiple cracks and predominantly globular pores were also observed.

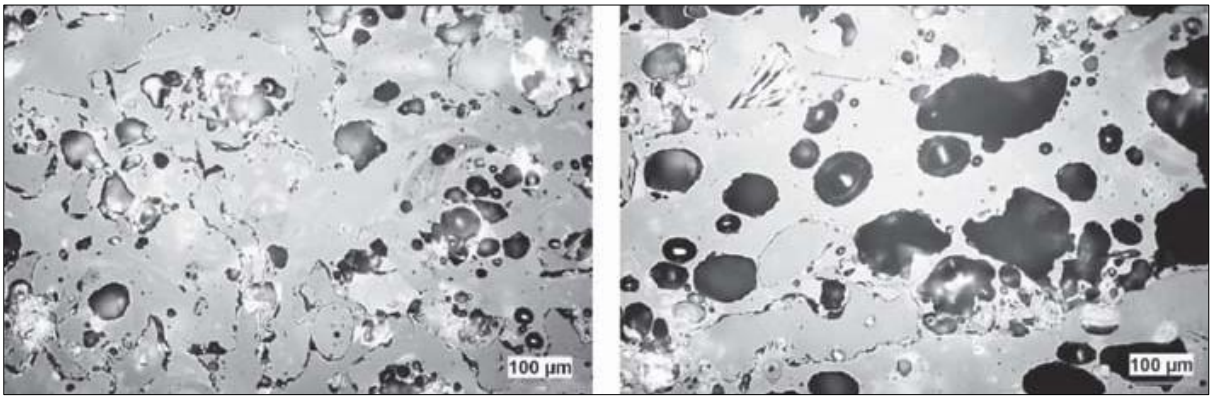

Figure 19. Tourmaline coatings sprayed using FD 40 with SD 350 mm (left) and FD 90 with SD 250 mm (right) (optical micrograph)

The porosity (table 9) as measured by IA was lower for FD40/SD350 coating and extremely high for FD90/SD250 coating. The equivalent diameter (ED) of pores for the second coating was about 15 times smaller than the maximum. The number of pores per square millimeter was only 670, whereas for other coatings from natural mineral feedstock it was typically much higher. This means that tourmaline pores are large and, compared to olivines [11], not very frequent.

The specific weight determined by Archimedes' principle was higher for the FD40/SD350 coating and lower for the FD90/SD250 coating. The specific weight is always markedly lower than for tourmaline mineral. The wear resistance for the 'low porosity' coating FD40/SD350 was much lower than for other sprayed silicates such as basalt or garnet [28] (table 9).

Table 9. Characteristic of selected tourmaline coatings with comparison to other plasma sprayed silicates [83]

Sample	**Porosity (IA) [%]**	**ED (pore size) [µm]**	**Number of pores per mm^2**	**Specific weight [g/cm^3]**	**Inverse wear rate [m/mm^3]**
Tourmaline FD40/SD350	16 ± 3	8.7 ± 0.6	1145	1.67	14.7
Tourmaline FD90/SD250	44 ± 8	10.5 ± 1.0	670	1.18	-
Olivine	*14*	*7.3*	*990–1170*	-	*63*
Garnet	-	-	-	-	*45*
Basalt	-	-	-	-	*38–42*

The phases present were quantified by Rietveld analysis of the XRD patterns of the feedstock powder. The powder was composed of 97.2 % tourmaline, 1.3 % rutile (TiO_2), and 1.5 % phlogopite – a brown mica with chemical formula $KMg_3(Si_3Al)O_{10}(OH,F)_2$. As opposed to the feedstock powder, which was fully crystalline, the material after spraying was partly amorphous (a halo located between 18 ° and 38 ° 2θ in the XRD pattern) with the crystalline phase content varying depending on the FD/SD combination (figure 20). The crystalline part of the material exhibited one phase only – tourmaline.

In general, the longer FD and the shorter SD, the greater the degree of crystallinity. This verified that the combination of long FD and short SD used to minimize the trajectory length where the dwell time in a molten state is minimized was an efficient way of obtaining a predominantly crystalline coating.

The surface roughness parameter R_a is displayed in figure 23. The values between 20 µm and 40 µm are comparable with e.g. WSP sprayed TiO_2 [75] or Ce:YAG [100], and slightly lower than diopside (chapter 5.2). For low SD the roughness increases with higher FD. A combination of FD 100 with SD 250 yielded the highest roughness. This is an indication of slowly impacting particles. Crystallinity of the sample FD100/SD250 was the highest, therefore the slow impact led to longer cooling and to crystallization at non-overcooling conditions.

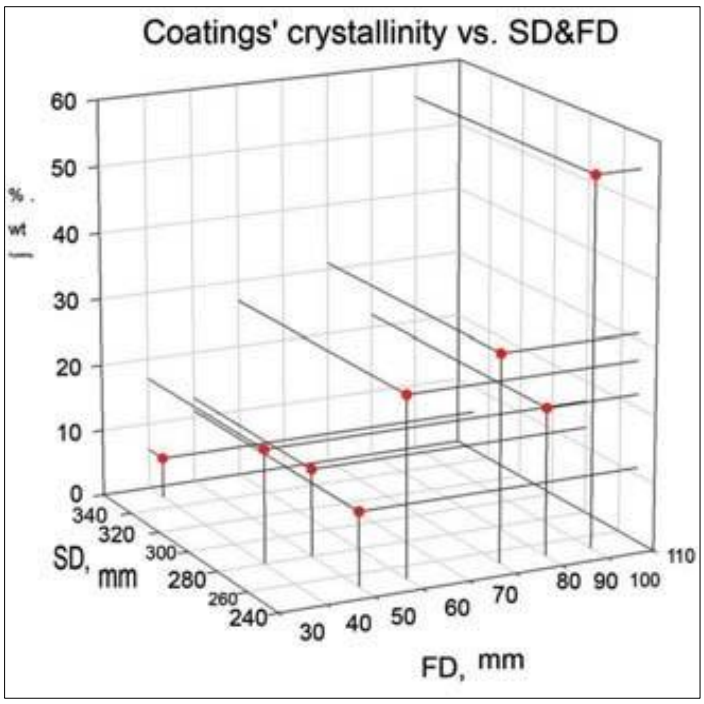

Figure 20. Crystallinity of tourmaline coatings with varying FD and SD

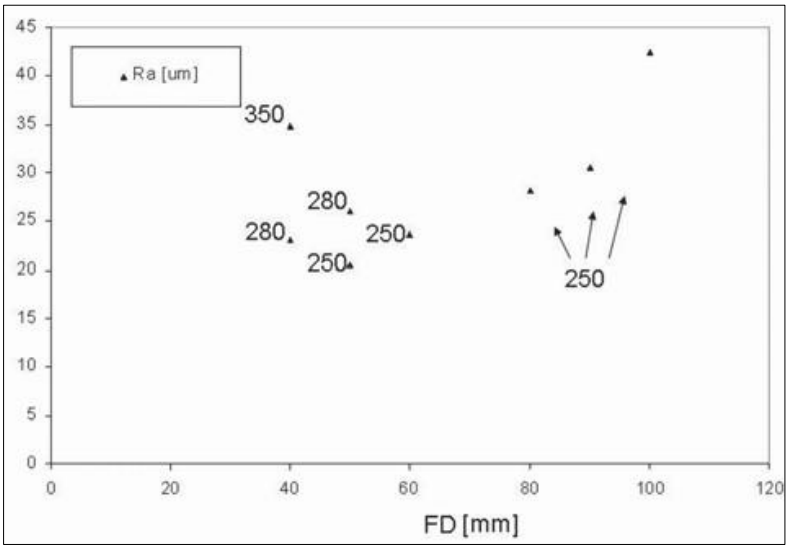

Figure 21. Surface roughness of plasma sprayed tourmaline (corresponding SD [mm] indicated at each point)

Chemical resistance was tested by immersing a piece of plasma-sprayed FSP (sample FD60/SD250) in nitric acid. A commercial 65 % solution of HNO_3 in water was used and the duration of the test was 100 hours. The low specific weight of the sprayed tourmaline (less than 1.5 g/cm^3) resulted in its floating on the acid surface. However, after 18 hours it started to sink and at the end of the test it was lying on the base of the flask. This indicates certain chemical changes, most probably leaching.

The initial crystallinity of this sample, about 27 % (figure 20), decreased after leaching to 14.5 %. However, the diffraction pattern corresponded strictly to tourmaline. Also, the amorphous fraction of the material was preferentially leached, which led to an increase in specific weight since the crystalline material was commonly heavier.

XRD phase analysis of the sample annealed for 8 hours revealed the presence of boromullite ($Al_9BSi_2O_{19}$) and haematite (Fe_2O_3). During annealing, Na, F, and OH groups were released from the original tourmaline ($NaFe_3Al_6(BO_3)_3Si_6O_{18}(OH,F)_4$) phase. Incorporation of boron into the mullite-like phase was reported by Henderson [62]. The other elements were incorporated in new phases. The transformation temperature of the original tourmaline powder was revealed by an endothermic peak on the DTA curve with onset at 890 °C (figure 22), which is in good agreement with values in the literature [62]: 880 ± 10 °C.

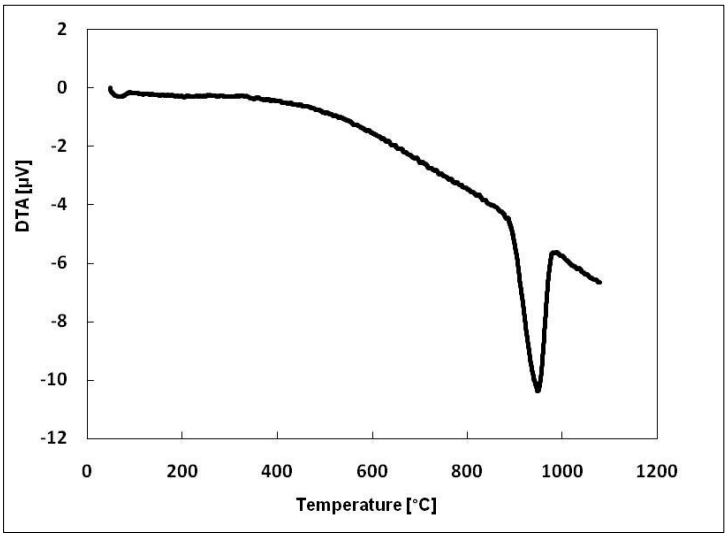

Figure 22. DTA curve of tourmaline feedstock powder

Reflectance results are displayed in figure 23. Surfaces of the as-sprayed and annealed (30 minutes) FD40/SD350 and FD100/SD250 coatings were compared in a wavelength range 250 nm to 2000 nm. Local maxima at about 1450 nm and 1950 nm were attributed to adsorbed water (ambient moisture) and were present in all materials. The flat region between 830 nm and 1000 nm is an instrumental artefact. The FD40/SD350 coating had a reflectance about 10 % (of that of the $BaSO_4$ standard) through most of the observed wavelength range. After annealing, the reflectance partly increased in the range below 1450 nm. In this range it was similar to the as-sprayed FD100/SD250 coating. The F100/SD250 coating was markedly changed by annealing. In the whole visible band and mainly in the infrared band, the reflectance increased markedly to about 30 %. This corresponds with its reddish colour (figure 24), which is caused by haematite.

After short-term annealing, the microstructure was almost unchanged (figure 25). After 30 minutes the coating on a ceramic tile (left) was still porous and the extremely large pores tended to cluster together. After 8 hours the FSP tended to show pore clustering and reorientation into lines parallel with the former substrate. This sample would very likely delaminate when exposed to long-term heating.

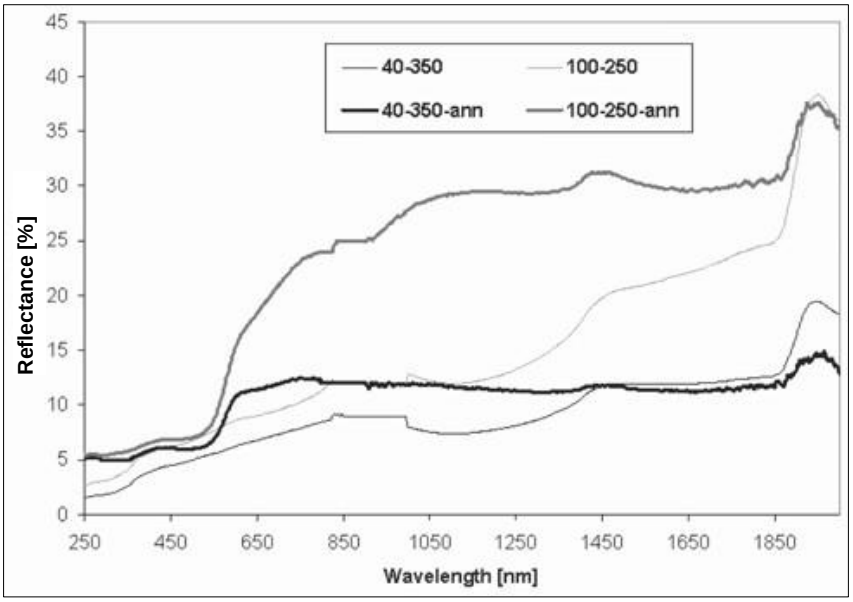

Figure 23. Reflectance of tourmaline coatings with varying FD and SD

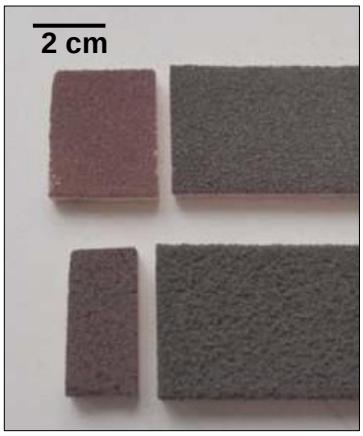

Figure 24. Colour changes of tourmaline coatings – annealed are left; top: FD100/SD250, bottom: FD40/SD350

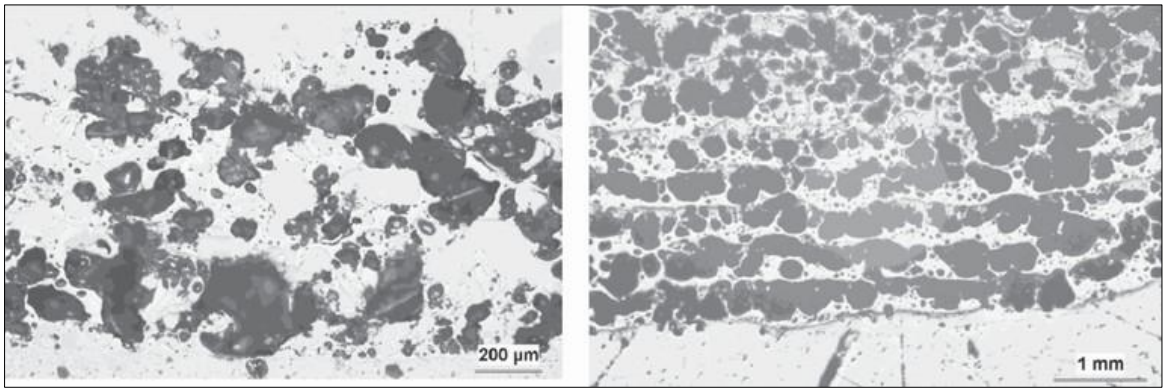

Figure 25. Tourmaline coating after 1000 °C/30 min annealing (left) and a FSP after 1000 °C/8 h annealing (right) (optical micrograph on cross section)

The microhardness increased markedly with annealing (table 10). This is due to the formation of new phases, namely boromullite. A hardness value for boromullite could not be found, but mullite has Vickers microhardness up to 15 GPa [101].

Table 10. Microhardness characteristics of tourmaline plasma sprayed coatings

Sample	**Microhardness [GPa]**
FD40/SD350	8.7 ± 1.4
FD90/SD250	9.3 ± 0.9
Annealed 30 min, FD90/SD250	12.7 ± 1.2
Annealed 8 h, FD90/SD250	13.5 ± 1.6

Conclusions for Tourmaline

Tourmaline is an inexpensive natural material that can be successfully processed by the plasma spray technique to form self-supporting plates stripped from steel substrates or coatings on metallic and ceramic substrates. This study demonstrated this ability using a hybrid water-argon stabilized plasma spray system. Despite the disordered structural character (phase composition containing chemically bonded water, incongruent melting, as well as microstructural homogeneity), plasma-deposited tourmaline exhibited relatively good chemical resistance in nitric acid (65 % HNO_3 in water). The porosity of the deposits was very high and the material was partly amorphous after spraying, with the crystallinity being dependent on a combination of feeding and spraying distances. The observed mechanical properties of the as-sprayed tourmaline are rather poor due to its high porosity. Therefore, tourmaline is not fully comparable with other silicates. In particular, the wear resistance of tourmaline was low. Microstructural modification by annealing, i.e. crystallization into phases without OH groups, appeared to be not favourable in terms of defect healing, probably due to the incongruent melting caused also by other impurities. However, the microhardness increased markedly because of the formation of new harder phases [76].

5.4 Kaolin

The X-ray diffraction data of starting kaolin powder showed fully crystalline material composed of kaolinite 75 %, muscovite 19 %, and silica (quartz) 6 %.

According to DTA dehydroxylation of the feedstock material (labelled KP) was finished at about 650 °C, thus the calcination temperature was set to 700 °C. After thermal treatment, a loss of 10.3 % of the original mass was detected after the treatment, which is caused by dehydration and dehydroxylation. The mass loss of metakaolinite compared to kaolinite was estimated in the literature [102] to be 9 % (surface adsorbed water plus hydroxyl groups). Phase analysis done by XRD showed 97 % of amorphous material (i.e. metakaolinite). The relative content of phases was 38 % silica and 62 % muscovite, whereas the quantity of the components is counted from the 3 % of crystalline material. Metakaolinite originated partly from the transformed kaolinite and partly from silica and muscovite.

Figure 26 displays the size distribution curves of KP and MK powders. Because of structural aspects mentioned below, the curves are rather different. They show a certain degree of sintering of metakaolinite (labelled MK), which was reflected in a higher average size of powder particles – i.e. peak centred at 20 μm instead of 4 μm. Volume density of the smallest particles (the "tail" at about 1 μm) decreased in terms of volume density for metakaolinite.

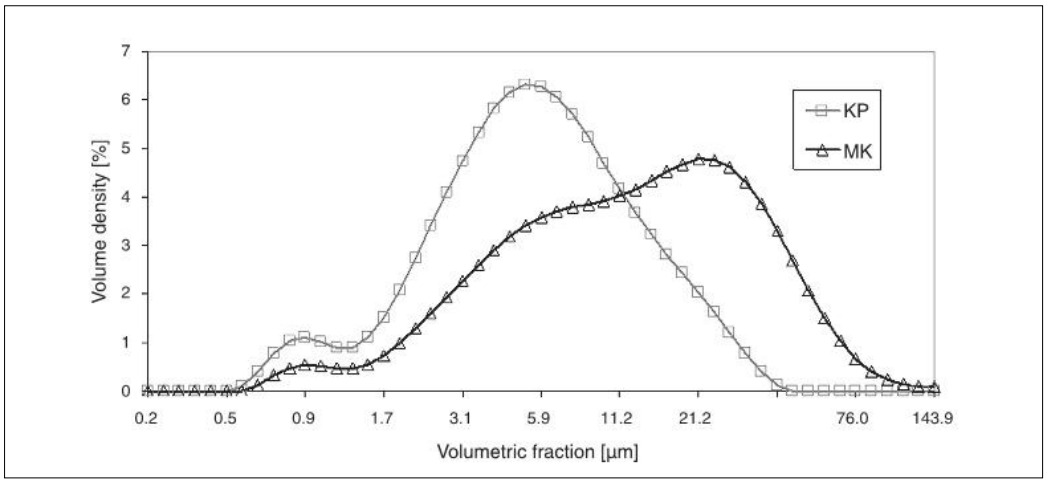

Figure 26. Size distribution of the kaolinite (KP) and metakaolinite (MK) powders

Figure 27 shows the original powder morphology. Especially the KP feedstock contained micro-flakes that formed larger agglomerated particles, but during handling the powder, the micro-flakes were partly separated from each other, which is an unwanted phenomenon and makes the powder too fragile and transport-sensitive (with a difficulty to establish a reliable size fraction).

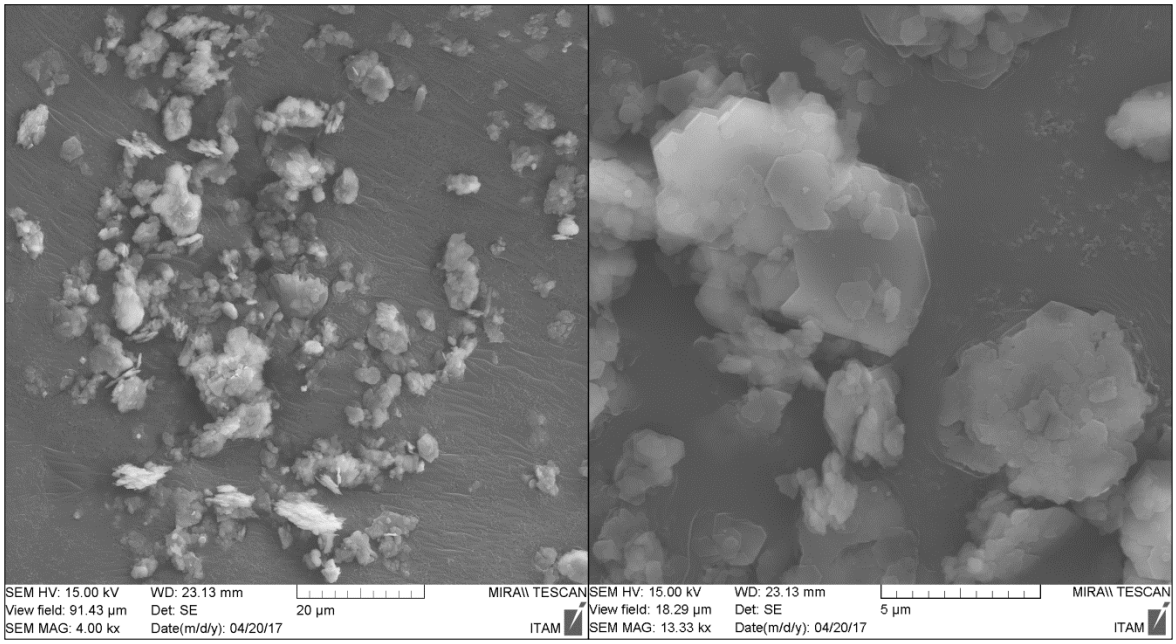

Figure 27. SE micrographs of the kaolinite spray powder

Metakaolinite powder, figure 28, exhibited improved cohesion due to thermal treatment applied – the micro-flakes were partly fused together and formed granulated feedstock powder suitable for plasma spraying.

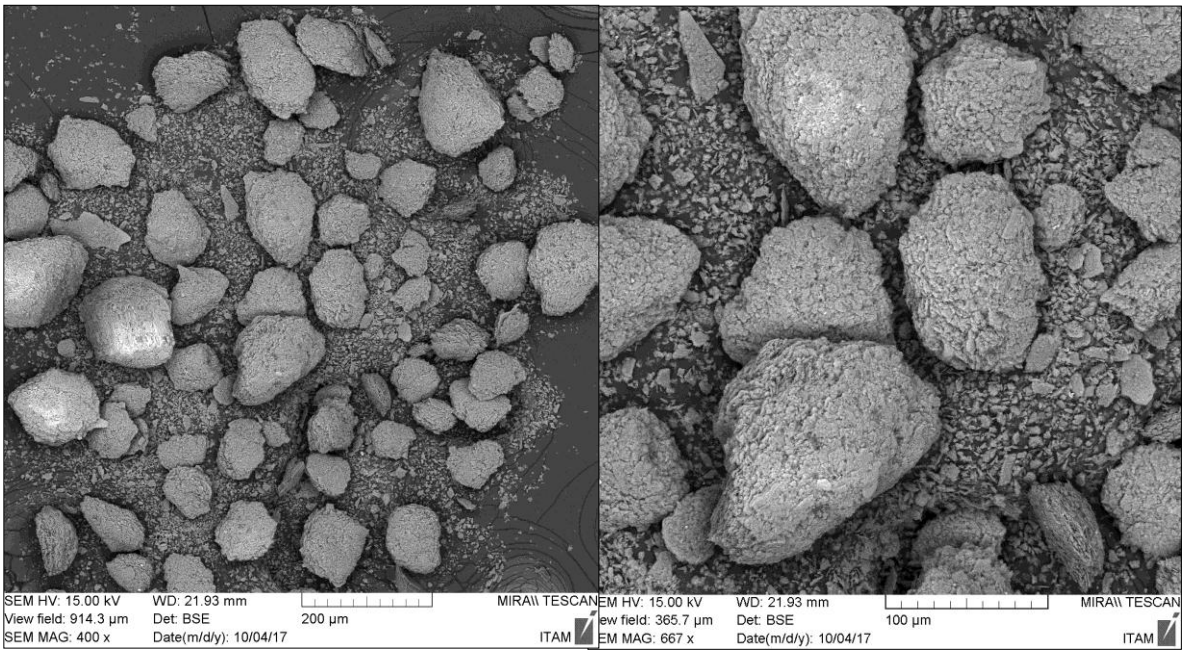

Figure 28. BSE micrographs of the metakaolinite spray powder

Enthalpy of kaolinite tends to increase with temperature [103]. Removal of the bonded water consumes lot of plasma energy, proper melting is rather complicated, and therefore searching for the parameters for optimal spraying was relatively difficult. Incongruent melting was reported at presence of free SiO_2 in kaolinite [104]. Shorter feeding distance led to evaporation of the sprayed material resulting in nearly zero spray efficiency monitored by the thickness growth speed. Longer FD caused extremely porous coating with poor cohesion due to insufficient powder melting. Shorter spray distance induced delamination of the coating (delamination within the coating, not a release from the substrate). Longer SD led to too cold impact and very low thickness growth speed (i.e. poor spraying effectiveness).

Figure 29 shows a coating cross section and figure 30 the surface for KP and MK coatings. Both coatings exhibited significant clustering of pores. Besides that, they exhibited imperfections on inter-splat boundaries and also cracks (MK more pronounced cracks than KP). In comparison with the conventionally sprayed dense "bulk-like" coatings, the microstructure of both actual coatings was adequate for gaining much lower thermal conduction. The "tail" in the particle size distribution at about 1 μm volumetric fraction, c.f. figure 25 and 27, was due to the fine particles at attached to the splat surfaces of both KP and MK, figures 29 and 30.

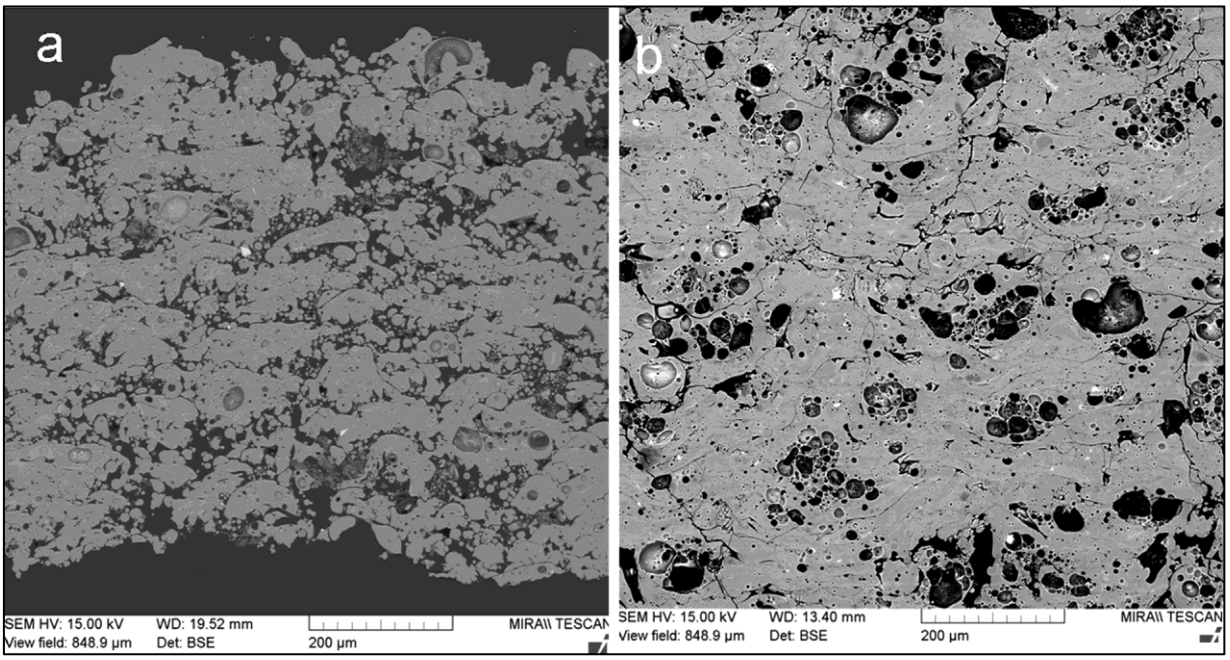

Figure 29. Cross section micrographs of KP sprayed coating(a) and MK sprayed coating (b)

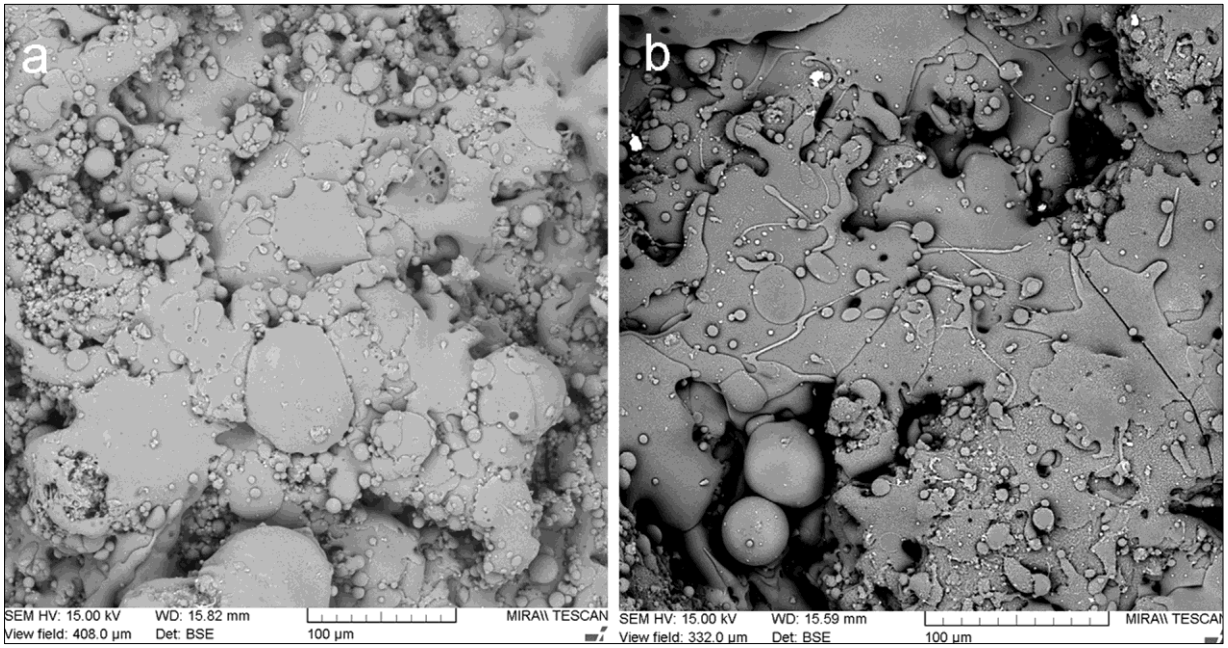

Figure 30. Surface micrographs of KP sprayed coating (a) and MK sprayed coating (b)

Based on the XRF results, table 11, it could be considered that the chemical composition of both coating types nearly identical.

Table 11. XRF elemental analysis on kaolin coating surfaces (other components of CMAS: Ca 3–6 wt.%; Na 1–4 wt.%; Mg 1–2 wt.%) [105]

Element	Content [wt.%] in KP	Content [wt.%] in MK	Content [wt.%] in CMAS
Al	38.4	38.2	8–14
Si	51.6	52.2	69–77
Ti	3.6	2.8	0–1
K	3.1	2.9	2–5
Fe	2.3	2.5	4–7

Specific weight of the deposited KP coating was low (2.499 ± 0.017 g/cm^3 by pycnometry, table 12, and from this standpoint, kaolin belongs to the most lightweight materials ever plasma sprayed, like spodumene (1.64 – 1.88 g/cm^3, porosity 18.5 %) or tourmaline (1.67 g/cm^3, porosity 30.8 %) [76]. Open porosity of the KP coating, examined by the Archimedean technique, was 24.12 % while open porosity of MK coating was only 8.70 % (table 12). Most typical ceramic coatings have much higher specific weight, between 4 and 6 g/cm^3.

Table 12. Porosimetry ([a] He pycnometry, [b]Immersion) and microhardness of the as-sprayed kaolin

Sample	Specific weight [g/cm^3]	Surf. roughness R_a [μm]	Microhardness [GPa]
KP	2.499[a]; 1.851[b]	19.5 ± 1.1	9.45 ± 2.65
MK	1.941[b]	26.0 ± 2.1	11.44 ± 3.10

Porosity based on the image analysis results is summarized in table 13. KP is much more porous compared to MK, whereas the size of pores is similar for KP and MK. The number of pores per square millimeter is 50 % higher for KP. Circularity of pores is very slightly higher for KP. Summary of this quantification is that both coatings exhibit pores with approximately the same character, but KP in a markedly higher quantity. Porosity 7.8 % was measured by image analysis on a mullite coating sprayed with equipment very similar to the actual experiments [106]. Porosity between 6 and 9 % was reported (based on IA) on mullite coating sprayed by plasma with gas stabilization [107]. Porosity of a mullite coating formed from andalusite feedstock was about 6 % [42]. Also, the actual KP coating exhibited extraordinarily high porosity whereas MK is in frame expected for similar sprayed materials.

Table 13. Image analysis results of plasma sprayed KP and MK coatings

Coating	Porosity [%]	ED (pore size) [μm]	Number of pores over 3 μm per mm^2	Circularity
KP	23.8 ± 2.3	10.0 ± 0.5	961 ± 165	0.537 ± 0.026
MK	9.5 ± 1.3	10.2 ± 1.2	603 ± 76	0.480 ± 0.027

Surface roughness of the KP coating was R_a = 19.5 ± 1.1 μm, MK: R_a = 26.0 ± 2.1 μm. This parameter was reported in literature for plasma sprayed mullite $Al_6Si_2O_{13}$ with the value of 14 μm [108], but mullite is typically more compact powder and therefore forms a smoother coating surface.

Microhardness on a KP polished cross section was HVm = 9.45 ± 2.65 GPa at a 0.5 N load, whereas the MK coating was harder (11.44 ± 3.10 GPa). The reported Vickers hardness varied from 1 to 4 GPa at a 10 N load depending of the sintering temperature [109], elsewhere reported as 2 – 7 GPa depending on the sintering temperature (load not reported) [105]. Microhardness of flame sprayed mullite was reported to be about 7 GPa [[110]. Microhardness between 6 and 7 GPa was reported for a mullite coating sprayed by plasma with gas stabilization [111]. Preheating of substrates to 700 °C was applied to increase the microhardness from 7.1 GPa (non-preheated) to 13.0 GPa [107]. Microhardness of mullite coating formed from andalusite Al_2SiO_5 feedstock was about 6.5 GPa [42] (table 12).

Differential thermal analysis results are depicted in figure 31. Endothermic peak on the curve of the starting KP powder with onset at 400 °C signalizes dehydroxylation of kaolinite and formation of metakaolinite, which ends at 650 °C, in concordance with other publications [112; 113]. Hence, the temperature ensuring calcination of the starting powder was set as high as 700 °C at the powder thermal treatment before spraying (that led to

formation of MK powder from the starting KP powder). Crystallization of mullite occurred before 1000 °C in the case of powders as well as coatings. Other authors specified this range to be 980 – 992 °C [112]. A spinel type aluminosilicate (SAS) formation at about 980 °C was mentioned in another work [15], or in the case of plasma sprayed deposit at 961 ± 4 °C [114]. A wide exothermic peak in the temperature range 1200 – 1300 °C corresponds to the mullite formation from SAS [102]. In the KP coating, this peak was missing and thus this fact correlates to the absence of mullite detected by XRD, which agrees also with another paper dealing with plasma spraying of kaolinite flakes [114]. In case of KP powder, the heating was stopped at about 1050 °C to extract samples for XRD and resolve if the conversion to mullite is direct or indirect with intermediate SAS phase. The analysis of the pattern showed 28 % of crystalline material and from this proportion, 16 % was SAS (the rest: mullite 41 %, quartz 27 % and muscovite 15 %). According to the character of CTE curves, KP coating exhibited this intermediate transformation as well, whereas MK not. Only a part of the material followed this "two-step" transformation, whereas high majority transformed directly.

TG curves are presented in figure 32. KP powder lost weight markedly because of the dehydroxylation of kaolinite and formation of metakaolinite, which ends at 650 °C. Above 650 °C, the weight is constant. The weight of KP coating drops firstly because of continual loss of water (probably adsorbed water), and above 500 °C, it is nearly constant.

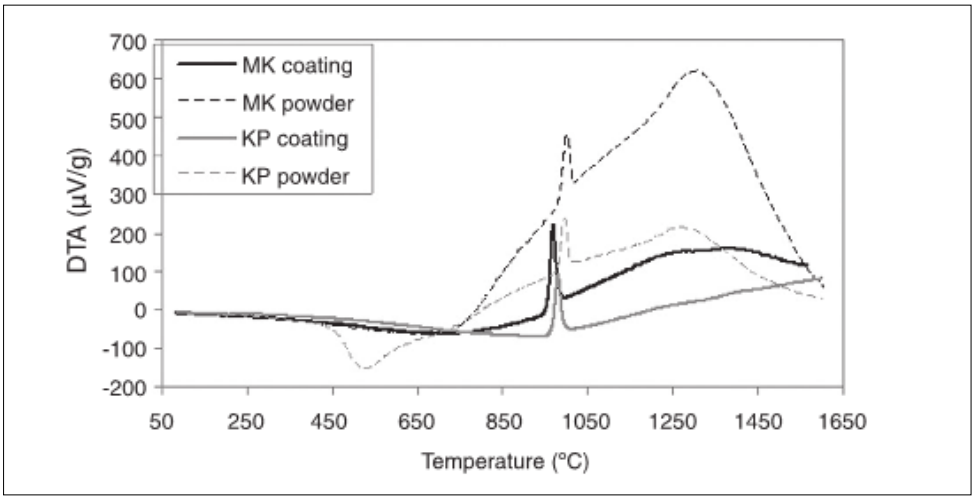

Figure 31. DTA curve of kaolin materials

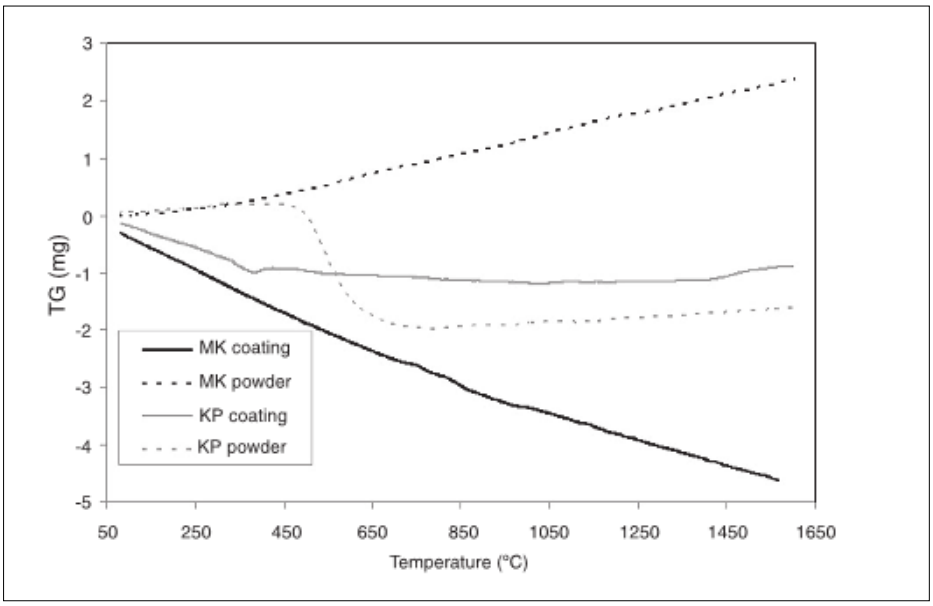

Figure 32. Thermogravimetric curves of kaolin materials

Curves of thermal expansion are displayed in figure 33. The values of the linear coefficient of thermal expansion (CTE) were calculated for the interval from 30 to 850 °C and this parameter has a value of 0.6 × 10−6/K for the KP coating and 1.5 × 10−6/K for the MK coating, respectively. Plasma sprayed mullite had typically higher thermal expansion at elevated temperatures, 3.8 × 10−6/K [113]. Values at RT (i.e. 9.4 × 10−6/K for KP and 9.3 × 10−6/K for MK, respectively) were higher than typical values of oxide ceramics and are much closer to metallic materials often serving as substrates, as for example stainless steel with CTE 15.5 × 10−6/K. The constituent materials had following CTE: alumina 8.3–9.0, silica 9.0–14.0 and mullite 4.5–5.7 (all ×10−6/K). Reasonably, the values of KP and MK were in between, MK slightly higher, because it contained slightly more silica. The inset in figure 33 showed a peak on the displacement curve at about 600 °C. In concordance with [115; 116], this phenomenon corresponded to α-quartz to β-quartz inversion and was more pronounced in MK, richer in SiO_2 than KP.

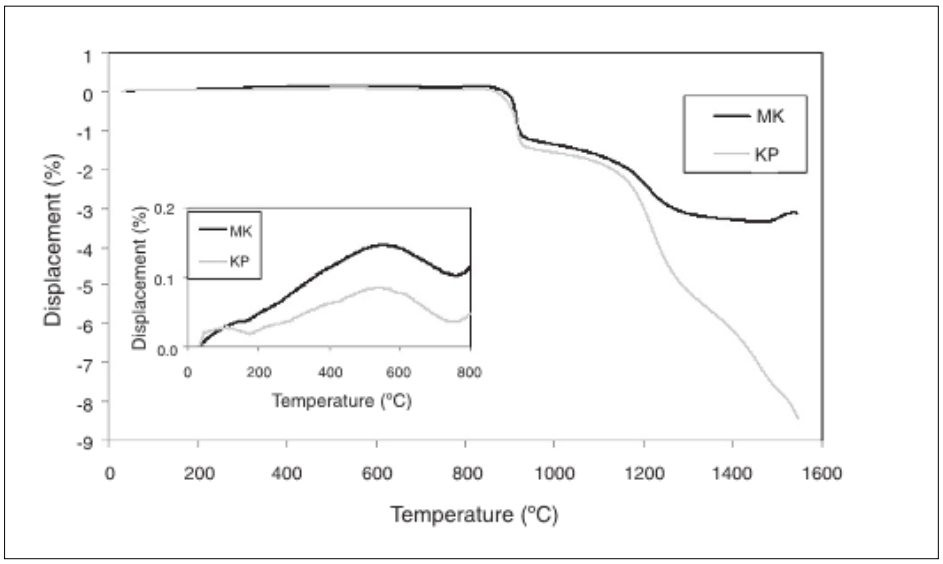

Figure 33. Thermal expansion curves of kaolin materials

During sintering, the CTE above sintering temperature, about 850 °C, was also negative [117] (i.e. the material shortened). So, it can be summarized that CTEs of the coatings were high at RT and decreased at high temperatures.

Thermal diffusivity of plasma sprayed KP and MK coatings is listed in table 14. Near 800 °C, various ceramics change the thermal diffusivity behaviour from a drop to a rise with the growing temperature [118; 119; 120]. Behaviour of both types of the coatings was similar, table 14. Kaolinite had lower values of diffusivity than metakaolinite because of presence of more pores and less pronounced sintering. The values of thermal diffusivity as well as their evolution with temperature were very similar to the coating sprayed from natural $ZrSiO_4$ (unpublished results).

Table 14. Thermal diffusivity [cm^2/s] of plasma sprayed KP and MK coatings

Temperature [°C]	KP	MK
25	0.00251	0.00344
700	0.00227	0.00318
900	0.00256	0.00348

Phase Composition and Reactivity with CMAS

Reactivity of the coating with calcium-magnesium-aluminum silicate (CMAS) powder was tested. The resulting phase components are summarized together with all other phase composition investigations in table 15. "Annealed coating" means the same thermal procedure (4 h at 1150 °C) but without CMAS.

Fully crystalline kaolinite (KP) powder was nearly completely amorphized by the plasma spray process. Metakaolinite (MK) powder is considered amorphous, because the metakaolinite mineral does not exhibit diffracting peaks [108; 121; 122]. Chemically, more simple phases as alumina, mullite and SiO_2 appeared after spraying instead of muscovite, which is a hydrated phase. Elements like K and F are, expectably, absent in coatings because of their volatility.

Surface of the coating obtained a brown "glaze" after annealing with CMAS. The phase present in both coatings annealed with CMAS, $(Ca_{0.64}Na_{0.32})(Al_{1.775}Si_{2.275})O_8$, is mineralogically called labradorite – a feldspathic mineral originated from albite, diopside and $CaCO_3$. This means that. CaO remained, while CO_2 was vaporized from CMAS in reactions with Al and Si from the as-sprayed coating. Both coatings annealed with CMAS became richer in silica compared to the annealed coatings. In conclusion, CMAS has detrimental effect on the KP coating, because labradorite is a less thermally stable phase compared to mullite constituting the crystalline fraction of the as-sprayed coatings.

Kaolinite dehydroxylation occurs through a three-dimensional diffusion process with formation of an amorphous product identified as metakaolinite ($Al_2Si_2O_5$). This process is completed above 650 °C. Metakaolinite remains short-range ordered at least to 980 °C. Formation of mullite at 995 – 998 °C, i.e. primary mullite, side by side with a cubic phase, Si-Al spinel (SAS), and amorphous silica-rich component at around 983 °C was confirmed, namely for both powders. From 1136 °C growth of mullite crystals occurs, and at T > 1200 °C crystallization of high temperature cristobalite (SiO_2) from a Si-rich amorphous

phase takes place. Additionally, in the Si-rich amorphous component formed at kaolinite-muscovite interfaces. Secondary mullite crystallization occurs at 1300 °C [112]. At a higher heating rate (over 1 K/min), delamination (destruction of kaolinite sheet structure) prevails over the dehydroxylation [123], and this is the case of plasma spraying, but also the case of thermal re-forming of KP into MK.

Table 15. XRD phases of kaolin material, semiquantitative content (% of total), [% of crystalline only]([a]CMAS composition is based on literature [124]*)*

CMAS powder[a]	**KP powder**	**MK powder**
SiO_2 (50)	$Al_2Si_2O_5(OH)_4$ kaolinite (75.0)	Amorph. (97)
$Na(AlSi_3O_8)$ albite (32)	$KAl_2(AlSi_3O_{10})(F,OH)_2$muscovite (19.0)	$KAl_2(AlSi_3O_{10})(F,OH)_2$ muscovite [62.0] (1.8)
$CaMg(Si_2O_6)$ diopside (16)	SiO_2 (6.0)	SiO_2 [38.0] (1.2)
$CaCO_3$ (2)	–	–
KP coating	**KP coating annealed**	**KP coating annealed with CMAS**
Amorph. (97)	Amorph. (38)	Amorph. (47)
Gamma Al_2O_3 [85.5] (2.4)	$Al_6Si_2O_{13}$ mullite [97.0](60)	$Al_6Si_2O_{13}$ mullite [51.0] (27)
SiO_2 [15.5] (0.6)	SiO_2 [3.0] (2)	SiO_2 [28.0] (15)
		$(Ca_{0.64}Na_{0.32})$ $(Al_{1.775}Si_{2.275})O_8$ labradorite [21.0] (11)
MK coating	**MK coating annealed**	**MK coating ann. with CMAS**
Amorph. (95)	Amorph. (39)	Amorph. (42)
SiO_2 [42.0] (2.3)	$Al_6Si_2O_{13}$ mullite [97.5] (60)	$Al_6Si_2O_{13}$ mullite [42.5] (25)
$Al_6Si_2O_{13}$ mullite [30.0] (1.5)	SiO_2 [2.5] (2)	(Ca0.64Na0.32) $(Al_{1.775}Si_{2.275})O_8$ labradorite [31.0] (18)
Gamma Al_2O_3 [28.0] (1.2)	–	SiO_2 [25.5] (15)

Conclusions for Kaoline

Kaolinite with structurally bonded water and metakaolinite without it were successfully plasma sprayed. Metakaolinite powder was obtained by thermal treatment of natural raw kaolinite. The coatings were rather porous, mainly the kaolinite-based ones, and composed predominantly of amorphous material. Metakaolinite coating was less porous and harder. Muscovite phase, found in the powder, disappeared after spraying, while new phases were present – alumina in the kaolinite coating and moreover mullite in the metakaolinite coating. Annealing for 4 h at 1150 °C increased the proportion of crystalline material and increased the mullite content. After interaction with Si-rich CMAS dust, labradorite appeared but mullite and silica remained the most important components [77].

5.5 Clay Shale

Selected chemical, physical and mineralogical data (table 16) about A111VHR were taken from the supplier material data sheet for the delivered powder fraction of 0 - 100 μm and from results of our control measurements for the sifted fraction A111 of 40 - 80 μm.

Table 16. Data for A111 powder
(''Suppliers data'' taken from the certificate for the delivered fraction 0 - 100 μm - A111VHR; ''IPP data'' are for the additionally sieved fraction of 40 - 80 μm and its mineralogical composition is normalized for the over-all crystallinity of 66.1 %)

Chemical analysis	**Supplier's data[wt.%]**	**IPP data [wt.%]**	**Physical properties**	**Supplier's data**	**IPP data**
Al_2O_3	42.15	42.1	Specific weight (g/cm^3)	2.57	2.74
Fe_2O_3	1.25	2.1	Calcination temperature (°C)	1350	-
TiO_2	1.54	3.6	Mineralogical composition (wt.%)		
K_2O	0.75	1.3	Mullite	38	54.5
Na_2O	0.05	-	Cristobalite	5	8.5
CaO	0.13	-	Quartz	3	1.7
MgO	0.18	-	Rutile TiO_2	-	0.9
SiO_2	53.9	50.9	Anatas TiO_2	-	0.5
-	-	-	Amorphous	54	33.9

There are clear differences between the ''as-delivered'' A111VHR powder (wider fraction) and the used feedstock powder with narrow grain size fraction of 40 - 80 μm (table 16). Meaningful differences were found in the mineralogical compositions, less important in the chemical compositions. In figure 34, diffraction patterns for the undersize fraction (below 40 μm - black) and the selected one (red) are juxtaposed. Phase ID revealed presence of mullite, quartz, cristobalite and two tetragonal modifications of titanium oxide, i.e. anatase and rutile, the corresponding weight percentages of these phases in both fractions were ascertained by quantitative Rietveld method and are seen in table 17. The presence of amorphous part, demonstrated by the so-called amorphous halo in diffraction patterns, was approximated by the pseudo Voigt function. The crystallinity was computed presuming the chemical composition of the crystalline and amorphous material is the same. Average sizes of coherently scattering domains (''crystallite size'') were calculated according to direct convolution approach from integral breadths of observed diffraction profiles (table 18). Results show that the overall crystallinity of the selected feedstock size is higher due to slightly more mullite and cristobalite compared to the undersized fraction (table 17). Moreover, the specific weight of the feedstock is higher. That result seems to suggest that the differences are due to disparity in the size of the analyzed powder: the amorphous phase in original powder is brittle and fragments on milling into very fine particles below 40 μm which are separated off by the following sieving. It is therefore important to note that milling and sieving the initial raw A111VHR material can influence the mineralogical composition of the feedstock powder.

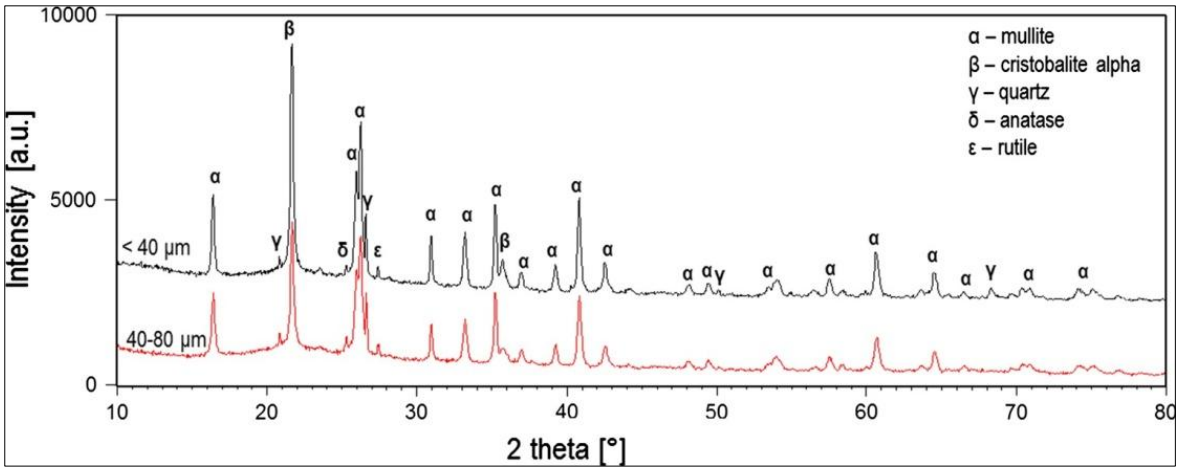

Figure 34. Diffraction patterns of two different fractions of A111: narrow fraction of 40 to 80 µm (red pattern) and fraction below 40 µm (black pattern)

Table 17. Summary of phase composition of selected samples (820 °C, 1200 °C, 1400 °C and 500 °C for deposits annealed for 30 min)

Phase[wt.%]/sample	Powder under 40 µm	Feedstock 40-80 µm	As-sprayed deposits	820 ºC	1200 ºC	1400 ºC	1500 ºC
Crystallinity	61	66	9	7	59	57	57
Mullite	51	54	9	7	57	55	55
Cristobalite	6	8	0	0	2	2	2
Quartz	~2	~2	0	0	0	0	0
Rutile	<1	<1	0	0	0	0	0
Anatas	<1	<1	0	0	0	0	0
Amorphous	39	34	91	93	41	43	43

Table 18. Sizes of the coherent crystallites in selected samples (1200 °C and 1400 °C for deposits annealed for 30 min)

Crystallite size, nm/sample	Powder under 40 µm	Feedstock 40-80 µm	1200 ºC	1400 ºC
Mullite	32 ± 1	39 ± 1	41 ± 1	73 ± 2
Cristobalite	28 ± 1	32 ± 1	37 ± 2	40 ± 3
Quartz	195 ± 31	192 ± 31	-	-
Rutile	62 ± 11	53 ± 10	-	-
Anatas	99 ± 27	52 ± 7	-	-

In order to find out the optimal processing parameters, spraying was done for various combinations of feeding and spraying distances and corresponding particle temperatures, velocities, and diameters were collected by DPV-2000 (figure 35). Diameters of flying particle have not differed much from that of the original feedstock and hence only data of

particles velocities and temperatures are shown. Since it was expected that A111 feedstock particles would decompose after interaction with hot plasma into mullite and SiO_2 [41; 108], the optimal processing temperature was chosen above the melting point of mullite (1840 °C) to allow for good flattening after impacting the substrate and below the boiling point of SiO_2 (2230 °C) to avoid its selective evaporation. The following single set of processing parameters (labelled P1) was then used for all further spraying: FD = 40 mm and SD = 400 mm, giving the flying ‘‘particle’’ temperature around 2100 °C and its velocity close to 100 m/s.

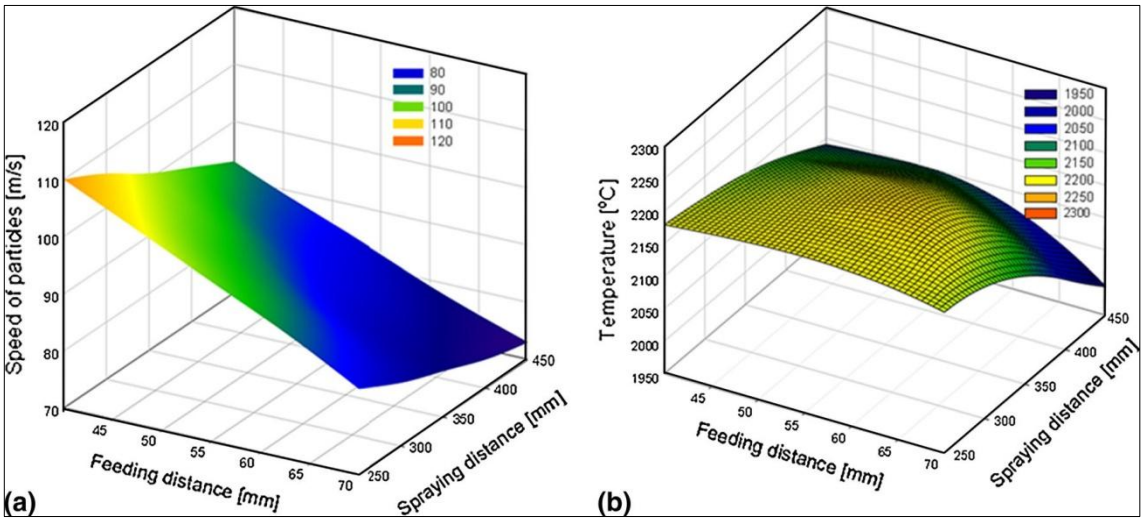

Figure 35. In-flight particle data in dependency on processing parameters FD and SD; velocity (a) and temperature (b)

Figure 36 shows a characteristic structure of A111 deposit sprayed with the P1 parameters. It is worth noting that (i) there is no visible adhesion failure between the coating and substrate; (ii) there is no visible splat architecture of coatings; (iii) there are a large number of ‘‘bubble like’’ pores in the structure, and (iv) there are visible cracks which tend to form in the direction parallel to the substrate surface, but no typical small cracks perpendicular to the substrate are seen. The impacting A111 ‘‘particles’’ are in reality fully liquid droplets which on impact fill very well the rough surface of blasted steel coupons, and, still in persisting liquid form, they smelt together before cooling without forming visible ‘‘splat boundaries.’’ That confirms previous results [41] showing that the deposits exhibit less pronounced splat structure than is commonly observed in alumina or zirconia ceramics. The ‘‘bubble like’’ pores may originate from frozen gas bubbles filled either with evaporated silica or with air entrapped in the feedstock powder. Presence of these bubbles sets the porosity to around 12 vol.%, which is significantly more that it is usually found in silica-based amorphous matrix. Cracks parallel to the surface may result from the stress relaxation, when several sprayed layers are subsequently deposited on each other. A new ‘‘liquid’’ layer is deposited on already solidified previous layer and during cooling a perfect cohesion between subsequent layers will not develop.

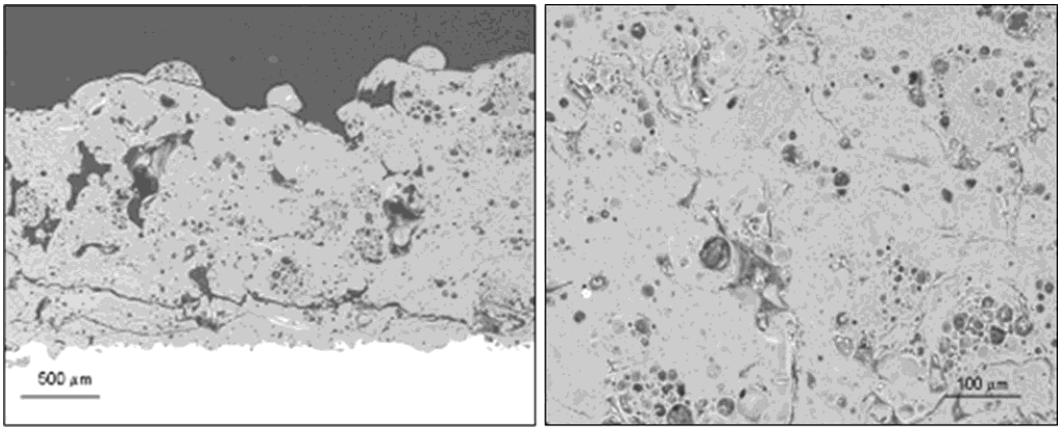

Figure 36. Structure on cross sections of A111 coatings on steel substrate (SEM)

Comparison of the XRD data from the feedstock with that of an as-sprayed coating (figure 37) clearly shows that while the feedstock has crystalline part (66 wt.%), the coating is mostly amorphous. Detailed analysis of the diffraction patterns demonstrates that the only crystalline matter in the as-sprayed A111 deposits is mullite [78] with maximum amount always bellow 10 wt.%. Prevailing content of the amorphous fraction is confirmed also by the specific weight measurement - the average specific weight of the as-sprayed deposits is 2.39 g/cm^3 against the feedstock specific weight of 2.73 g/cm^3.

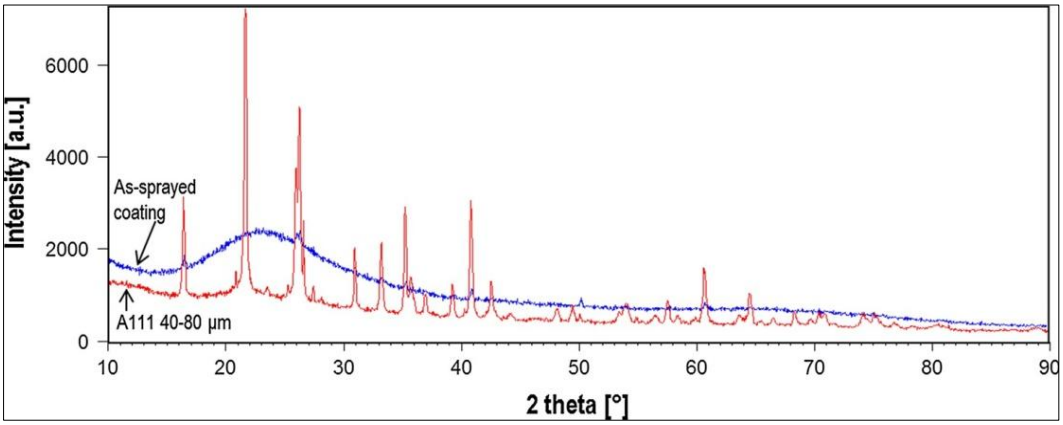

Figure 37. XRD patterns from the feedstock (red) and from as-sprayed coating (blue)

Since similar results were obtained for FSP, it is evident that the difference in preheating temperatures of the substrate and of the mandrel (150 K) does not play any substantial role and therefore general word ‘‘deposit’’ is further used for both types, i.e. for coatings and FSP. Results for the deposits are similar to those for Eucor material [125] suggesting that the cooling rate of droplets after impact was too high for growth of a large amount of a crystalline phase.

The FFP were also analyzed for comparison. It is evident that, in contrary to fast impacting particles, the longer flying time in the air without impacting provides slower cooling and therefore crystallinity of collected particles is higher than of deposits. XRD phase analysis (table 19) revealed that FFP contain around 20 wt.% of mullite with minor amounts of other minerals. The size of coherently scattering domains in FFP is slightly smaller than mullite and cristobalite crystallites in the feedstock.

However, one substantial question remains open, namely whether the mullite content in the as-sprayed deposits (up to 10 %) is just unmelted residuum of feedstock particles which were only softened by the plasma and deposited (or spheroidized), or whether it is mullite formed from the fully molten droplets. Detailed SEM analysis of the structure seems to suggest that there might be both types of mullite present. Yet it is interesting to note that no unmelted (angular) feedstock particles were found. Smaller values of average crystallite size in the annealed deposits (table 19) seems to advocate that there is a mixture of larger mullite crystallites originating from the feedstock and newly formed fine mullite crystallites.

Other interesting point is that no intermediate phase, such as spinel, frequently reported during thermally decomposition of kaolinite [126; 127; 128; 129], was found in coatings. The cooling rate in the deposits was evidently high enough to prevent diffusion and formation of transitional phases.

Table 19. XRD data from Rietveld analysis of FFP and HTXRD samples ("Size" means the average size of the coherently scattering mullite regions - crystallites)

Sample	**Annealing temp. [ºC]**	**Size [nm]**	**Crystallinity [vol.%]**
Feedstock	-	39	66
FFP 1	-	33	23
FFP 2	-	34	19
Annealed	880	19	3
	900	18	4
	920	14	9
	940	11	44
	960	11	46
	980	11	48
	1000	12	50
	1200	34	59
	1400	67	57
	1500	117	57

Rough measurement of the phase stability of A111 deposits was done by the TMA instrument. In such a technique the beginning of a crystallization process in an amorphous material is usually demonstrated as a distinct contraction of the sample due to the volume change accompanying that transition. This will be demonstrated in thermal evolution of crystallization related volume changes (CRVC) as a peak. Figure 38 presents measurements in the temperature interval from 550 to 1300 °C with a constant heating rate 5 K/min. There is a slight decrease in the length with no corresponding changes of CRVC below approximately 900 °C followed by steep changes of both parameters above that temperature. The phases in the mostly amorphous deposit are evidently stable on annealing up to temperatures of 850 - 900 °C. The sharp CRVC peak at 940 - 950 °C (figure 38) suggests rapid crystallization of the amorphous phase.

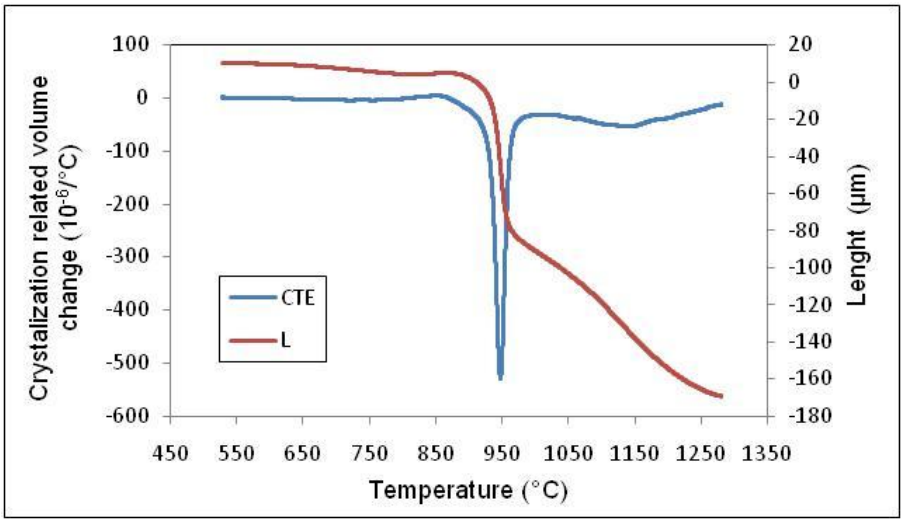

Figure 38. Thermal expansion curves of as-sprayed calcined clay shale

TMA measurements were supplemented by other thermal diagnostic techniques. Thermal conductivity measurement (figure 39) shows a sudden substantial increase between 600 and 800 °C suggesting, similarly to TMA, that certain ‘‘preparatory’’ processes in the amorphous matrix may take place even around 800 °C. Nature of that process is yet unclear but it is probably connected to nucleation.

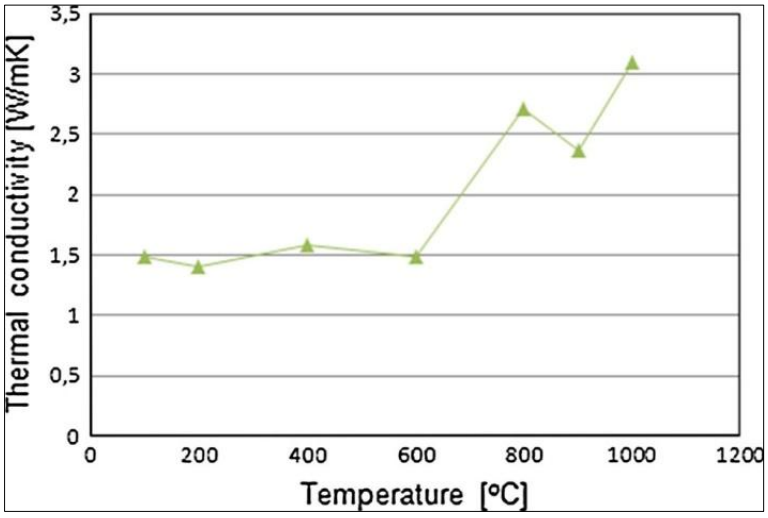

Figure 39. Thermal conductivity data of as-sprayed calcined clay shale

Considering that the nucleation rate is a function of annealing temperature T_a, several authors [130; 131] used dependency of the exothermic peak temperature on T_a during DTA measurement for determining the maximum nucleation rate. Johnson et al. [131] concluded that in quenched and annealed specimens mullite was fully nucleated below 850 °C. Considering result of the thermal conductivity measurement showing significant change in k below 800 °C and the well-established fact that the thermal conductivity of a given material is affected by impurities, structural changes, partial phase transition, etc., it is safe to conclude

that in the as-sprayed mostly amorphous samples nucleation induced by annealing is completed below 900 °C. Measurements of the dependency of heat flow on temperature shows the start of amorphous-to-crystalline transition just above 900 °C and the maximum rate of crystallization around 950 °C [78]. Figure 40 illustrates the effect of the heating rate on the heat flow value that allows calculating the activation energy of the transition. Using the Kissinger method [132] the calculated activation energy was 1012 kJ/mol, which closely corresponds to value for crystallization of the ternary eutectoid mixture of Al_2O_3-SiO_2-ZrO_2 [125]. This value fits also well into the range of values for the mullite crystallization, i.e. 850-1300 kJ/mol, as reported in the literature [131]. In order to confirm that there is no additional crystallization, TMA and DSC measurements were conducted on the same samples for the second time. No substantial differences were registered.

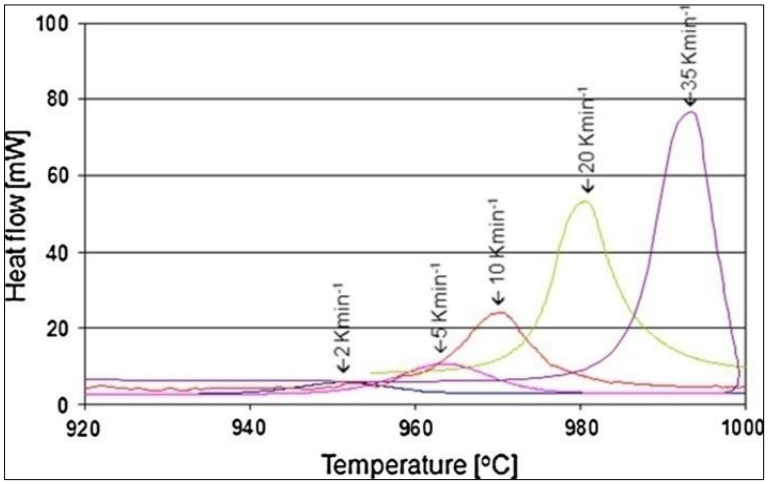

Figure 40. Results of DSC measurements of as-sprayed calcined clay shale

As the second stage the thorough XRD analysis of samples annealed above 800 °C was performed in two steps: (i) on consecutively isothermally annealed deposited strips, (ii) by a direct HTXRD measurement. Results for the selected most important intervals of temperature are on figure 41. Regardless of the fact that for the consecutive isothermal annealing with ensuing XRD measurements longer dwell time for each sample at a given temperature (30 min) was chosen, while at the HTXRD measurements the dwell time data given temperature was substantially shorter (1 min), the results are basically identical. Mullite starts to form between 920 and 940 °C, confirming the non-XRD results, and its amount gradually increases with the temperature

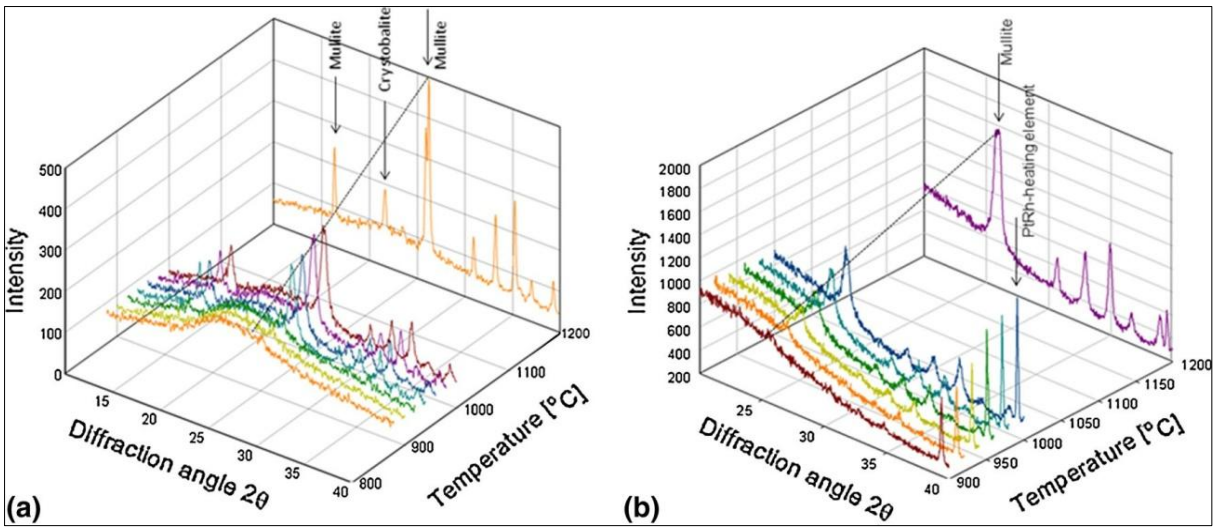

Figure 41. Selected XRD patterns for successive samples (a) and HTXRD (b)

The amount of crystalline fraction reaches its maximum of around 60 wt.% at 1200 °C and does not increase further up to the highest measured temperature of 1500 °C. Besides mullite, a small amount (around 2 wt.%) of cristobalite also forms at temperatures from 1200 °C upward. Example of Rietveld refinement of the sample annealed at 1400 °C is in figure 42. While the crystallite sizes of both mullite as well cristobalite are at 1200 °C similar to those of the feedstock, mullite grains then grow rapidly, reaching roughly twice the initial size as seen in table 18. No other phases besides mullite and cristobalite were detected even for the highest annealing temperature (figure 42). That means the oxides identified in the A111 feedstock (Fe_2O_3, TiO_2, K_2O) are probably dissolved in the amorphous matrix and thus increase its stability [78].

In order to consider whether residual stresses play any role in the stabilization of amorphous content, two samples annealed at 940 and 1400 °C were investigated by XRD. The computed macroscopic residual stresses were tensile amounting to 160 ± 18 MPa and 177 ± 15 MPa, for 940 and 1400 °C samples, respectively. As seen, the stresses barely change with annealing temperature and their tensile character may act as one of the hindrances to the volume reduction of the amorphous fraction.

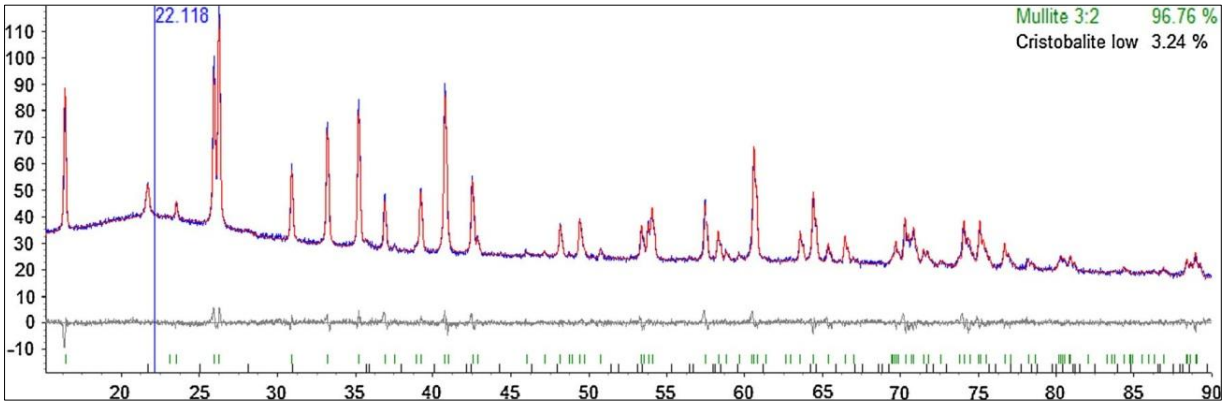

Figure 42. Result of Rietveld refinement of sample annealed at 1400 °C for 30 min

The picture from SEM in figure 43 depicts the main features of the structure after the highest annealing temperature. There are evidently three different morphological formations: (i) clusters of fine needle-like crystallites and neighbouring; (ii) lighter regions amounting by image analysis to around 58 %, which corresponds to XRD results for sum of crystalline mullite and cristobalite. The (iii) darker regions are amorphous with higher content of SiO_2. Similarly, in an alumina-kaolinite sample with an overall composition of mullite after heat treatment at 1300 °C for 1 h, Aksay et al. [133] showed the formation of nanometer-sized mullite crystallites in an amorphous silica-rich matrix.

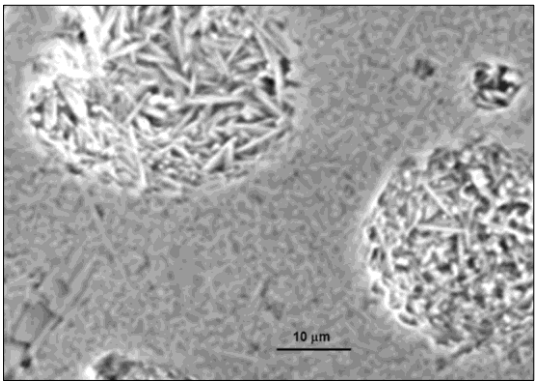

Figure 43. Structure of A111 deposit after annealing at 1500 °C (SEM)

Plasma spraying often produces non-equilibrium and non-stoichiometric structures and this is the case of A111 spraying with processing parameters P1. Resulting deposits consist of minor fraction of crystalline mullite with stoichiometry closer to ‘‘3/2’’ type and major fraction of glassy SiO_2 that is contrary to the feedstock exhibiting much larger crystallinity. Mostly amorphous A111 deposits have porosity about 12 % and they could be, hence, used for EBC when higher resistance against chemical attack or small biological activity is needed. On the other hand, their use is limited to lower temperature regions to avoid any problems from possible crystalline transition (mainly volume changes).

A111 plasma sprayed deposits are stable at least up to 800 °C. Pre-nucleation of crystallites in the amorphous matrix starts between 600 and 800 °C but crystallization (crystal growth) starts at higher temperatures above 800 °C. There is a very rapid crystallization between 920 and 940 °C when the largest increase of the crystallinity was recorded (figure 44). The measured crystallization temperature is about 30 °C lower than that reported in the literature for spraying from the mullite feedstock, for instance [41; 113]. The difference may result from presence of impurities such as Fe_2O_3, TiO_2, and K_2O in the feedstock.

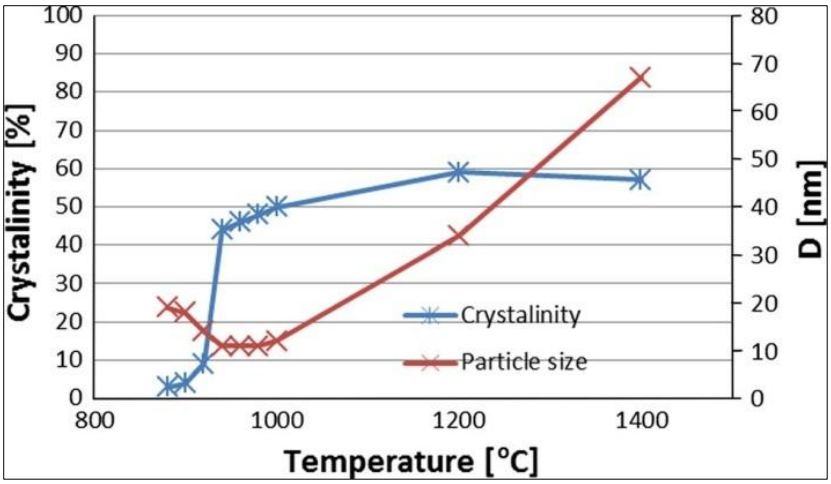

Figure 44. Summary of dependency of crystallinity and crystallite size on annealing temperature calculated from XRD patterns

The maximum crystallinity formed after annealing up to 1500 °C is around 60 wt.% which is close to the crystallinity of the feedstock powder. Clearly, the reason for the limited crystallinity is similar to that published by An et al. [42], i.e. the deficiency of Al_2O_3 needed for the mullite reaction. An et al. solved this problem by additional secondary annealing with addition of extra alumina for reaction with remaining silica. In general, the ‘‘3/2’’ mullite contains about 72 wt.% of alumina in equilibrium, but in non-equilibria intermediate states, which cannot be excluded in our spraying experiments, even more alumina may enter the reaction (up to 83.2 wt.% [134]). A111 feedstock, which is based on kaolinite, contains only around 42 wt.% of Al_2O_3 that is available for formation of mullite, which corresponds to the measured value of approximately 60 wt.% crystallinity [78]. Remaining amorphous SiO_2 is probably stabilized by minor additives in A111 and certain role must be played by the residual stresses, which have according to the performed XRD measurements tensile character, but it remains to be not fully understood. Various authors discuss stabilization of amorphous silica against crystallization, pointing out the uncertainty in temperatures, experimentally found hysteresis, showing the influence of additives and processing parameters, etc., but there is no unified theory available.

Since it is possible to produce mullite nanocrystallites in the silica-rich amorphous matrix, it is evident that the as-sprayed coatings can be transformed into FGM by applying surface heat treatment. Suitable surface heat treatment will raise the surface temperature above 900 °C while maintaining the coating/substrate interface at temperatures below 250 °C [135]. Surface layer of the resulting graded material contains up 60 % of crystalline phases (mullite and cristobalite) similar to the bulk heat-treated samples. With increasing depth below the coating surface, the crystalline content decreases below 10 % which corresponds to crystallinity of the as-sprayed coating. The crystalline surface layer may exhibit improved mechanical properties (e.g. increased hardness) thanks to the presence of nanocrystallites [135]. To prove this assumption further investigations concerning mechanical properties have to be done.

Conclusions for Clay Shale

Inexpensive natural raw material of the silicate family, labelled A111, is highly suitable for plasma spraying. As the raw material has been already calcined by the supplier, there are no intermediate phases appearing in the deposits, which is advantageous. There are only various amounts of mullite, glassy SiO_2 and crystalline SiO_2-cristobalite in the feedstock. As-sprayed coatings are mostly amorphous and temperature stable up to around 800 °C. Higher degree of crystallinity can be generated by a relatively short annealing at temperatures above 900 °C. Degree of crystallinity (up to 60 wt.%) and the crystallite size can be controlled by the annealing temperature. Sizes of crystallites of mullite and cristobalite dispersed in the amorphous matrix after heat treatment are in tens of nanometers. The as-sprayed coatings can be potentially transformed into a functionally graded material by applying surface heat treatment [78].

6 Implication for Science and Practical Applications

The results of this work bring a positive finding that all studied materials can be processed by plasma spraying technology. And at the same time, in some parameters they are fully comparable with synthetic ones used in industry. Above all, it should be noted that two of them stand up to comparison with widely used mullite.

Microhardness of plasma spray (PS) metakolinite and kaolinite is close to the bulk mullite (10 GPa) [81; 77]. Thermal conductivity of PS calcined clay shale is similar to bulk mullite [81]. Thanks to very low thermal diffusivity, even lesser than mullites' diffusivity, both kaolin coatings are advisable as thermal insulators. Thermal expansion (CTE) of kaolin coatings are notably lower than bulk mullite and plasma sprayed synthetic mullite [41; 81; 77], unlike clay shale coatings, which have corresponding CTE to PS synthetic mullite [78; 41]. Otherwise, clay shale and kaolin coatings have a very similar thermal behavior as bulk and plasma sprayed synthetic mullites. This also applies to their temperature stability (up to about 1500 °C, that is the maximum operating temperature of the instruments on which the samples were analyzed). Specific weight of calcined clay shale coatings (2.3 g/cm^3) is slightly lower than specific weight of bulk mullite (2.8 g/cm^3) [81] and that of plasma sprayed synthetic mullite (3.1 g/cm^3) [136]; specific weight of both kaolin coatings is even lower (around 2 g/cm^3). Needle-like crystallites are one of two regular mullite morphologies [137] increasing mechanical strength and thermal shock resistance of mullite materials by interlocking of individual needles - such structures were observed in clay shale coatings.

The production engineers need to know the application limits of the coating materials. The temperature of possible use in long-term application for each of the studied materials is given in table 20. For comparison, other geomaterials from plasma sprayed coatings, studied by the author outside the scope of this work [138], are also presented. Besides other purposes, the electrical applications (insulations, passive components of circuits – e.g. capacitors) of majority of these given geomaterials look prospectively [138].

Table 20. Maximal temperature limiting the durability of as-sprayed coatings

Coating Material	Temperature [°C]
Zircon	730
Diopside	800
Garnet	800
Clay Shale	800
Kaolin	850
Basalt	850
Olivine	890
Tourmaline	890

The thesis is focused on a new trend that relies on future research. The experimental activity at the Institute of Plasma Physics will be continued on the investigation of other properties of the plasma sprayed diopside, zircon, and kaolin coatings and on the recommendation of its potential application into practice. Since many types of natural raw materials are still poorly explored from the point of utilization in plasma coatings applications, future research will be most probably focused on the estimation and

investigation of the most suitable geomaterials. A well-promising mineral is chromite ($FeCr_2O_4$), the ore for chromium, or the mineral barite ($BaSO_4$) used as radiation protection. The interest has also increased in using precious stones such as spinel, epidote, or andalusite (mentioned in chapter 2.2). Other minerals such as kerphalite, wollastonite, Li-Si compounds, phonolite rock, or silicates originating from the mining of lithium-rich ores should also be in the scope of future investigation. One of the biggest challenges definitely represents the discovery of an alternative material to the YSZ coatings.

In addition, waste materials from metallurgy (see chapter 2.2) and other industrial sectors are promising sources for plasma spraying applications as an alternative to the synthetic powders. Fly ash in a mixture with red mud (the mud from aluminum oxide production) was also successfully plasma-sprayed [139]. Mantry et. al. [140] revealed an interesting and innovative utilization of cheap copper slag (the waste from copper metallurgy) sprayed on an aluminous and steel substrate. The improvement consisted in the enhancement of the hardness of the material after deposition of the coating. The subsequent addition of aluminous powder to the slag before spraying improved the coating-substrate adhesion to such extent that the material could be utilized in highly demanded tribological applications as well. Additionally, the slag is also a source of nickel, ferrovanadium, ferronickel, ferrotungsten, and other compounds.

A promising source of forsterite, corundum, and chromium-magnesite ceramics are old furnace linings [8]. Cementitious clinkers or scrapings from furnaces also represent a possible source of material for the spraying powder production. Nevertheless, the modification and purification of such waste materials often require cooperation with other industrial facilities. Alternative materials for plasma coating applications can also be combined with synthetic additives to improve both the properties of the final coating or the process of spraying.

7 Conclusion

The substitution of synthetic materials represents a poorly explored issue, as it has been summarized above in the introduction part. In the scope of the thesis, the investigated materials were zircon, diopside, tourmaline, kaolin, and clay shale. The tasks of the work were fulfilled as follows:

- Compact plasma coatings were successfully prepared from all mentioned materials. Four of them are materials that have not yet been studied and even have not been successfully processed in the field of plasma spraying. Moreover, due to their non-standard properties, kaolin and tourmaline are a topic in the field of thermal spraying that has not yet been studied.
- Among the tested materials, only tourmaline was appraised as rather unsuitable for plasma spraying because of the high porosity of coatings causing by poorer mechanical properties. The coatings on a substrate or free-standing coatings produced from the other tested materials could be utilized for example in moderately demanding high-temperature applications. The coatings manufactured from the zircon and diopside represents a promising alternative to coatings made from synthetic silicates, e.g. steatite.
- The coatings made from kaolin and from clay shale after thermal post-treatment application are well suited as an alternative to mullite material.
- The author of this thesis focused on examination the thermal properties of the materials. She successfully assessed crystallization temperatures of the coatings under the secondary thermal loading, i.e. stability of materials in high-temperature processes (table 20 in chapter 6).
- Zircon mineral was plasma sprayed as coatings on stainless steel or ceramic substrates and/or as free-standing zircon subjects (plates and tubes). Instead of amorphization, this material exhibits in the as-sprayed state a nano-cryststallinity [74] on a limit, under which the most advantageous component – tetragonal ZrO_2 – would be preferred according to the literature [89].

  Diopside mineral was plasma sprayed as coatings on stainless steel or carbon steel substrates and/or as free-standing diopside subjects (plates). Thermal post-treatment cannot be recommended, since it was shown to promote porosity development in the coatings due to crystallization of amorphous as-sprayed material. In the other hand, very fine structure (approaching nanostructure) was revealed in the heat-treated material and can be utilized in the materials sciences, because nanocrystalline diopside is rarely studied [75; 95].

  Tourmaline mineral was plasma sprayed as coatings on stainless steel or ceramic substrates and/or as free-standing tourmaline subjects (plates). The relation between plasma parameters and crystallinity was described. Thermal post-treatment was shown to improve the properties of the coatings due to crystallization of amorphous as-sprayed material. The high porosity of as-sprayed as well as annealed tourmaline opens application potential as e.g. scaffolds for catalysts [76].

  Kaolinite mineral was plasma sprayed as coatings on stainless steel or carbon steel or ceramic tiles and/or as free-standing kaolinite planar parts. Thermal post-treatment of the powder already before spraying was shown to enhance the sprayability of powder transformed to metakaolinite. The coatings were able to

survive thermal exposition to silicate dust due to crystallization of amorphous as-sprayed material and/or recrystallization of other phases to mullite, which is more chemically simple substance, and also more thermally stable [77].

Calcined clay shale was plasma sprayed to form free-standing plates. Again, as for the previous material, certain degree of mullite formation was attained. Thermal post-treatment was shown to improve the properties of the coatings due to crystallization of predominantly amorphous as-sprayed material [78].

8 Literature

[1] Bose S., 2018. In: High temperature coatings. Butterworth-Heinemann, Oxford, UK, p. 29-43.

[2] Fookes P.G. Geomaterials. Quarterly Journal of Engineering Geology and Hydrogeology, 24 (1991) 3-15.

[3] Přikryl R., Török Á., Gómez-Heras M., Miskovsky K., Theodoridou M, 2016. In: Sustainable use of traditional geomaterials in construction practice, Geological Society, London, UK, p. 5-7.

[4] Hrabovský M. Water-stabilized plasma generators. Pure and Applied Chemistry, 6 (1998) 1157-1162.

[5] http://www.ofic.co.jp/en/r_and_d/thermalspraying/, 5.4.2020.

[6]http://www.ipp.cas.cz/vedecka_struktura_ufp/materialove-inzenyrstvi/galerie/08-mikrostruktury.html, 5.4.2020.

[7] Cao X.Q., Vassen R., Stoever D. Ceramic materials for thermal barrier coatings. Journal of the European Ceramic Society, 24 (2004) 1–10.

[8] Pokorný V., 1988. Práškové materiály pro hořáky řady PAL z netradičních surovin. Ústavní zpráva č. 9/88. Ústav fyziky plazmatu, Praha 8.

[9] Chráska P., Dubský J., Neufuss K., Písačka J. Alumina-base plasma-sprayed materials, Part I: Phase stability of alumina and alumina-chromia. Journal of Thermal Spray Technology, 6 (1997) 320-326.

[10] https://www.eutit.cz/eucor.html, 5.4.2020.

[11] Chráska T., Neufuss K., Dubský J., Nohava J. Plasma spraying of a novel material with amorphous and nanocrystalline microstructure. International thermal spray conference. Ljubljana, 2005.

[12] Chráska T., Neufuss K., Dubský J., Ctibor P., Rohan P. Fabrication of bulk nanocrystalline alumina–zirconia materials. Ceramics International, 34 (2008) 1229-1236.

[13] Brožek V., Dubský J., Kolman B., Neufuss K., Chráska P. Plasma sprayed coatings of molybdenum silicide. 8th International conference of high temperature materials chemistry. Vienna, 1994.

[14] Ctibor P., Neufuss K., Štengl V., 2009. Structure and properties of plasma sprayed TiO_2 ceramics. NOVA Science Publishers, New York, p. 115-161. ISBN 978-1-60692-516-4.

[15] Matějíček J., Neufuss K., Ctibor P., Rohan P., Dubský J., Chráska P., Brožek V. WSP-sprayed boron carbide coatings for fusion applications. International Thermal Spray Conference. Düsseldorf, 2002.

[16] Bayrak G., Senol Y. Crystallization kinetics of plasma sprayed basalt coatings. Ceramics International, 32 (2006) 441–446.

[17] Chráska P., Neufuss K., Kolman B., Dubský J. Plasma Spraying of Silicates. A United Forum for Scientific and Technological Advances. Materials Park, OH: ASM International, 1998.

[18] Berghaus-Oberste J., Chráska T., Neufuss K., Moreau Ch., Chráska P. Thermal spraying of basalt for abrasion protective coatings using WSP, HVOF and APS. International Thermal Spray Conference. Dusseldorf, 2005.

[19] Bayrak G., Ercenk E., Ugur S., Yilmaz S. Bond strength of basalt based glass-ceramic coatings. Acta Physica Polonica A, 125 (2014) 620-622.

[20] Ercenk E., Sena U., Yilmaz S. The effect of SiC addition on the crystallization kinetics of atmospheric plasma–sprayed basalt-based coatings. Ceramics International, 38 (2012) 49–56.

[21] Ageorges H., Medarhri Z., Ctibor P., Fauchais P. Plasma sprayed basalt/chromium oxide coatings. High Temperature Materials and Processes, 1 (2007) 71-82.

[22] http://geologie.vsb.cz/loziska/loziska/index.html, 5.4.2020.

[23] Kolman B., Forman J., Dubský J., Chráska P. Homogenity studies of powders and plasma sprayed deposits. Microchimica Acta, 114/115 (1994) 335-342.

[24] http://www.cluz.cz/cz/palene-materialy, 5.4.2020.

[25] Chráska P., Kolman B., Dubský J., Ctibor P., Neufuss K. Spatial distribution of chemistry, structural features and phases in tehrmal spray deposits. Acta Technica CSAV, 46 (2001) 323-336.

[26] Neufuss K., Ilavský J., Dubský J., Kolman B., Chráska P. Plasma Spraying of Silicates II. United Thermal Spray Conference. Düsseldorf, 1999.

[27] Ctibor P., Sedláček J., Neufuss K., Dubský J., Chráska P. Dielectric properties of plasma-sprayed silicates. Ceramics International, 31 (2005) 315–321.

[28] Ctibor P., Kotlan J., Pala Z., Neufuss K., Soumar J. Plasma spraying of natural olivine and its dielectric, mechanical and optical characterization. Romanian Reports in Physics, 2 (2015) 600–616.

[29] Liu X., Ding C. Characterization of plasma sprayed wollastonite powder and coatings. Surface and Coatings Technology, 153 (2002) 173-177.

[30] Kim Y.-H., Shin P.-W., Lee S.-J. Preparation of granule powders for thermal spray coating by utilization of pyrophyllite minerals. Journal of the Korean Ceramic Society, 53 (2016) 557-562.

[31] Bhuyan S.K., Thiyagarajan T.K., Mishra S.C.. Development of ceramic coating on metal substrate using industrial waste and ore minerals. Materials Science and Engineering, 178 (2017) 012029.

[32] Bhuyan S.K., Samal S., Pattnaik D., Sahu A., Swain B., Thiyagarajan T.K., Mishra S.C. Effect of bauxite addition on adhesion strength and surface roughness of fly ash based plasma sprayed coatings. Materials Science and Engineering, 338 (2018) 012053.

[33] Mishra S.C., Praharaj S. Deposition of plasma spray coating using industrial waste with low grade ore mineral. Orissa Journal of Physics, 18 (2011) 199-206.

[34] Mishra S.C., Sahu A., Das R., Satapathy A., Sen S., Ananthapadmanabhan P. V., Sreekumar K.P. Microstructure, adhesion and erosion wear of plasma sprayed alumina-titania composite coatings. Journal of reinforced plastics and composites, 28 (2008) 9-13.

[35] Chvátal M., 2005. Úvod do systematické mineralogie. Silikátový svaz, Praha. str. 39,78, 90, 97, 111. ISBN 80-86821-11-5.

[36] Chráska P., Neufus K., Herman H. Plasma Spraying of zircon. Journal of Thermal Spray Technology, 6 (1997) 445-448.

[37] Stevens R., 1986. In: An Introduction to Zirconia Ceramics. No. 113, Magnesium Elektron, Ltd., UK. 8-9.

[38] Dubský J., Kolman B., Neufuss K. Phase composition changes in annealed plasma sprayed zircon-alumina coatings. A united forum for scientific and technological advances. Materials park, OH: ASM International, 1998.

[39] Dubský J., Kolman B., Buchal A.Phase composition changes in plasma sprayed zircon alumina tubes. Meeting the challenges of the 21st century.Materials Park, OH: ASM International, 1998.

[40] Ramswamy P., Seetharamu S., Varma K.B.R., Rao K.J. Thermal barrier coating application of zircon sand. Journal of Thermal Spray Technology, 8 (1999) 447-453.

[41] Rohan P., Neufuss K., Matějíček J., Dubský J., Prchlík L., C. Holzgartner. Thermal and mechanical properties of cordierite, mullite and steatite produced by plasma spraying. Ceramics International, 30 (2004) 597-603.

[42] An Y., Chen J.M., Zhou H.D., Liu G. Microstructure and thermal cycle resistance of plasma sprayed mullite coatings made from secondary mullitized natural andalusite powder. Surface and Coatings Technology, 205 (2010) 1897-1903.

[43] An Y., Liu G., Zhao X.Q., Chen J.M., Zhou H.D., Hou G.L. Preparation and microstructure characterization of mullite coatings made of mullitized natural andalusite powders. Journal of Thermal Spray Technology, 3 (2011) 479-485.

[44] An Y., Zhao X.G., Hou G.L., Zhou H.D., Chen J., Chen J.M. Tribological and thermal properties of mullite coating prepared by atmospheric plasma spraying. Journal of Thermal Spray Technology, 23 (2013) 410–419.

[45] Chen C.Y., Lan G.S., Tuan W.H. Microstructural evolution of mullite during the sintering of kaolin powder compacts. Ceramics International, 26 (2000) 715-720.

[46] Kim B.M., Cho Y.K., Yoon S.Y., Stevens R., Park H.C. Mullite whiskers derived from kaolin. Ceramics International, 35 (2009) 579-583.

[47] Bai J. Fabrication and properties of porous mullite ceramics from calcined carbonaceous kaolin and α-Al2O3. Ceramics International, 36 (2010) 673-678.

[48] Yung-Feng C., Wang M.C., Hon M.H. Phase transformation and growth of mullite in kaolin ceramics. Journal of the European Ceramic Society, 24 (2004) 2389-2397.

[49] Castelein O., Soulestin B., Bonnet J.P., Blanchart P. The influence of heating rate on the thermal behaviour and mullite formation from a kaolin raw material. Ceramics International, 27 (2001) 517-522.

[50] Fiala J. Nonhydrolytic synthesis of alumosilicates. Brno, 2009. Masters thesis. Masaryk University, Faculty of Natural Sciences. (in Czech).

[51] Benazzouz B.K., Zaoui A., Belonoshko A.B. Determination of the melting temperature of kaolinite by means of the Z-method. American Mineralogist, 98 (2012) 1881-1885.

[52] Kim D.-Y., Lee J.-G., Joshi B., Lee J.-H., Al-Deyab S.S., Yoon H.G.,Yang D.R., Yarin A., Yoon S.S. Supersonically sprayed thermal barrier layers using clay micro-particles. Applied Clay Science, 120 (2016) 142-146.

[53] Obada D.O., Dodoo-Arhin D., Dauda M., Anafi F.O., Ahmed A.S., Ajayi O.A. The impact of kaolin dehydroxylation on the porosity and mechanical integrity of kaolin based ceramics using different pore formers. Results in Physics, 7 (2017) 2718-2727.

[54] Cano N.F., Yauri J.M., Watanabe S. Thermoluminescence of natural and synthetic diopside. Journal of Luminescence, 128 (2008) 1185–1190.

[55] Ito M., Morioka M. Growth of diopside ($CaMgSi_2O_6$) single crystal by the Czochralski technique. Geochemical Journal, 40 (2006) 625–629.

[56] Romero M., Rincon A., Acosta A. Effect of iron oxide content on the crystallization of a diopside glass–ceramic glaze. Journal of the European Ceramic Society, 22 (2002) 883-890.

[57] Bozadjiev L.S., Bozadjiev R.L., Georgiev G.T., Doncheva L.S. Diopside porcelain tile. American Ceramic Society Bulletin, 85 (2006) 9101–9104.

[58] Kostikov K.S., Pogrebenkov V.M., Vereshchagin V.I. Diopside - the prospective compound of ceramics. The fifth russian-korean international symposium on science and technology. Tomsk Polytechnic University, 2001.

[59] Razavi M., Fathi M., Savabi O., Vashaee D., Tayebi L. In vitro study of nanostructured diopside coating on Mg alloy orthopedic implants. Materials Science and Engineering: C, 41 (2014) 168–177.

[60] Xue W., Liu X., Zheng X., Ding C. Plasma-sprayed diopside coatings for biomedical applications. Surface and Coatings Technology, 185 (2004) 340–345.

[61] Maldiney T., Lecointre A., Viana B., Besièrre A., Gourier D., Bessodes M., Richard C., Scherman D. Trap depth optimization to improve optical properties of diopside-based nanophosphors for medical imaging. Oxide-based materials and devices III.San Francis.

[62] Henderson E. Chemical and physical properties of tourmaline. Plymouth, Devon, 1971. Doctoral thesis. Plymouth Polytechnic.

[63] Hawkins K.D., MacKinnon D.R., Schneeberger H. Influence of chemistry on the pyroelectric effect in tourmaline. American Mineralogist, 80 (1995) 491–501.

[64] Xu H.-Y., Prasad M., Liu Y.Schorl: A novel catalyst in mineral-catalyzed Fenton like system for dyeing wastewater discoloration. Journal of Hazardous Materials, 165 (2009) 1186–1192.

[65] Xu H.-Y., Prasad M., He X.-L., Shan L.-W., Qi S.-Y. Discoloration of Rhodamine B dyeing wastewater by schorl-catalyzed Fenton-like reaction. Science in China, Series E Technological Sciences, 52 (2009) 3054-3060.

[66] Liu S.M., Li D.C., Hu W.T., Qin G.Q., Li L.F. Ion-beam deposition of tourmaline film on glass. Journal of Non-Crystalline Solids, 354 (2008) 1444–1446.

[67] Salimijazi H., Hosseini M., Mostaghimi J., Pershin L., Coyle T.W., Samadi H., Shafyei A. Plasma sprayed coating using mullite and mixed alumina/silica powders. Journal of Thermal Spray Technology, 21 (2012) 825-830.

[68] Wang W., Liang J., Guo X., Xuan F., Hong H. Mechanical properties and dissolution behavior of plasma sprayed wollastonite coatings deposited at different substrate temperatures. Journal of Thermal Spray Technology, 21 (2012) 496–504.

[69] Cojocaru C.V., Lamarre J.-M., Legoux J.-G., Marple B.R. Atmospheric plasma sprayed forsterite (Mg_2SiO_4) coatings: An investigation of the processing-microstructure-performance relationship. Journal of Thermal Spray Technology, 22 (2013) 145–151.

[70] Fauchais P., Fukumoto M., Vardelle A., Vardelle M. Knowledge concerning splat formation: An invited review. Journal of Thermal Spray Technology, 13 (2004) 337–360.

[71] Schelz S., Branland N., Plessis D., Minot B., Guillet F. Laser treatment of plasma sprayed $ZrSiO_4$ coatings. Surface and Coatings Technology, 200 (2006) 6384 6388.

[72] Suzuki M., Sodeoka S., Inoue T., Ueno K., Oki S., Shimosaka K. Structure and properties of plasma-sprayed zircon coating. 1st International thermal spray conference: Thermal spray - surface engineering via applied research. Materials Park, OH: ASM International, 2000.

[73] Kaiser A., Lobert M., Telle R. Thermal stability of zircon ($ZrSiO_4$), Journal of the European Ceramic Society, 28 (2008) 2199–2211.

[74] Ctibor P., Pala Z., Nevrlá B., Neufuss K. Plasma-sprayed fine-grained zirconium silicate and its dielectric properties. Journal of Materials Engineering and Performance, 26 (2017) 2388-2393.

[75] Ctibor P., Nevrlá B., Pala Z., Sedláček J., Soumar J., Kubatík T., Neufuss K., Vilémová M., Medřický J. Study on the plasma sprayed amorphous diopside and annealed fine-grained crystalline diopside. Ceramics International, 41 (2015) 10578-10586.

[76] Ctibor P., Nevrlá B., Pala Z., Vrtiška L. Natural tourmaline as an efficient alternative to ceramic-type material for plasma spraying. Journal of the Southern African Institute of Mining and Metallurgy, 118 (2018) 387-393.

[77] Nevrlá B., Ctibor P., Koudelková V., Lukáč F., Neufuss K. Plasma spraying of natural kaolinite and metakaolinite. Boletin de la Sociedad Espanola de Ceramica Y Vidrio. *In press*. doi:10.1016/j.bsecv.2020.03.005.

[78] Dubský J., Chráska T., Pala Z., Nevrlá B., Chráska P. Plasma spraying of silica-rich calcined clay shale. Journal of Thermal Spray Technology, 4 (2014) 732-741.

[79] Ústav fyziky plazmatu AV ČR. Method of controlling size and number of pores of self supporting ceramic bodies. Neufuss K., Chráska P. April 2000. Czech Republic Patents No. 286735. Úřad průmslového vlastnictví.

[80] Ústav fyziky plazmatu AV ČR. Způsob výroby samonosných těles na bázi keramiky vytvářených metodou plazmového nanášení na duté nebo plné jádro. Neufuss K., Chráska P. November 1997. Czech Republic Patents No. 283203. Úřad průmslového vlastnictví.

[81] MPDB - Materials Properties Database, v. 8.82, rel. 2020. JAHM Software, http://www.jahm.com.

[82] US Standard ASTM G 75-95. Standard test method for determination of slurry abrasivity (miller number) and slurry abrasion response of materials (SAR number). West Conshohocken, PA, United States: ASTM International, March 1995.

[83] Ctibor P., Neufuss K., Pala Z., Kotlan J., Soumar J. Dielectric and mechanical properties of plasma-sprayed olivine. Romanian Reports in Physics, 67 (2015) 600–616.

[84] Ctibor P., Hrabovsky M. Plasma sprayed TiO_2: The influence of power of an electric supply on particle parameters in the flight and character of sprayed coating. Journal of the European Ceramic Society, 30 (2010) 3131– 3136.

[85] Matějíček J., Chumak O.,Konrád M.,Oberste-Berghaus J., Lamontagne M. The influence of spraying parameters on in-flight characteristics of tungsten particles and the resulting splats sprayed by hybrid water-gas stabilized plasma torch. International Thermal Spray Conference. Basel (CH), 2005.

[86] Čížek J., Khor K.A. Role of in-flight temperature and velocity of powder particles on plasma sprayed hydroxyapatite coating characteristics. Surface and Coatings Technology, 206 (2012) 2181–2191.

[87] Smith D.K., Newkirk W. The crystal structure of baddeleyite (monoclinic ZrO_2) and its relation to the polymorphism of ZrO_2. Acta Crystallographica, 18(1965) 983–991.

[88] Teufer G. The crystal structure of tetragonal ZrO_2. Acta Crystallographica, 15 (1962) 187–1195.

[89. Shannon R.D. Revised effective ionic radii and systematic studies of interatomic distances in halides and chalcogenides. Acta Crystallographica, 32 (1972) 751–767.

[90] Itoh T. Formation of polycrystalline zircon ($ZrSiO_4$) from amorphous silica and amorphous zirconia. Journal of Crystal Growth, 125 (1992) 223—228.

[91] Chraska T., King A.H., Berndt C.C. On the size-dependent phase transformation in nanoparticulate zirconia. Materials Science and Engineering A, 286 (2000) 169–178.

[92] Hsu Y.-W., Yang K.-H., Yeh S.-W., Wang M.-C. Mechanism of lower activation energy for tetragonal ZrO_2 crystallite growth in the 3 mol% yttria partially stabilized zirconia (3Y-PSZ) precursor powders. Journal of Alloys and Compounds, 555 (2013) 82–87.

[93] Puclin T., Kaczmarek W.A., Ninham B.W. Mechanochemical processing of $ZrSiO_4$. Materials chemistry and physics, 40 (1995) 73–81.

[94] Longo F.N., 2004. Coating operations.In: Davis J.R. (ed.). Handbook of Thermal Spray Technology. ASM International, Materials Park, OH, p.123. ISBN 0-87170-795-0.

[95] Ctibor P., Nevrlá B., Pala Z., Sedláček J., Kubatík T., Neufuss K., Vilémová M., Medřický J. Study on the plasma sprayed diopside. Konference Vrstvy a povlaky. Rožnov pod Radhoštěm, 2014.

[96] Kotlan J., Ctibor P., Pala Z., Homola P., Nehasil V. Improving dielectric properties of plasma sprayed calcium titanate ($CaTiO_3$) coatings by thermal annealing. Ceramics International, 40 (2014) 13049–13055.

[97] Stergiou A.C., D.K. Gioureli. Crystallographic study of the mineral ferroan clinozoisite from three localities of Northern Greece. Powder Diffraction, 13 (1998) 222–226.

[98] Choi B.K., Sun G.N., Kim E.S. Microwave dielectric properties of diopside glass ceramics. Ceramics International, 39 (2013) 677–680.

[99] Eoh Y.J., Kim E.S. Effect of heat-treatment on the dielectric properties of $CaMgSi_2O_6$ glass–ceramics with Cr_2O_3–Fe_2O_3–TiO_2. Japanese Journal of Applied Physics, 53 (2014) 08NB01.

[100] Ctibor P., Kubát J., Nevrlá B., Pala Z. Plasma spraying of cerium-doped YAG. Journal of Materials Research, 29 (2014) 2344-2351.

[101] Shackelford J.F., Doremus R.H. (eds.), 2008. Ceramic and glass materials: structure, properties and processing. Springer, New York,p. 37. ISBN 978-0-387-73361-6.

[102] Andrini L., Gauna M.R., Conconi M.S., Suarez G., Requejo F.G., Aglietti E.F., Rendtorff N.M. Extended and local structural description of a kaolinitic clay, its fired ceramics and intermediates: An XRD and XANES analysis. Applied Clay Science, 124–125 (2016) 39-45.

[103] Lvov B.V., 2007. Thermal decomposition of solids and melts. Springer, New York, p. 189. ISBN: 978-1-4020-5671-0.

[104] Boch P., Niepce J.-C. (eds.), 2007. Ceramic materials, processes, properties and applications. ISTE Ltd, London, p. 81. ISBN13:978-1-905209-23-1.

[105] Harabi A., Zaiou S., Guechi A., Foughali L., Harabi E., Karboua N.-E., Zouai S., Mezahi F.-Z., Guerfa F. Mechanical properties of anorthite based ceramics prepared from kaolin DD2 and calcite. Ceramica, 63 (2017) 311-317.

[106] Ctibor P., Sedláček J., Neufuss K. Dielectric properties of plasma sprayed silicates with and without additional annealing. Acta Technica CSAV, 52 (2007) 385-397.

[107] Li S., Zhao X., An Y., Deng W., Hou G., Hao E., Zhou H., Chen J. Effect of deposition temperature on the mechanical, corrosive and tribological properties of mullite coatings. Ceramics International, 44 (2018) 6719-6729.

[108] Ramaswamy P., Seetharamu S., Varma K.B.R., Rao K.J. Thermal shock characteristics of plasma sprayed mullite coatings. Journal of Thermal Spray Technology, 7 (1998) 497-504.

[109] Stubna I., Sin P., Vilju M., Trnik A. The effect of the firing temperature on the hardness of alumina porcelain. Materiali in Tehnologije, 48 (2014) 331-336.

[110] Cano C., Garcia E., Fernandes A.L., Osendi M.I., Miranzo P. Mullite/ZrO_2 coatings produced by flame spraying. Journal of the European Ceramic Society, 28 (2008) 2191-2197.

[111] Hou G., An Y., Zhao X., Zhou H., Chen J. Effect of critical plasma spraying parameter on microstructure and wear behavior of mullite coatings. Tribology International, 94 (2016) 138-145.

[112] De Aza A.H., Turrillas X., Rodriguez M.A., Duran T., Pena P. Time-resolved powder neutron diffraction study of the phase transformation sequence of kaolinite to mullite. Journal of the European Ceramic Society, 34 (2014) 1409-1421.

[113] Di Girolamo G., Blasi C., Pilloni L., Schioppa M. Microstructural and thermal properties of plasma sprayed mullite coatings. Ceramics International, 36 (2010) 1389-1395.

[114] Fisher J.G., Chang K., James P.F., Messer P.F., Davies H.A. Ceramic flake formation in the aluminosilicate system by plasma spraying, Journal of Materials Science, 40 (2005) 1625-1632.

[115] Escalera E., Antti M.L., Odén M. Thermal treatment and phase formation in kaolinite and illite based clays from tropical regions of Bolivia. 6th EEIGM International Conference on Advanced Materials Research. Nancy, France, 2011.

[116] Stubna I., Trnik A., Chmelik F., Vozar L.,2011. In: Sikalidis C. (ed.). Advances inceramics – characterization, raw materials, processing, properties, degradation and healing. IntechOpen Limited, London, p. 233. ISBN: 978-953-307-504-4.

[117] Holdridge D.A. Thermal expansion as a method for checking the composition of ceramic clays and of studying mineralogical changes during firing. Clay Minerals Bulletin, 4 (1959) 94-105.

[118] Boissonnet G., Bonnet G., Pasquet A., Bourhila N., Pedraza F. Evolution of thermal insulation of plasma-sprayed thermal barrier coating systems with exposure to high temperature. Journal of the European Ceramic Society, 39 (2019) 2111-2121.

[119] Li J.F., Li L., Ding C.X. Thermal diffusivity of plasma-sprayed Cr_3C_2–NiCr coatings. Materials Science and Engineering: A. 394 (2005) 229-237.

[120] Mikuskiewicz M., Moskal G., Migas D., Stopyra M. Thermal diffusivity characterization of europium zirconate, cerate and hafnate. Ceramics International, 45 (2019) 2760-2770.

[121] Heller-Kallai L., Lapides I. Reactions of kaolinites and metakaolinites with NaOH. Comparison of different samples (Part 1). Applied Clay Science, 35 (2007) 99-107.

[122] Kuenzel C., Vandeperre L.J., Donatello S., Boccaccini A.R., Cheeseman. Ambient temperature drying shrinkage and cracking in metakaolin-based geopolymers. Journal of the American Ceramic Society, 95 (2012) 3270-3277.

[123] Ptáček, Frajkorová F., Šoukal F., Opravil T. Kinetics and mechanism of three stages of thermal transformation of kaolinite to metakaolinite. Powder Technology, 264 (2014) 439-445.

[124] Jech D. Processing and structural stability of nanocrystalline thermal barrier coatings. Brno, 2018. Doctoral Thesis. Brno University of Technology. (in Czech).

[125] Chráska T., Hostomský J., Klementová M., Dubský J. Crystallization kinetics of amorphous alumina-zirconia-silica ceramics. Journal of the European Ceramic Society, 29 (2009) 3159-3165.

[126] McConnell J.D.C., Fleet S.G. Electron optical study of the thermal decomposition of kaolinite. Clay Minerals, 8 (1970) 279-290.

[127] Sonuparlak B., Sarikaya M., Aksay I.A. Spinel phase formation during the 980 °C exothermic reaction in the kaolinite-to-mullite reaction series. Journal of the American Ceramic Society, 70 (1987) /837-842.

[128] Bellotto M., Gualtieri A., Artioli G., Clark S.M. Kinetic study of the kaolinite-mullite reaction sequence. Part I: Kaolinite dehydroxylation. Physics and Chemistry of Minerals, 22 (1995) 207-214.

[129] Gualtieri A., Bellotto M., Artioli G., Clark S.M. Kinetic study of the kaolinite-mullite reaction Sequence. Part II: Mullite formation. Physics and Chemistry of Minerals, 22 (1995) 215-222.

[130] Ray C.S., Day D.E. Nucleation and crystallization in glasses as determined by DTA. Ceramic Transactions, Nucleation and Crystallization in Glasses, 30 (1993) 207-233.

[131] Johnson B.R., Kriven W.M., Schneider J. Crystal structure development during devitrification of quenched mullite. Journal of the European Ceramic Society, 21 (2001) 2541-2562.

[132] Kissinger H.E. Variation of peak temperature with heating rate in differential thermal analysis. Journal of Research of the National Bureau of Standards, 57 (1956) 217-221.

[133] Aksay A., Dabbs D.M., Sarikaya M. Mullite for structural, electronic, and optical applications. Journal of the American Ceramic Society, 74 (1991) 2343-2358.

[134] Aksay A., Pask J.A. The silica-alumina system: Stable and metastable equilibria at 1.0 atmosphere. Science, 183 (1974) 69-71.

[135] Chráska T., Neufuss K., Dubský J., Ctibor P., Klementová M. Fabrication of bulk nanocrystalline ceramic materials. Journal of Thermal Spray Technology, 17 (2008) 872-877.

[136] Chráska T., Neufuss K., Oberste-Berghaus J., Lamontagne M., Moreau Ch. In-flight particle diagnostic of water stabilized plasma spray process. International Thermal Spray Conference. Düsseldorf, 2005.

[137] Nour W.M.N., Awad H.M. Effect of MgO on phase formation and mullite morphology of different egyptian clays. Journal of the Australian Ceramic Society, 44 (2008) 27-37.

[138] Ctibor P., Nevrlá B., Neufuss K., Petrášek J., Sedláček J. Plasma spray coatings of natural ores from structural, mechanical, thermal, and dielectric viewpoints. Coatings, 10 (2019) 1-16.

[139] Harekrushna S., Mishra B., Murmu R., Sangram P., Sarat P., Mishra S.C. Wettability, thermal and sliding behavior of thermally sprayed fly ash premixed red mud coatings on mild steel. Materials Sciences and Applications, 11 (2019) 12-26.

[140] Mantry S., Jha B.B, Satapathy A. Evaluation and characterization of plasma sprayed Cu slag - Al composite coatings on metal substrates. Journal of Coatings, (2013) 1-7.

A List of Publications Related to the Thesis

A1 Papers in Impacted Journals

Nevrlá B., Ctibor P., Koudelková V., Lukáč F., Neufuss K. Plasma spraying of natural kaolinite and metakaolinite. Boletin de la Sociedad Espanola de Ceramica Y Vidrio. *In press.* doi:10.1016/j.bsecv.2020.03.005 (Ref. [77])

Ctibor P., Nevrlá B., Neufuss K., Petrášek J., Sedláček J. Plasma spray coatings of natural ores from structural, mechanical, thermal, and dielectric viewpoints. Coatings, 10 (2019) 1-16. [138]

Ctibor P., Nevrlá B., Pala Z., Vrtiška L. Natural tourmaline as an efficient alternative to ceramic-type material for plasma spraying. Journal of the Southern African Institute of Mining and Metallurgy, 118 (2018) 387-393. (Ref. [76])

Ctibor P., Pala Z., Nevrlá B., Neufuss K. Plasma-sprayed fine-grained zirconium silicate and its dielectric properties. Journal of Materials Engineering and Performance, 26 (2017) 2388-2393. (Ref. [74])

Ctibor P., Nevrlá B., Pala Z., Sedláček J., Soumar J., Kubatík T., Neufuss K., Vilémová M., Medřický J. Study on the plasma sprayed amorphous diopside and annealed fine-grained crystalline diopside. Ceramics International, 41 (2015) 10578-10586. (Ref. [75])

Dubský J., Chráska T., Pala Z., Nevrlá B., Chráska P. Plasma spraying of silica-rich calcined clay shale. Journal of Thermal Spray Technology, 4 (2014) 732-741. (Ref. [78])

A2 Other Publications

Ctibor P., Nevrlá B., Pala Z., Sedláček J., Kubatík T., Neufuss K., Vilémová M., Medřický J. Study on the plasma sprayed diopside. Konference Vrstvy a povlaky. Rožnov pod Radhoštěm, 2014. (Ref. [95])

List of Figures

Figure 1. Scheme of water stabilized (a) and hybrid plasma torch (b) [4]

Figure 2. Scheme of the plasma coating [5] and the detail of splat (an Eucor ceramic coated with the water torch, electron microscope) [6]

Figure 3. Cross section of two $ZrSiO_4$ coatings produced by WSP spraying: 28-290 (a) and 23-200 (b) (light microscopy)

Figure 4. XRD pattern of $ZrSiO_4$ coating

Figure 5. Detailed DTA curve of $ZrSiO_4$ coating

Figure 6. Optical micrographs of diopside splats on glass: FD 50 mm (top left) FD 70 mm (top right) and FD 60 mm (bottom)

Figure 7. Optical micrographs of diopside feedstock powder and free-flight particles at feeding distance 50 mm, 60 mm and 70 mm

Figure 8. Optical micrographs of diopside free-standing plates at FD 65 mm non-sieved (left) and the separated size above 250 μm (right)

Figure 9. Surface of the diopside self-supporting plate (SEM-SE)

Figure 10. Cross section of diopside self-supporting plate (SEM-BSE)

Figure 11. Diopside coating EDX spectrum

Figure 12. XRD patterns of diopside feedstock powder (1), as-sprayed sample (2) and samples after 15 min (3) and 30 h (4) annealing at 900 °C (vertical shift was introduced in order to distinguish between the patterns)

Figure 13. Rietveld refinement of powder XRD pattern measured on a diopside sample annealed for 30 h at 900 °C; the measured data are in blue and the fit is in red, difference between both is ("R_{wp} quality of the fit") presented as a gray curve at zero intensity

Figure 14. Line EDX scan showing variations in chemical composition among single splats of diopside coating

Figure 15. DTA curve of the diopside feedstock powder and as-sprayed FSP

Figure 16. Tourmaline splats on glass with constant feeding distance 40 mm (optical micrograph)

Figure 17. Free-flight particles collected at feeding distance 40 mm (left) and 80 mm (right) (optical micrograph)

Figure 18. Tourmaline free-flight particles collected at feeding distance 40 mm (optical micrograph)

Figure 19. Tourmaline coatings sprayed using FD 40 with SD 350 mm (left) and FD 90 with SD 250 mm (right) (optical micrograph)

Figure 20. Crystallinity of tourmaline coatings with varying FD and SD

Figure 21. Surface roughness of plasma sprayed tourmaline (corresponding SD [mm] indicated at each point)

Figure 22. DTA curve of tourmaline feedstock powder

Figure 23. Reflectance of tourmaline coatings with varying FD and SD

Figure 24. Colour changes of tourmaline coatings – annealed are left: FD100/SD250 (top), FD40/SD350 (bottom)

Figure 25. Tourmaline coating after 1000 °C/30 min annealing (left) and a FSP after 1000 °C/8 h annealing (right) (optical micrograph on cross section)

Figure 26. Size distribution of the kaolinite (KP) and metakaolinite (MK) powders

Figure 27. SE micrographs of the kaolinite spray powder

Figure 28. BSE micrographs of the metakaolinite spray powder

Figure 29. Cross section micrographs of KP sprayed coating (a) and MK sprayed coating (b)

Figure 30. Surface micrographs of KP sprayed coating (a) and MK sprayed coating (b)

Figure 31. DTA curve of kaolin materials

Figure 32. Thermogravimetric curves of kaolin materials

Figure 33. Thermal expansion curves of kaolin materials

Figure 34. Diffraction patterns of two different fractions of A111: narrow fraction of 40 to 80 μm (red pattern) and fraction below 40 μm (black pattern)

Figure 35. In-flight particle data in dependency on processing parameters FD and SD; velocity (a) and temperature (b)

Figure 36. Structure on cross sections of A111 coatings on steel substrate (SEM)

Figure 37. XRD patterns from the feedstock (red) and from as-sprayed coating (blue)

Figure 38. Thermal expansion curves of as-sprayed calcined clay shale

Figure 39. Thermal conductivity data of as-sprayed calcined clay shale

Figure 40. Results of DSC measurements of as-sprayed calcined clay shale

Figure 41. Selected XRD patterns for successive samples (a) and HTXRD (b)

Figure 42. Result of Rietveld refinement of sample annealed at 1400 °C for 30 min

Figure 43. Structure of A111 deposit after annealing at 1500 °C (SEM)

Figure 44. Summary of dependency of crystallinity and crystallite size on annealing temperature calculated from XRD patterns

List of Tables

Table 1. Transformations in kaolinite structure during firing, based on literature [50]

Table 2. Plasma spray parameters for zircon

Table 3. Parameters of DTA and TG measurements

Table 4. Image analysis of pores in $ZrSiO_4$ coatings and comparison with different silicate coatings [83; 84]

Table 5. Mechanical characteristics of the as-sprayed diopside [95]

Table 6. Porosity and specific weight of the as-sprayed diopside ([a] Image analysis, [b] Pycnometry, [c] Immersion) [75; 95]

Table 7. Immersion determined open porosity of diopside coatings

Table 8. Chemical elements content in the as-sprayed diopside (determined by EDX)

Table 9. Characteristic of selected tourmaline coatings with comparsion to other plasma sprayed silicates [83]

Table 10. Microhardness characteristics of tourmaline plasma sprayed coatings

Table 11. XRF elemental analysis on kaolin coating surfaces [105]

Table 12. Porosimetry ([a] He pycnometry, [b] Immersion) and microhardness of the as-sprayed kaolin

Table 13. Image analysis results of plasma sprayed KP and MK coatings

Table 14. Thermal diffusivity [cm^2/s] of plasma sprayed KP and MK coatings

Table 15. XRD phases of kaolin material, semiquantitative content (% of total), [% of crystalline only] ([a] CMAS composition is based on literature [124])

Table 16. Data for A111 powder

Table 17. Summary of phase composition of selected samples (820 °C, 1200 °C, 1400 °C and 500 °C for deposits annealed for 30 min)

Table 18. Sizes of the coherent crystallites in selected samples (1200 °C and 1400 °C for deposits annealed for 30 min)

Table 19. XRD data from Rietveld analysis of FFP and HTXRD samples

Table 20. Maximal temperature limiting the durability of as-sprayed coatings